University of California
Los Angeles

Physical Processes in the Vicinity of a Supermassive Black Hole

A dissertation submitted in partial satisfaction
of the requirements for the degree
Doctor of Philosophy in Astronomy

by

Tuan Do

2010

The dissertation of Tuan Do is approved.

Craig Manning

James Larkin

Mark Morris

Andrea Ghez, Committee Chair

University of California, Los Angeles

2010

to Mom and Dad

Table of Contents

List of Figures

List of Tables

Acknowledgments

This thesis could not have been written in isolation. Many people in all parts of my life have made essential contributions to its completion. I would like to thank my advisor, Andrea Ghez for helping me become a better scientist; Mark Morris for illuminating discussions; Shelley Wright and James Larkin for teaching me all I know about integral field spectroscopy; Brad Hansen and Matthew Wood for discussions of stellar kinematic models; Xi Chen, Sylvana Yelda, Damien Ramunno-Johnson, and Quinn Konopacky for your support throughout grad school. Most of all, I would like to thank my father, mother, and brother for their lifelong support of my education.

I acknowledge that results presented in this thesis are based on published works with additional coauthors. In particular, Chapter two is a version of Do et al. (2009b) and Chapter Three is derived from Do et al. (2009a). The W.M. Keck Observatory is operated as a scientific partnership among the California Institute of Technology, the University of California and the National Aeronautics and Space Administration. The Observatory was made possible by the generous financial support from the W. M. Keck Foundation.

Vita

1982	Born, Vietnam
2004	B.A. (Astrophysics, Physics) University of California, Berkeley
2006	M.S. (Astronomy) University of California, Los Angeles.

Publications

Stolte, A., Morris, M. R., Ghez, A. M., Do, T., Lu, J. R., Ballard, C., Mills, E., Matthews, K., "Disks in the Arches cluster – survival in a starburst environment", 2010, The Astrophysical Journal, 718, 801

Do, T., Ghez, A. M., Morris, M. R., Lu, J. R., Matthews, K., Yelda, S., Larkin, J., 2009, "High angular resolution integral-field spectroscopy of the Galaxy's nuclear cluster: a missing stellar cusp?", The Astrophysical Journal, 703, 1323

Meyer, L., Do, T., Ghez, A., Morris, M. R., Yelda, S., Schoedel, R., Eckart, A., "A power-law break in the near-infrared power spectrum of the Galactic center black hole", 2009, The Astrophysical Journal Letters, 694, 1

Do, T., Ghez, A. M., Morris, M. R., Yelda, S., Meyer, L., Lu, J. R., Hornstein, S. D., Matthews, K., "A Near-Infrared Variability Study of the Galactic Black Hole: A Red Noise Source with No Detected Periodicity", 2009, The Astrophysical Journal, 691, 1021

Ghez, A. M., Salim, S., Weinberg, N. N., Lu, J. R., Do, T., Dunn, J. K., Matthews, K., Morris, M. R., Yelda, S., Becklin, E. E., Kremenek, T., Milosavljevic, M., Naiman, J., "Measuring Distance and Properties of the Milky Way's

Central Supermassive Black Hole with Stellar Orbits", 2008, The Astrophysical Journal, 689, 1044

Meyer, L., Do, T., Ghez, A., Morris, M. R., Witzel, G., Eckart, A., Blanger, G., Schodel, R., "A 600 Minute Near-Infrared Light Curve of Sagittarius A*", 2008, ApJL, 688, 17

Do, T., Ghez, A. M., Morris, M. R., Yelda, S., Lu, J. R., Hornstein, S. D., Matthews, K., "Testing for periodicities in near-IR light curves of Sgr A*", 2008, Journal of Physics: Conference Series, Volume 131, Proceedings of "The Universe Under the Microscope - Astrophysics at High Angular Resolution"

Do, T., Morris, M. R., Sahai, R., Stapelfeldt, K., "A Spitzer Study of the Mass-Loss Histories of Three Bipolar Preplanetary Nebulae", 2007, Astronomical Journal, 134, 1417

Morris, M. R., Uchida, K., Do, T., "A magnetic torsional wave near the Galactic Centre traced by a double helix nebula", 2006, Nature, 7082, 308

Hinkle, K. H., Joyce, R. R., Do, T., "Dust enshrouded AGB stars in the LMC", 2004, Variable Stars in the Local Group, IAU Colloquium 193, Conference Proceedings

Abstract of the Dissertation

Physical Processes in the Vicinity of a Supermassive Black Hole

by

Tuan Do

Doctor of Philosophy in Astronomy

University of California, Los Angeles, 2010

Professor Andrea Ghez, Chair

The Galactic center offers us an opportunity to study the environment around a supermassive black hole at a level of detail not possible in other galactic nuclei. This potential has been greatly expanded by the implementation of laser guide star adaptive optics and integral field spectroscopy on large ground-based telescopes. This thesis takes advantage of these technologies to address the nature of the variable near-infrared emission from the black hole as well as test theories of the equilibrium configuration of a star cluster with a supermassive black hole at its center.

First, we present the results of near-infrared (2 and 3 μm) monitoring of Sgr A*-IR with 1 min time sampling. Sgr A*-IR was observed continuously for up to three hours on each of seven nights, between 2005 July and 2007 August. Sgr A*-IR is detectable at all times and is continuously variable, with a median observed 2 μm flux density of 0.192 mJy, corresponding to 16.3 magnitude at K'. These observations allow us to investigate Nyquist sampled periods ranging from about 2 minutes to an hour. Using Monte Carlo simulations, we find that the variability of Sgr A* in this data set is consistent with models based on correlated noise with

power spectra having frequency dependent power law slopes between 2.0 to 3.0, consistent with those reported for AGN light curves. Of particular interest are periods of ~ 20 min, corresponding to a quasi-periodic signal claimed based upon previous near-infrared observations and interpreted as the orbit of a 'hot spot' at or near the last stable orbit of a spinning black hole. We find no significant periodicity at any time scale probed in these new observations for periodic signals. This study is sensitive to periodic signals with amplitudes greater than 20% of the maximum amplitude of the underlying red noise component for light curves with duration greater than ~ 2 hours at a 98% confidence limit.

Second, we report on the structure of the nuclear star cluster in the innermost 0.16 pc of the Galaxy as measured by the number density profile of late-type giants. Using laser guide star adaptive optics in conjunction with the integral field spectrograph, OSIRIS, at the Keck II telescope, we are able to differentiate between the older, late-type (~ 1 Gyr) stars, which are presumed to be dynamically relaxed, and the unrelaxed young (~ 6 Myr) population. This distinction is crucial for testing models of stellar cusp formation in the vicinity of a black hole, as the models assume that the cusp stars are in dynamical equilibrium in the black hole potential. In the survey region, we classified 77 stars as early-type 79 stars as late-type. We find that contamination from young stars is significant, with more than twice as many young stars as old stars in our sensitivity range ($K' < 15.5$) within the central arcsecond. Based on the late-type stars alone, the surface stellar number density profile, $\Sigma(R) \propto R^{-\Gamma}$, is flat, with $\Gamma = -0.26 \pm 0.24$. Monte Carlo simulations of the possible de-projected volume density profile, n(r) $\propto r^{-\gamma}$, show that γ is less than 1.0 at the 99.7 % confidence level. These results are consistent with the nuclear star cluster having no cusp, with a core profile that is significantly flatter than predicted by most cusp formation theories, and even allows for the presence of a central hole in the stellar distribution. Of the possible

dynamical interactions that can lead to the depletion of the red giants observable in this survey – stellar collisions, mass segregation from stellar remnants, or a recent merger event – mass segregation is the only one that can be ruled out as the dominant depletion mechanism. The degeneracy in the true distribution of stars cannot be broken with number counts alone, but we show how the addition of kinematic measurements can remove the degeneracy. Resolving the physical origin of the lack of a stellar cusp will have important implications for black hole growth models and inferences on the presence of a black hole based upon stellar distributions.

CHAPTER 1

Introduction

Within the past decade, the case for the existence of a supermassive black hole at the dynamical center of the Milky Way, long associated with the radio point source Sgr A*, has been firmly established by the measurement of orbits of stars around the center of the Galaxy at near-infrared (NIR) wavelengths. Barring some exotic unknown particle, the most likely possibility for an object with the high mass density measured from the orbits is a supermassive black hole with a mass of $\sim 4 \times 10^6 M_\odot$ (Ghez et al., 2008). While this represents the strongest evidence for a black hole of this mass, an increasing body of evidence is also supporting the existence of supermassive black holes at the centers of most, if not all, galaxies (Ferrarese & Ford, 2005). At a distance of $\sim$8 kpc, the black hole at the Galactic center is the closest in its class; thus observing its detailed properties is important for understanding all galactic nuclei. With recent advances in instrumentation for high angular resolution observations at near-infrared wavelengths (1 - 3 μm), we are now well poised to address questions about the black hole's environment - both the accretion flow and its effect on stars within its sphere of gravitational influence.

This thesis will capitalize on the new observational capabilities at the Keck telescopes (laser guide star adaptive optics and integral-field spectroscopy) to address two currently unresolved scientific questions: (1) What is the nature of the near-infrared variability associated with the location of the supermassive

black hole? (2) What is the long term dynamical influence of a black hole on a star cluster? How do the distribution of observed stars in the immediate vicinity of a massive black hole compared to longstanding theoretical predictions?

1.1 Laser guide star adaptive optics

While the Galactic center offers us the opportunity to study the physical processes associated with a supermassive black hole at a level of detail unmatched by any other source, observing this region in detail can be challenging: (1) because we are located at the edge of the Milky Way disk, there is tremendous amount of extinction of optical light from dust between us and the Galactic center; (2) large ground based telescopes have their angular resolution severely limited by atmospheric turbulence instead of the diffraction limit set by the telescope diameter.

The first challenge can be overcome by observing at near-infrared wavelengths, where the effect of dust extinction has less impact. However, the second challenge is more difficult to overcome. In seeing limited conditions, long exposure observations taken with the Keck telescopes have a resolution of only $0.''6$ instead of the diffraction limit of $0.''055$ for a 10 m telescope at 2.2 μm (an imaging technique called speckle imaging can achieve diffraction limited performance in seeing limited conditions, but only with very short, $\sim$ 0.1 s exposures, which severely limits sensitivity and spectroscopy). In order to correct for the blurring effects of the atmosphere, the technology known as adaptive optics (AO) has now been widely deployed on large ground based telescopes to achieve nearly diffraction limited performance at near-infrared wavelengths. AO relies on observing the effects of phase aberrations on bright star near the science target and then applying corrections to the phase errors by the use of a deformable mirror in the light path between the telescope and the science camera. While the AO system

at Keck performs very well next to bright optical guide stars, these stars are not uniformly distributed in the sky, thus limiting the number of science targets observable using this technique. In order to access more of the sky, it is possible to use a laser beam tuned to a wavelength of one of the atomic transitions of the sodium atom to stimulate emission in the sodium layer at $\sim$ 90 km in the Earth's atmosphere to create an artificial star. The laser guide star can then be used as a probe of atmospheric aberrations much like natural guide stars (with the exception of the effect of tip-tilt, which requires a natural guide star, though it can be much fainter when used in conjunction with a laser). Implementation of the laser guide star adaptive optics (LGS AO) system at Keck has greatly improved the sky coverage available for AO correction, including the Galactic center. Since 2004, when LGS AO observations of the Galactic center began, about a factor of 5 better astrometry has been achieved along with an increase in sensitivity of about 4 magnitudes over previous non-AO observations for imaging. The sensitivity for spectroscopy has also increased by about 3 magnitudes compared to pervious observations of this region. This increase in resolution and sensitivity has enabled a wider range of scientific observations at the very center of the Galaxy where the high density of sources have impeded study in the past. In particular, LGS AO has for the first time, enabled the observations presented in this thesis.

1.2 The near-infrared emission from Sgr A*

One of the most exciting results from the increase in sensitivity provided by AO observations of the Galactic center is the detection of variable infrared emission from the location of the radio source Sgr A* in 2003 (Genzel et al., 2003a). The infrared emission from material accreting onto the black hole was only recently

detected because the source is quite underluminous compared to those observed in the centers of other galaxies. In one of the first NIR detections of Sgr A*, Genzel et al. (2003a) reported a possible quasi-periodic (QPO) signal at $\sim$ 17 min in a light curve $\sim$ 3 hours long. One proposed model to explain the reported periodic signal is that it arises from the periodic Keplerian orbits of 'hot spots' of plasma at the last stable orbit around the black hole (Meyer et al., 2006). The last stable orbit for a non-spinning 4×10^6 $M_\odot$ black hole is $\sim$ 30 min; this period decreases for a maximally spinning black hole down to $\sim$ 15 minutes. If a QPO exists and can be modeled this way, a 20 min period would translate to a lower limit on the spin of Sgr A*, one of the fundamental properties of black holes. An alternative hypothesis for the variable flux emission is that the material falling into the black hole is experiencing hydrodynamical instabilities leading to changes in the brightness of the integrated light detected in the near-infrared. Flux variability of this form, termed "red noise", has been observed at the centers of other galaxies for many years. Red noise can mimic the behavior of periodic signals when the duration of the data set is only several times longer than the periodic signal. The first part of this thesis is to quantitatively establish the probability that the variability of Sgr A* is periodic. To do so, we have obtained some of the most photometrically sensitive light curves of Sgr A* from the Keck telescope and developed a statistical method for determining whether these light curves are consistent with red noise. Chapter 2 presents the result of monitoring Sgr A* as well as the corresponding statistical tests for periodic signals.

1.3 Dynamical evolution of stars at the Galactic center

At the center of the Galaxy lies one of the densest stellar clusters known to date, with a stellar density comparable to having a million stars between the sun and the nearest star. The dominant force influencing the long term dynamical behavior of this cluster is the gravitational potential from the supermassive black hole. The cluster in turn likely contributed to the buildup of mass of the black hole from stars whose orbits bring them close enough to be tidally disrupted. The absorption of stars by the black hole transfers the gravitational energy of the disrupted stars into the orbits of the remaining stars in the cluster, changing their dynamical properties and spatial distribution. These interactions result in a steady state distribution of stars that is very centrally concentrated (a cusp of stars), significantly different than a stellar system without a black hole at the center (Bahcall & Wolf, 1976). Briefly, the existence of a power cusp in the stellar density profile around a black hole can be understood as the result of the steady state configuration of a cluster with stars being absorbed by the black hole (Binney & Tremaine, 2008). We start by assuming that the density profile scales as a power law of radius:

$$n(r) \propto r^{-\gamma} \tag{1.1}$$

The velocity dispersion of the stars is given by the Jeans equations and should be on the order of $\langle v^2 \rangle \sim GM_\bullet/r$. The local relaxation time (the approximate amount of time for the cluster to erase the dynamical signatures of its formation through two body gravitational interaction between stars) is given by:

$$t_{relax} = 0.34 \frac{\sigma^3}{G^2 m \rho \ln \Lambda} \tag{1.2}$$

Substituting $\langle v^2 \rangle$, and ignoring the Coulomb logarithm ($\ln \Lambda$, a constant):

$$t_{relax} \approx \frac{\langle v^2 \rangle^{3/2}}{G^2 m^2 n} \propto r^{\gamma - 3/2} \tag{1.3}$$

A star that reaches the tidal radius, $r_\bullet$ of the black hole will essential be removed from the star cluster, resulting in the loss of energy from the cluster on the order of $E(r) = -GM_\bullet m/r_\bullet$. This implies a flow in energy in the system, and the number of stars interior to a radius, r can carry out energy on the order of $N(r)E(r)$ through a shell of radius r per relaxation time. With $N(r) \propto r^{3-\gamma}$:

$$N(r)E(r)/t_{relax} \propto r^{-2\gamma + 7/2} \tag{1.4}$$

In a steady state, the flow of energy needs to be independent of radius, which results in $\gamma = 7/4$. This is the same cusp slope determined by Bahcall & Wolf (1976) more rigorously for a single mass stellar system around a black hole. When including multiple stellar masses, Bahcall & Wolf (1977) found that the density cusp slope can be as shallow as $\gamma = 3/2$.

The prediction of a cusp profile in a dynamically relaxed star clusters with a black hole at the center has been reproduced robustly through many theoretical studies over the years, including Fokker-Planck calculations and N body simulations, even with the addition of dynamical effects such as mass segregation and stellar collisions (e.g., Bahcall & Wolf, 1977; Murphy et al., 1991; Alexander & Hopman, 2008). These studies have been used as inputs into simulations when the mass density near a black hole is required, such as in simulations of the growth of massive black holes or as the background mass distribution for the study of dynamics near a massive black hole. The sea of stars in the cusp act as a source of dynamical friction in the system, enabling the in-spiral of compact objects such

as neutron stars, stellar mass black holes, and even other massive black holes by removing some of the angular momentum of the in-falling objects. The rate of in-spiral of compact objects in particular strongly influences the frequency and strength of gravitational waves, which a number of large physics experiments like LIGO are trying to detect from the Galactic center. The existence of a stellar cusp may also be important in informing our understanding of other unresolved phenomena at the Galactic center, such as the existence of the young stars located within 0.04 pc of the black hole. These young stars could not have formed at their present location because the tidal field of the black hole would shear apart any molecular clouds before they could collapse to form stars. One of the theories to explain their presence posits that they were ejected from a larger population of young stars at 0.5 pc that were originally formed in a self-gravitating disk. The distribution of S-stars seen today could have been the result of dynamical interaction between the orbits of the stars in the disk and the stellar cusp, with the cusp of stars providing a source of dynamical friction and torque to change both the orbital plane and angular momentum of disk stars to bring them closer to the black hole (Madigan et al., 2009).

While these theories rely the existence of a stellar cusp around massive black holes, stellar cusps have been difficult to observationally verify. The challenge lies in finding a dynamically relaxed star cluster with an independently confirmed black hole sufficiently nearby to use number counts to determine the stellar density within the sphere of influence the black hole; the latter criteria is difficult to fulfill except in the local universe as the radius of influence is only about 1-2 pc for an $\sim 4 \times 10^6\ M_\odot$ black hole. Both of these difficulties can now be overcome when observing the Galactic center, which has a well determined black hole mass and the advent of LGS AO has allowed us to count individual stars down to 0.004 pc of the black hole. Recent studies of the Galactic center used star

counts from images to infer the spatial distribution of stars in the cluster (Schödel et al., 2007). Schödel et al. (2007) found that the density of stars rose toward the center, but perhaps was not rising as steeply as predicted. One difficulty in interpreting this result is that stellar counts from imaging alone do not provide sufficient information about the age of the stars. This distinction is critical at the Galactic center given recent star formation in this region 6 million years ago that resulted in a substantial number of high mass young stars. These stars have not had enough time to reach a dynamically relaxed state with respect to the black hole, so their distribution should not be expected to follow the predictions from Bahcall & Wolf (1976). In order to remove this bias, only old stars that have had time to dynamically relax (> 1 billion years) should be considered in the density profile measurements.

For the second part of this thesis, we conducted a spectroscopic survey of the central ~ 0.16 pc of the Galaxy, in order to separate the young stars from the old. The survey is sensitive to stars as faint as Kp = 15.5 mag, which at the distance to the Galactic center, corresponds to an old K or M type red giant or a young B-type main sequence star (Figure 1.1 shows a theoretical color magnitude diagram in the near-infrared of stars at the Galactic center). While these two classes of stars have similar observed brightnesses, their temperature, hence spectral features are quite different, making it possible to select only old, and presumably dynamically relaxed, stars to measure the density profile of the cusp. In Chapter 3, we present the resulting measurements the stellar population in this region along with the density profile of the old stars. We also discuss some possible dynamical scenarios that may have lead to the observed profile. In Chapter 4, we present several methods that can be used to incorporate kinematic information to further constrain the three-dimensional distribution of stars.

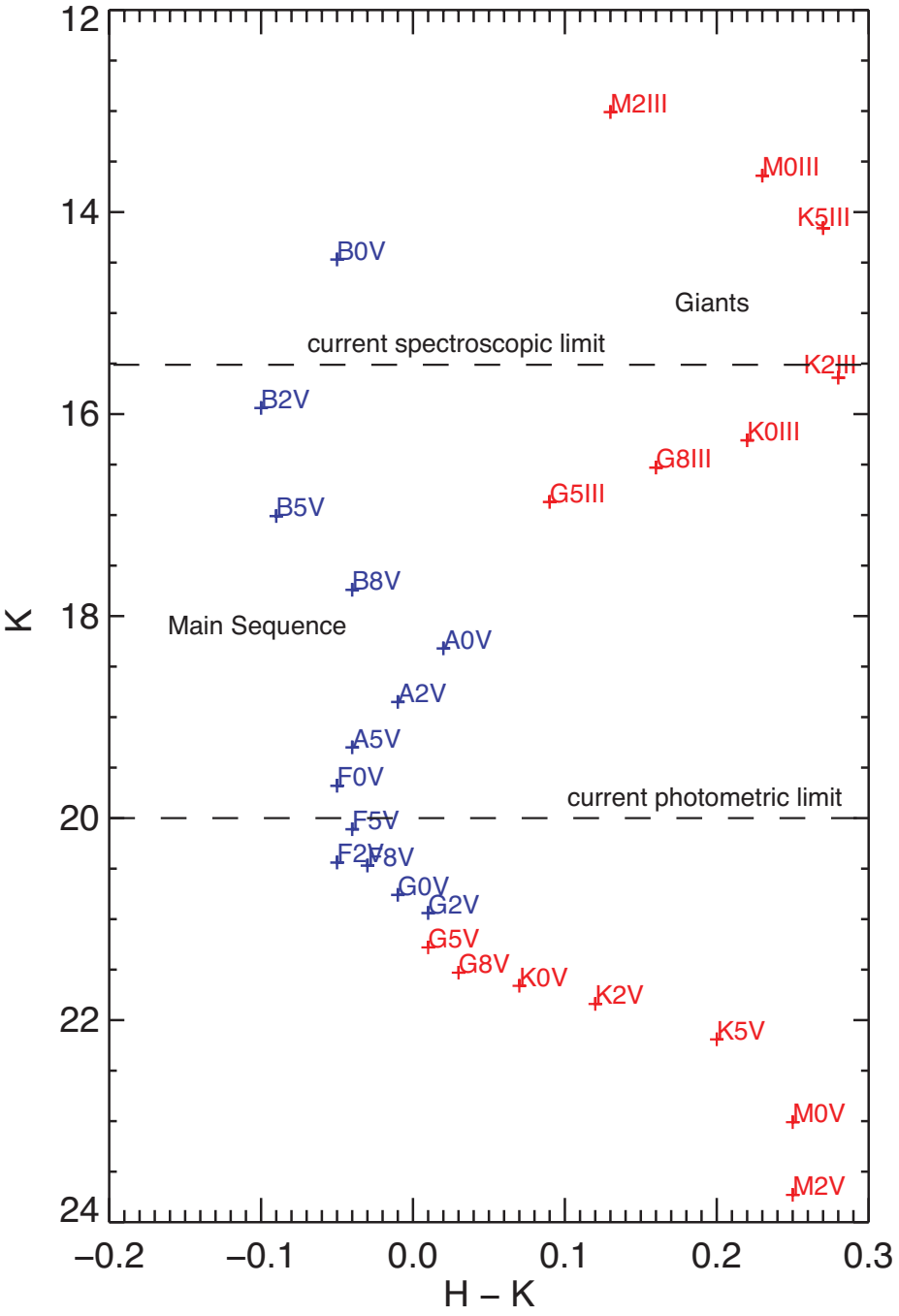

Figure 1.1 Theoretical color magnitude diagram of the Galactic center in the NIR showing the expected observed Kp magnitude for stars of different spectral types behind 3 magnitudes of extinction at Kp and at 8 Kpc (the H-K colors are intrinsic colors). Given our current spectroscopic capabilities, we are sensitive to either K to M-type giants (~ 1 $M_\odot$, > 1 Gyr old) or early B-type main sequence stars (~ 20 $M_\odot$, < 100 Myr old).

CHAPTER 2

Near-IR variability of Sgr A*: a red noise source with no detected periodicity

The existence of a super-massive black hole with a mass of $\sim 4 \times 10^6 M_\odot$ at the center of the Galaxy has now been firmly established from monitoring the orbits of the stars in the near-infrared (NIR) within 1 arcsecond of the location of the associated radio source Sgr A* (e.g. Schödel et al., 2002, 2003; Ghez et al., 2003, 2005b, 2008). Multi-wavelength detections of the radio point source at sub-millimeter, X-ray, and infrared wavelengths have also been made, showing that the luminosity associated with the black hole is many orders of magnitudes below that of active galactic nuclei (AGN) with comparable masses (Melia & Falcke, 2001). These observations have also shown that the emission from Sgr A* is variable (e.g., Baganoff et al., 2003; Mauerhan et al., 2005; Eisenhauer et al., 2005; Hornstein et al., 2007; Marrone et al., 2007; Eckart et al., 2008). Although it is now easily detected in its bright states when its flux increases by up to an order of magnitude over time scales of 1 to 3 hours, Sgr A* is difficult to detect in its faintest states at X-ray wavelengths because of the strong diffuse background, and in the near-infrared because of confusion with nearby stellar sources (Baganoff et al., 2003; Hornstein et al., 2007). Advances in adaptive optics (AO) technology have offered improved sensitivity to infrared emission from the location of Sgr A* against the stellar background, such that observations in its faint states are now

possible (Ghez et al., 2005a). Hereafter, the IR-luminous source Sgr A*-IR will be referred to simply as Sgr A*, recognizing that it is likely to be coincident with the radio source of that name.

At both NIR and X-ray wavelengths, a possible quasi-periodic oscillation (QPO) signal with a $\sim$ 20 min period has been reported in light curves of Sgr A* (Genzel et al., 2003a; Aschenbach et al., 2004; Eckart et al., 2006b). Models that aim to produce QPO signals include both a class of models involving the Keplerian orbits of 'hot spots' of plasma at the last stable orbit (Meyer et al., 2006; Trippe et al., 2007) as well as models with rotational modulations of instabilities in the accretion flow (Falanga et al., 2007). Since the orbital period at the last stable orbit of a non-spinning black hole is 32 ($\mathrm{M}_{bh}/4.2 \times 10^6 M_\odot$) min, this putative periodic signal has been interpreted as evidence for a spinning black hole. The challenges for these claims are the relatively short time baselines of the observations (only a few times the claimed period), the low amplitude of the possible QPO activity, and the level of rigorous assessment of the statistical significance of the claimed periodicity.

An alternative explanation for peaks in the periodograms seen in previous studies and interpreted as a periodic signal is that they are a sign of a frequency dependent physical process, commonly known as red noise (Press, 1978). The power spectrum of such a physical process will display an inverse power law dependence on frequency, which manifests as light curves with large amplitude variations over long time scales and small amplitude variations over short time scales. The power spectrum of any individual realization of a red noise light curve will show statistical fluctuations around the intrinsic power law function, creating spurious peaks that can lead to an interpretation of periodic activity. Variability studies of other accreting black hole systems like AGNs and Galactic

X-ray binaries have shown that their power spectral densities are consistent with red noise. Several physical models have been proposed to produce the red noise light curves seen in AGNs (e.g. Lyubarskii, 1997; Armitage & Reynolds, 2003; Vaughan et al., 2003); one common model that results in a red noise spectrum is from fluctuations in the physical parameters, such as the gas densities and accretion rate, at different radii of a turbulent magnetohydrodynamic accretion disk (Kataoka et al., 2001). While QPO signals have been unambiguously confirmed in X-ray binaries, no QPO signals in AGNs have been shown to be statistically different than red noise (Benlloch et al., 2001; Vaughan, 2005). Recent work by Bélanger et al. (2008 in prep) have also shown that a statistical analysis of X-ray light curves of Sgr A*, when including the contribution from red noise, show no indications of a QPO signal.

High sensitivity and high angular resolution near-infrared observations of Sgr A* have been obtained at the Keck II telescope utilizing new improvements in adaptive optics technologies to investigate the existence of a QPO signal as well as the timing properties of Sgr A*. These observations are described in Section 3.2. In order to test whether the variability of Sgr A* has the characteristics of red noise and to examine the possibility of a periodic signal, we have carried out a statistical analysis of the timing properties of the observed light curves that includes the possible contribution of red noise in the power spectrum to establish the significance of peaks in the periodograms. We find that the near-infrared variability of Sgr A* is entirely consistent with red noise, with no periodic signals detected on any night. Sections 2.2.2.1 details our analysis of the light curves. Lastly, in Section 2.3, we discuss the implications of our results for Keplerian models of the Sgr A* flux variability and compare the timing properties of Sgr A* with those of AGNs.

2.1 Observations and Data Reduction

The Galactic center has been extensively imaged between 2005 and 2007 with the Keck II 10 m telescope using the natural and laser guide star adaptive optics (NGS and LGS AO) (Wizinowich et al., 2006; van Dam et al., 2006) system and the NIRC2 near infrared camera (P.I. K. Matthews). For this study we include all nights of LGS-AO observations at K' (2 μm) that had sampling of 1-3 minutes, a total time baseline of at least $\sim$ 1 hour, and at least 60 data points. We also include one night of NGS observations at L' that satisfied the same criteria. As summarized in Table 3.1, this resulted in a selection of 7 data sets with durations ranging from 80 min to 3 hours.

A detailed description of LGS AO observations of the Galactic center are described in Ghez et al. (2005a); here, we only summarize the setup for our observations. The laser guide star was propagated at the center of our field and for low order tip-tilt corrections, we used the $R = 13.7$ mag star, USNO 0600-28577051, which is located $\sim 19''$ from Sgr A*. Most of the images were obtained using the K' band-pass filter ($\lambda_o = 2.12$ μm, $\Delta\lambda = 0.3$ μm) and were composed of 10 coadded 2.8 sec exposures, for a total integration time of 28 sec. The remaining set of observations from 2005 July 28 was taken through the L' band-pass filter ($\lambda_o = 3.78$ μm, $\Delta\lambda = 0.7$ μm). For five of the K' nights, the time interval between each image is about 50 seconds, with dithers every three minutes. K' images from 2006 July 17 were sampled at 3 minute intervals but were not dithered. The L' observations had one minute sampling, and were also not dithered. The 3 min dithers affect the timing analysis by the presense of a spike at that frequency in the periodograms (this is well reproduced by Monte Carlo simulations of the effects of sampling).

Photometry was performed on the individual images using the point spread

Table 2.1. Summary of Observations of Sgr A*

Date (UT)	Filter	Start Time (UT)	End Time UT	N_{obs}	Median Samp. (sec)	Duration (min)	Dithered[a]	Strehl[b] (%)	FHWM[a] (mas)	Mean Flux[c] (mJy)	σ[b] (mJy)	S0-17$_{phot}$[d] %	S2-133$_{phot}$[d] %
2005 July 28[e]	L′	06:10:52	09:09:23	144	69	180	No	70	81	4.74	1.7	...	...
2006 May 03	K′	10:54:30	13:14:12	116	51	140	Yes	34	60	0.29	0.15	7	13
2006 June 20	K′	08:59:22	11:17:54	70	51	79	Yes	24	71	0.24	0.18	7	22
2006 June 21	K′	08:52:26	11:36:53	164	51	164	Yes	33	61	0.19	0.07	4	17
2006 July 17[f]	K′	06:45:29	09:54:03	70	147	189	No	35	59	0.15	0.05	5	22
2007 May 18	K′	11:34:10	13:52:39	77	51	84	Yes	36	59	0.29	0.14	7	10
2007 August 12	K′	06:67:10	07:44:38	62	51	57	Yes	33	58	0.16	0.02	4	7

[a]When the observations are dithered, the time interval between dithers is 3 min.

[b]Average for the night. Strehl ratios and FWHM measurements made on IRS 33N for all K′ data and IRS 16C for L′ data

[c]Flux values are observed fluxes, not de-reddened.

[d]Photometric precision for the two comparison sources S0-17 and S2-133, with mean fluxes 0.38 mJy and 0.15 mJy respectively.

[e]NGS mode

[f]Previously reported in Hornstein et al. (2007)

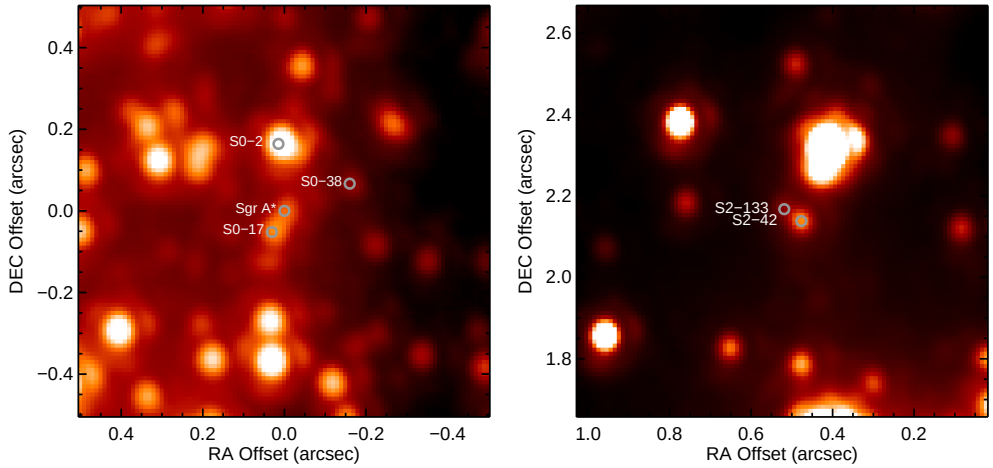

Figure 2.1 **Left**: a K' image from 2006 May 3 of the central 0.″5 around Sgr A* with a logarithmic intensity scale so that the faint sources can be more easily seen. Sgr A* (K′ = 15.8 in this image) is in the center of the image along with the comparison stars, S0-2, S0-17 and S0-38. The image is oriented with north up and east to the left, with offsets in projected distance from Sgr A*. **Right**: image from the same night of the pair of comparison sources, S2-42 ($K' = 15.5$) and S2-133 ($K' = 16.7$), with a flux ratio similar to that of S0-17 and Sgr A* when Sgr A* is faint. These two stars also has a similar separation in the plane of the sky as S0-17 and Sgr A* (∼50 mas).

function (PSF) fitting program *StarFinder* (Diolaiti et al., 2000). The program was enhanced as described in Hornstein et al. (2007) to include the *a priori* knowledge of the location of the near-infrared position of Sgr A* and nearby sources in order to facilitate the detection of Sgr A* at faint flux levels in these short exposures. To do this, for each night of observation, the position of Sgr A* and nearby sources was determined in a nightly-averaged image produced by a weighted average of individual images from that night (see Figure 2.1). We then used the knowledge of the location of all the sources as fixed inputs into *StarFinder* to more accurately fit for the flux contribution of sources near Sgr A* in the individual short exposure images. To compensate for seeing changes through the night, a different PSF was constructed for each image. We also include only images with Strehl ratios greater than 20% to minimize large errors

in the photometry from bad seeing conditions, which resulted in dropping only about 10 data points out of all nights. On average, the Strehl ratio at K' was 32%, with the full width of the core at half-maximum intensity (FWHM) $\sim$ 60 mas as measured from the relatively isolated star IRS 33N. We are able to detect Sgr A* at all times, even at its faintest flux levels. The gaps in the data are from technical disruptions in the observations.

Photometric calibrations were performed relative to the list of non-variable sources from Rafelski et al. (2007) at K' and IRS 16C ($L' = 8.14$ mag) and IRS 16NW ($L' = 8.43$ mag) at L' (Blum et al., 1996). The photometric error at each flux density level seen in Sgr A* was estimated by fitting a power law to the rms uncertainty in the flux for all non-variable stars in the same range of brightnesses observed for Sgr A* within $0.''5$ of the black hole (see Figure 2.2). We find the typical dependence of the photometric error, σ, on flux density, F, to be: $\sigma \approx 0.2F^{0.3}$ mJy. The flux measurement uncertainties are comparable for all nights except 2006 June 20, the night with the worst seeing. Within the range of observed Sgr A* fluxes, we are on average able to achieve between 3 to 15% relative photometric precision for each 28 sec K' exposure. A source of systematic error in the flux measurements is the proximity of Sgr A* to unresolved sources, which could contribute flux. This contribution is only likely to have an impact when Sgr A* is faint (Hornstein et al., 2007), but for the purpose of this variability study, this effect is likely only a systematic offset in the mean flux density and a source of white noise (for more details, see Section 2.2.1). For comparison to Sgr A*, we also analyze the light curves of the nearby stars S0-17 and S0-38 at K' and S0-2 at L'. S0-17 ($K' = 15.5$ mag) was chosen because it is spatially closest to Sgr A*, with a projected distance from Sgr A* of $\sim$ 56 mas in 2006 May to $\sim$ 48 mas in 2007 August; monitoring S0-17 is helpful to ensure that the variations in flux seen in Sgr A* are not a systematic effect of seeing or bias from

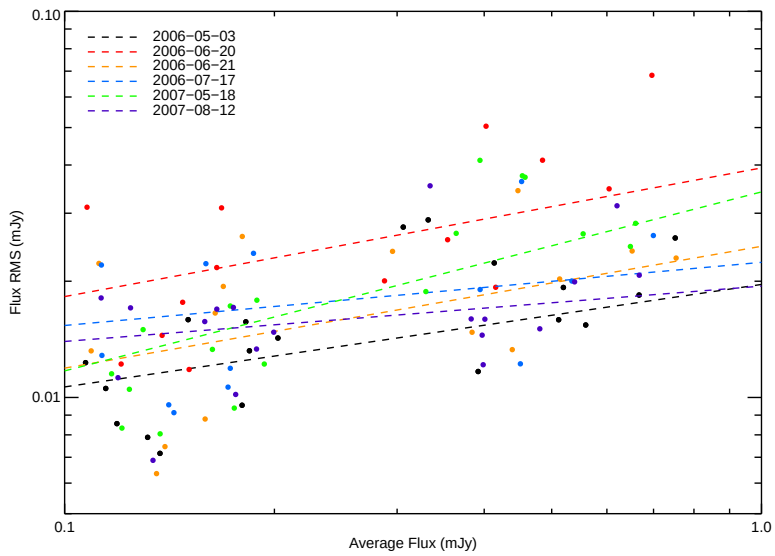

Figure 2.2 Plot of power law fits to the rms fluxes for stars within 0.″5 of Sgr A* with brightnesses within the range of observed brightness variations in the K' light curves from Sgr A*. The photometric noise properties are similar for each night.

nearby sources. The star S0-38 ($\sim$ 0.11 mJy, $K' \sim 17$ mag), $\sim 0''.2$ from Sgr A*, was chosen as a stellar reference because it has a similar flux to the faintest observed emission and given its proximity to Sgr A*, its photometry will be affect similarly from the unresolved stellar background. Figure 2.1 shows an image of this region and the location of the comparison sources with respect to Sgr A*.

In order to characterize possible effects on the photometry of Sgr A* by S0-17, we also use the photometry of two stars with separations and flux ratios similar to that of S0-17 and Sgr A* when Sgr A* is faint. The two stars, S2-42 (K′=15.5) and S2-133 (K′=16.7), are located about $2''$ from Sgr A* and are separated by $\sim$ 50 mas (Figure 2.1). The rms variability of S2-42 and S1-133 is about 5% and 15%, respectively, similar to the photometric precision we would have predicted based upon our power law fits to the rms stability of stars near Sgr A*. Thus, we can be confident that the photometry of Sgr A* at its faintest is similar to stars

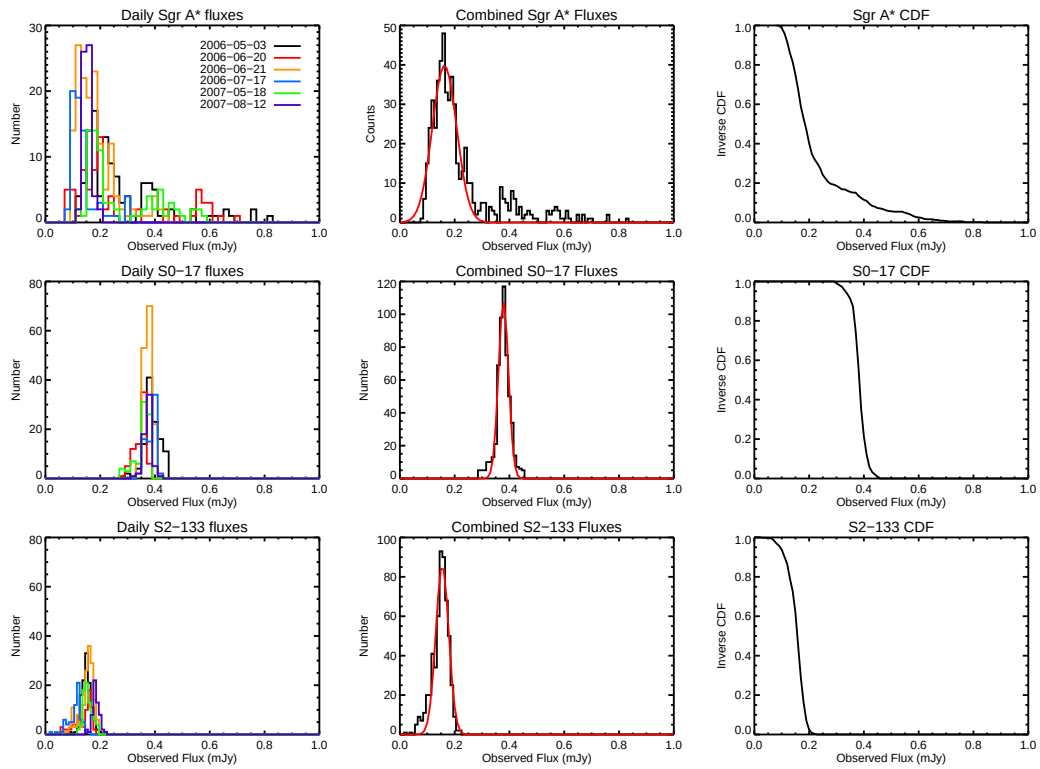

Figure 2.3 **Top**: Sgr A* flux distribution for each of the 6 K' nights (left), the combined fluxes from all nights (middle), and the inverse cumulative distribution function for the combined fluxes (right). **Middle**: The corresponding plots for S0-17, the non-variable comparison source used in this study. The total histogram of fluxes observed from S0-17 is consistent with a single Gaussian. **Bottom**: the flux distribution for S2-133, a $K' = 16.7$ magnitude star for comparison with the faint states of Sgr A*.

of that magnitude despite the proximity of S0-17.

2.2 Results and Analysis

2.2.1 Flux Distribution

In order to characterize the range of fluxes observed from Sgr A*, we have constructed histograms of fluxes from each night as well as the combined histogram

from all nights (Figure 2.3). Unless otherwise stated, the fluxes in this paper are observed fluxes and not corrected for extinction to Sgr A*. Where indicated, de-reddened fluxes have been calculated by assuming $A_v = 30$ (Moneti et al., 2001) and extinction law $A_{K'} = 0.1108 A_v$ (Rieke & Lebofsky, 1985). The comparison sources do not appear to be variable on the time scales probed in this study and have fluctuations consistent with Poisson noise. The flux distribution for the star S0-17 is consistent with a Gaussian centered at 0.37 mJy at K', with a standard deviation of 0.02 mJy; this suggests that we are able to reproduce the flux of S0-17 at the 5% level between different nights. A bias in the photometry from the proximity of S0-17 to the light curve from Sgr A* should manifest itself as a difference in the mean flux of S0-17 between 2006 and 2007 because S0-17 moved closer to Sgr A* in the plane of the sky between the two years. The fact that we observe the same mean flux from S0-17 between different years is also confirmation that there is little bias in the photometry of either S0-17 or Sgr A*. The light curves of S0-17 are also stable on each night, independent of the flux of Sgr A* and shows no greater variance than other stars of the same brightness in the region (within $0.''5$ of Sgr A*), showing that PSF fitting from *StarFinder* is able to able to properly account for the flux of both sources.

The cumulative distribution function for Sgr A* shows that it is brighter than S0-17 about 15% of the time at K'. The median flux density of Sgr A* is at 0.192 mJy ($K' = 16.3$ mag), or a de-reddened flux of 4.10 mJy. The flux histogram for Sgr A* is not well fitted by a Gaussian because it has a long tail in the distribution of flux densities at high flux densities. However, if the tail of the distribution is excluded, the flux distribution below 0.3 mJy, is well fit by a Gaussian with a mean of 0.158 mJy and a standard deviation of 0.05 mJy. The latter is larger than nearby sources with comparable flux densities, indicating that Sgr A* is intrinsically variable; for example, the flux distribution for S2-133 has a FWHM

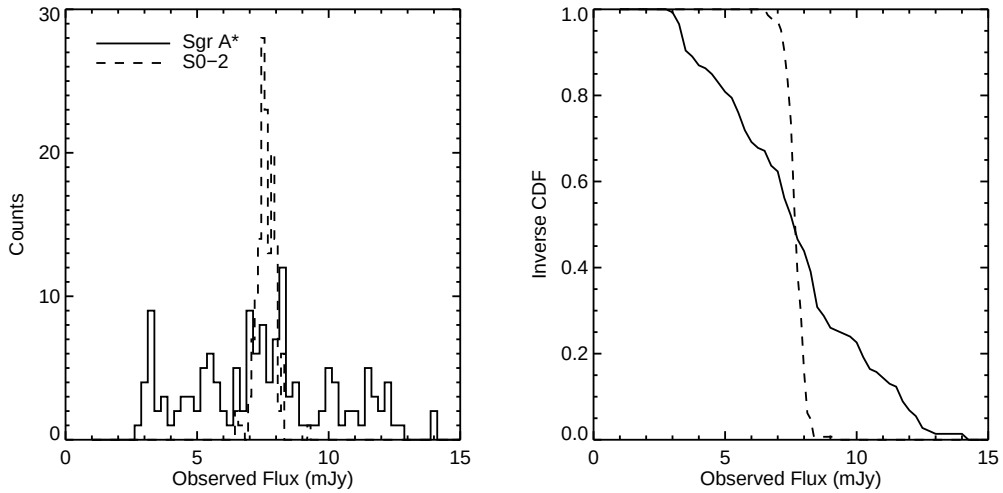

Figure 2.4 **Left** - Sgr A* and S0-2 flux distributions on the night of 2005 July 28 at L' . **Right** - the corresponding cumulative distribution function for Sgr A* and S0-2. Both CDFs are consistent with Gaussian distributions.

of ~ 0.02 mJy (see Figure 2.5).

The flux density distribution of Sgr A* for the L' night shows a much larger width than the comparison star S0-2 (Figure 2.4). The distribution appears to be symmetric about the mean and the CDF is consistent with a Gaussian with mean flux density of 7.69 mJy with $\sigma = 2.81$ mJy, compared to S0-2 with a mean flux density of 7.67 mJy with $\sigma = 0.37$ mJy.

While the bright flux levels (> 0.3 mJy) can be unambiguously attributed to the black hole, the source of emission from the location of Sgr A* when it is faint is less certain. The region immediately around Sgr A* is also the location of peak stellar density, which raises the possibility of flux contamination from either an unresolved population of stars or a very faint star in a close orbit at that location. We find that the faintest observed flux density at K' is 0.082 ± 0.017 mJy ($K' = 17.2$) or 1.75 ± 0.36 mJy de-reddened from the location of Sgr A* (consistent with limits observed by Hornstein et al. (2002)). Comparison of the

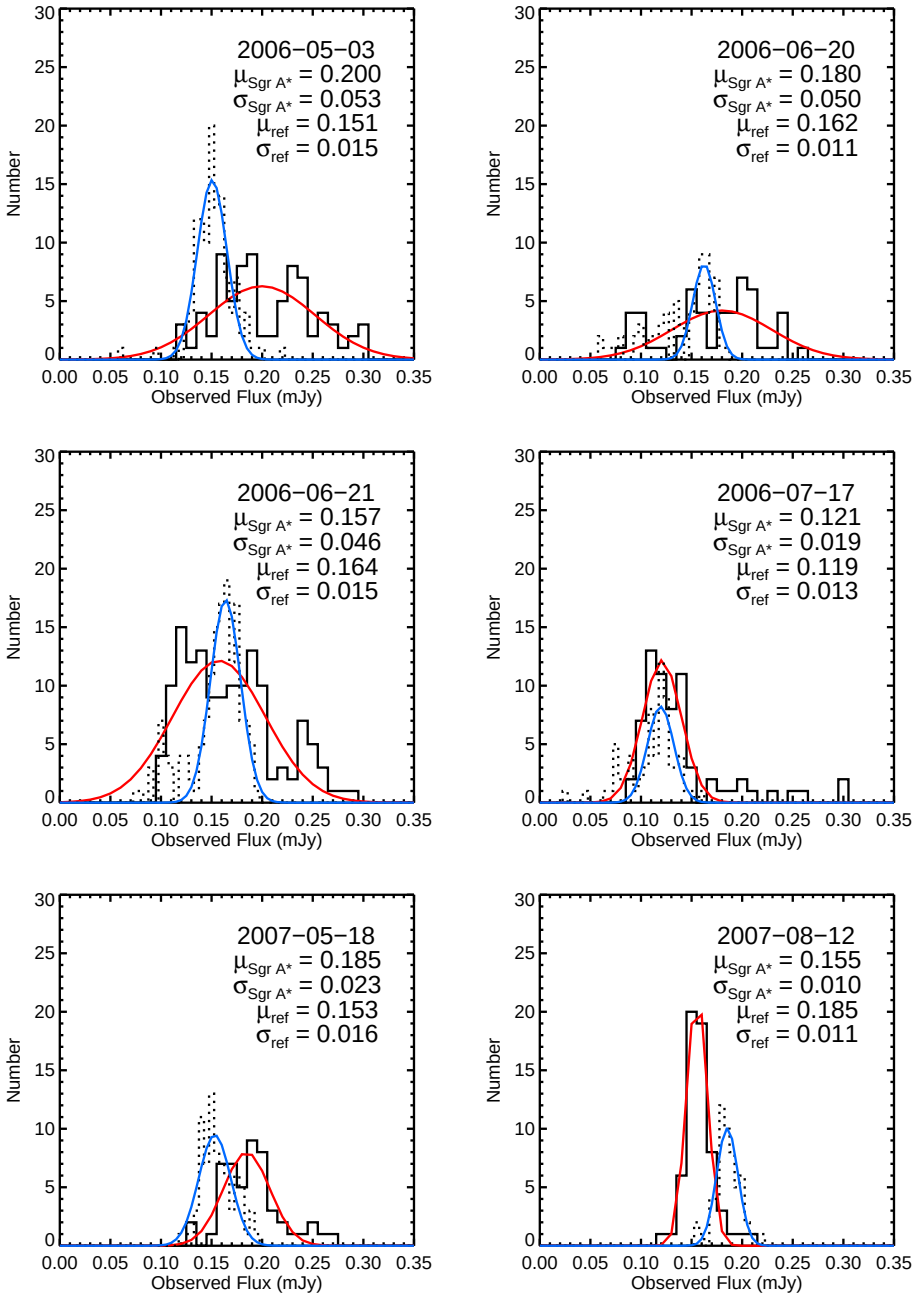

Figure 2.5 The flux distribution of Sgr A* (solid) of fluxes less than 0.3 mJy and the reference source, S2-133 (dotted) for each night along with the best fit Gaussian. On four of the six K' nights, the width of the Sgr A* flux distribution is greater than the reference, while in the remaining two nights, the widths are comparable. Labels are units of mJy.

flux distribution of S2-133 with that of Sgr A* below 0.3 mJy shows that, for four of the six K' nights, Sgr A* has a larger variance than S2-133 (see figure 2.5), indicating that Sgr A* is more variable than expected for a stellar source even at the faintest levels. On the remaining two nights, the variance of Sgr A* is similar to that of S2-133. On one of these two nights, 2007 August 12, Sgr A* was fainter than 0.22 mJy for the entire duration of our observation, which makes this night ideal for timing analysis of Sgr A* at its faintest flux density levels. Though the flux distribution looks similar to a star, the structure function and the periodogram shows a slightly steeper slope than expected for Gaussian noise and as compared to the stellar stellar comparison sources (see Sections 2.2.2.1 and 2.2.2.2). Furthermore, the $K' - L'$ color for 2006 July 17, previously reported in Hornstein et al. (2007), is constant and significantly redder, even at its faintest on that night, than from a stellar source. At the faintest fluxes, between 0.10 and 0.15 mJy, the mean $K' - L'$ spectral slope, corrected for extinction, of Sgr A* has an average power law exponent of -0.17±0.32, compared to a slope of -0.6 ± 0.2 from Hornstein et al. (2007). We estimate that a stellar source, which would have de-reddened spectral slope of 2, could contribute a maximum of about 35% of the flux to account for the difference in the spectral slope. This leads us to conclude that, even when the emission is faint, a large fraction of the flux arising from the location of Sgr A* is likely non-stellar and can be attributed to physical processes associated with the black hole.

2.2.2 Light Curves and Timing Analysis

Figures 2.6 and 2.7 shows the resulting light curves for Sgr A* and a non-variable comparison source for each night of observation. While comparison sources show no significant time variable emission, Sgr A* shows variations on time scales

ranging from minutes to hours, with peak emission that can be 10 times higher than during its faintest states. The emission peaks are time symmetric, with similar rise and fall times.

In order to characterize the variability of Sgr A*, we have carried out the following three different approaches to timing analysis: (1) periodograms (2) structure functions and (3) auto-correlations. The periodogram analysis, presented in section 2.2.2.1, is effective at pulling out periodic structure in light curves and therefore is optimal for assessing the presence of any periodicities, such as the proposed $\sim$ 20 min QPO reported in previous experiments (e.g., Genzel et al., 2003a; Eckart et al., 2006b). Both the periodogram and the structure function can also be used to measure the underlying power spectral density (PSD), which can then be used to explore similarities to the variability observed in AGNs. We also compute the auto-correlation for each night to look for possible differences in the variability at each time scale between each night.

2.2.2.1 Periodogram

It is important to consider all possible sources of noise when testing for periodicity in light curves. While peaks in the periodograms are a good place to start searching for periodicity, the peaks must have significantly more power than those produced by non-periodic processes to be unambiguously attributed to a true periodicity in any variable source. White (Gaussian) noise processes are unlikely to lead to large peaks in the periodograms because they contribute equal power at all frequencies. However, time-correlated physical processes can result in variability that is frequency dependent. One common variability characteristic - often seen in AGN light curves - is red noise, which can lead to spurious signals in a power spectrum or periodogram from a data set having a time baseline only a few times

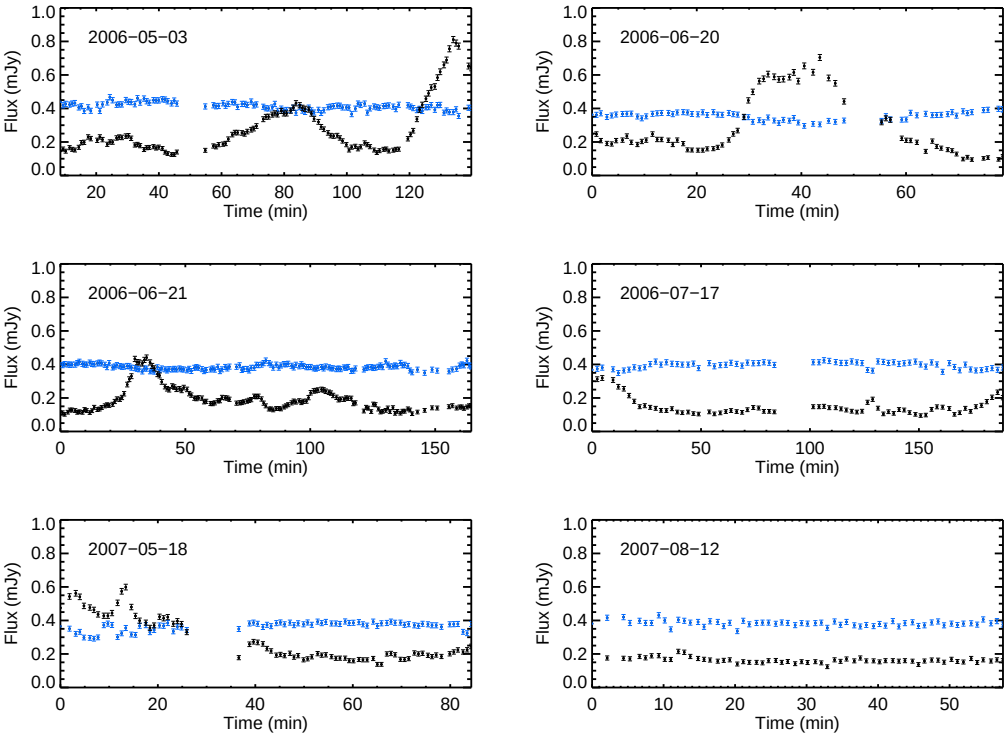

Figure 2.6 Sgr A* light curves (black) at K' with the star S0-17 (blue) for comparison.

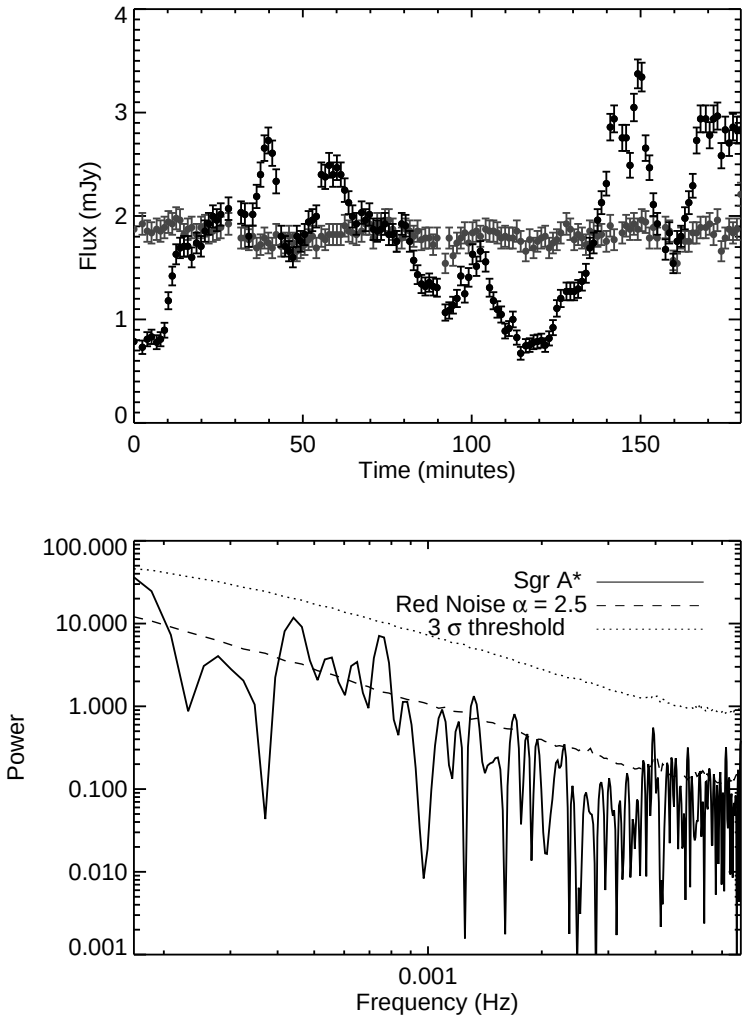

Figure 2.7 **Top:** The light curve of Sgr A* (black) and comparison source S0-2 (grey) at L' on 2005 July 28. **Bottom:** Normalized Lomb-Scargle periodograms of Sgr A* on this night (black). Also plotted is the 3 σ significance threshold determined from Monte Carlo simulations of red noise with a power law index, $\alpha = 2.5$ (dotted). The average of 10^5 periodograms with $\alpha = 2.5$ at the same time sampling is also shown for comparison (dashed line).

longer than that of the putative period, since it will show large amplitude fluctuations at low frequencies and small amplitudes at high frequencies. This can lead to relatively large stochastic peaks in the power spectrum at low frequencies, far above what would be expected from white noise. We emphasize that, although the term for this type of power law dependence of the flux variability is 'red noise', this variability arises from physical processes from the source and is not a result of measurement uncertainties such as Poisson noise, which behaves like white noise in its power spectrum.

One of the goals in this timing analysis is to test whether a purely red noise model can explain the variability of Sgr A*. The PSD of a red noise light curve is a power law, with greater power at lower frequencies: $P(f) \equiv f^{-\alpha}$, where f is the frequency and α is the power law index. For example, $\alpha = 0$ for white noise and $\alpha = 1$ for classical flicker noise (Press, 1978). All red noise simulations in this paper were produced by an algorithm detailed in Timmer & Koenig (1995), which randomizes both phase and amplitude of an underlying power law spectrum and then inverse Fourier transforms it into the time domain to create light curves. Our procedure for producing simulated light curves is as follows: (1) a light curve is produced from a PSD with a specific power law slope evenly sampled at half the shortest observed time sampling interval, with a duration at least 10 times as long as the observed light curve (rounded up to the nearest power of 2 for computational efficiency of the fast Fourier transform). This length was chosen based upon the suggestion by Uttley et al. (2002) to avoid a 'red noise leak' where power is distributed from frequencies lower than that sampled by the observation into observed frequencies. We find aliasing to be a negligible effect, because the light curves are generated at higher temporal resolution than the observations. (2) this light curve is then split into 10 non-overlapping segments to reduce simulation time (Uttley et al., 2002). Each segment is then re-sampled

at the exact sampling times used during the specific night that we are simulating. (3) since the simulation has an arbitrary flux scale, we scale the light curves to have the same mean flux level and standard deviation as that night. We also include the effects of measurement noise in the simulations by adding Gaussianly distributed noise to each simulated data point. We use our measurements of the photometric error as a function of flux densities (Section 3.2) of non-variable stars within $0''.5$ of Sgr A* to account for the flux density dependence in the noise for each simulated data point.

Instead of computing the PSD, which is often used for evenly sampled data, we searched for periodicity by computing a related function for unevenly sampled data: the normalized Lomb-Scargle periodogram (Press & Rybicki, 1989); given a set of data values h_i, $i = 1, \ldots, N$ at times t_i the periodogram is defined as:

$$P_N(\omega) \equiv \frac{1}{2\sigma^2} \left\{ \frac{[\sum_j (h_j - \overline{h}) \cos \omega (t_j - \tau)]^2}{\sum_j \cos^2 \omega (t_j - \tau)} + \frac{[\sum_j (h_j - \overline{h}) \sin \omega (t_j - \tau)]^2}{\sum_j \sin^2 \omega (t_j - \tau)} \right\} \tag{2.1}$$

where ω is the angular search frequency, $\overline{h}$ and σ^2 are the mean and variance of the data respectively. The constant τ is an offset introduced to keep the periodogram phase invariant:

$$\tan(2\omega\tau) = \frac{\sum_j \sin 2\omega t_j}{\sum_j \cos 2\omega t_j} \tag{2.2}$$

Since the periodogram is normalized by the variance of the flux, a light curve consisting of only white noise, or equivalently, red noise with a power law $\alpha = 0$, will have an average power of 1 at all frequencies.

The normalized Lomb-Scargle periodogram was computed for each light curve, oversampled by a factor of 4 times the independent Fourier intervals in order to increase the sensitivity to periods between the Fourier frequencies (Figures 2.7

and 2.8). Assuming that the physical source of the variability is stationary, we averaged together the periodograms for the five K' nights which have durations longer than 80 minutes (Figure 2.9). The combined periodogram excludes the 2007 August 12 night because it is less than an hour long, leading to poor sampling at low frequencies compared to the other nights. We combined the periodograms by averaging the Lomb-Scargle power at linearly space frequency bins. The combined periodogram is consistent with red noise, except for the peak corresponding to the time scale of the three minute dithers. To characterize the underlying spectrum, we have performed Monte Carlo simulations combining red noise light curves with the same sampling as the data set. We tested several different underlying PSD and found that the combined periodogram is consistent with power law indices between 2.0 and 3.0, with no periodic components. This model is able to reproduce the slope of the periodogram, the increase in power at three minutes from dithering, and the flattening of the periodogram at very low frequencies caused by poor sampling at those frequencies. The 3 min peak in the periodogram is repoduced very well by the simulations, showing that the simulations are correctly accounting for the effects of sampling. Figure 2.9 shows the results of Monte Carlo simulations with power law indices 1.5, 2.0, 2.5, and 3.0. The simulations shows that the resulting periodograms tend to be flatter than the intrinsic PSD because the limited time sampling at low frequencies results in poor sensitivity to long time scale variations characteristic of steeper power laws. Because the periodogram sampling is poor at frequencies below 40 min we will ignore those frequencies in all subsequent analysis. We find the resulting periodograms show less variation for intrinsic PSD $\alpha > 2$, which suggests that we have a better constraint on the lower limit than on the upper limit of our estimate for the slope of the PSD. While red noise models with values of α between 2.0 to 3.0 appear to be consistent with the average periodogram, we will use $\alpha = 2.5$

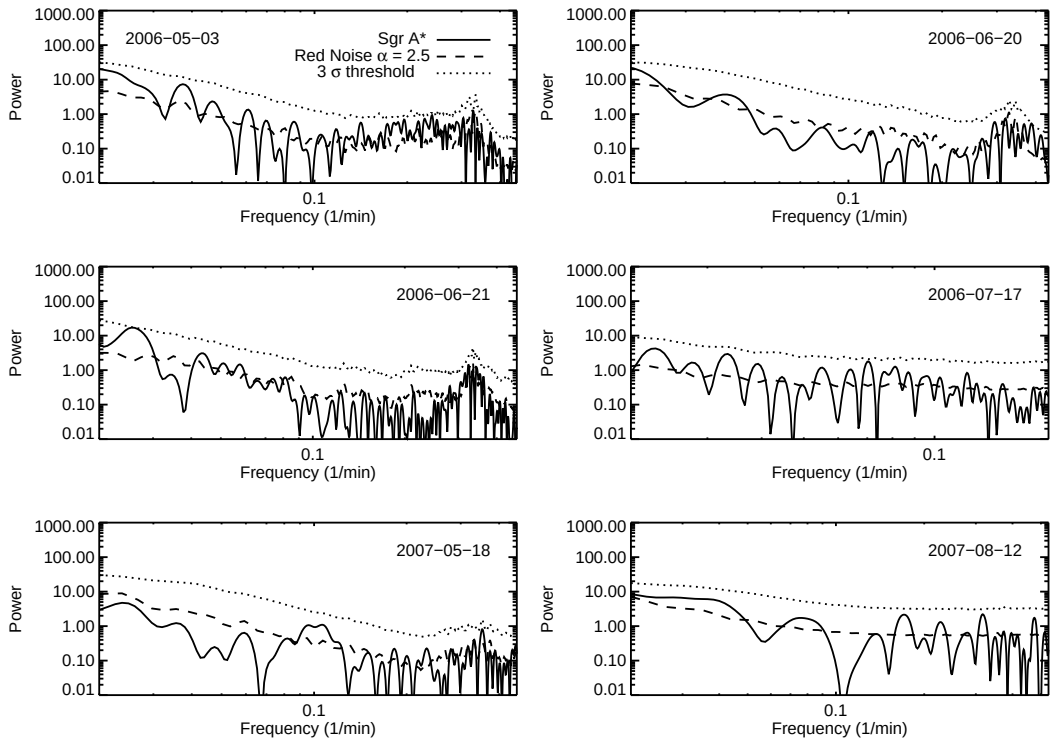

Figure 2.8 Normalized Lomb-Scargle periodograms of the Sgr A* light curves (black) at K'. Also plotted is the 3 σ significance threshold determined from Monte Carlo simulations of red noise with a power law index, $\alpha = 2.5$ (dotted line). The average of 10^5 periodograms with $\alpha = 2.5$ at the same time sampling is also shown for comparison (dashed line).

for the simulations in this work to provide a baseline for comparison. More light curves will be necessary to determine a reliable intrinsic PSD of Sgr A* (if it does not vary between nights). Where appropriate, we have also run simulations with a range of α values to investigate its effects on the statistical significance.

Although there is no evidence for QPO activity in the combined periodogram, we also test the case of a transient QPO phenomenon in each night. We therefore used our best fit of $\alpha = 2.5$ for the power law of the combined periodogram to test each night for statistically significant deviations from a purely red noise model. Our criterion for a statistically significant peak in the periodogram is

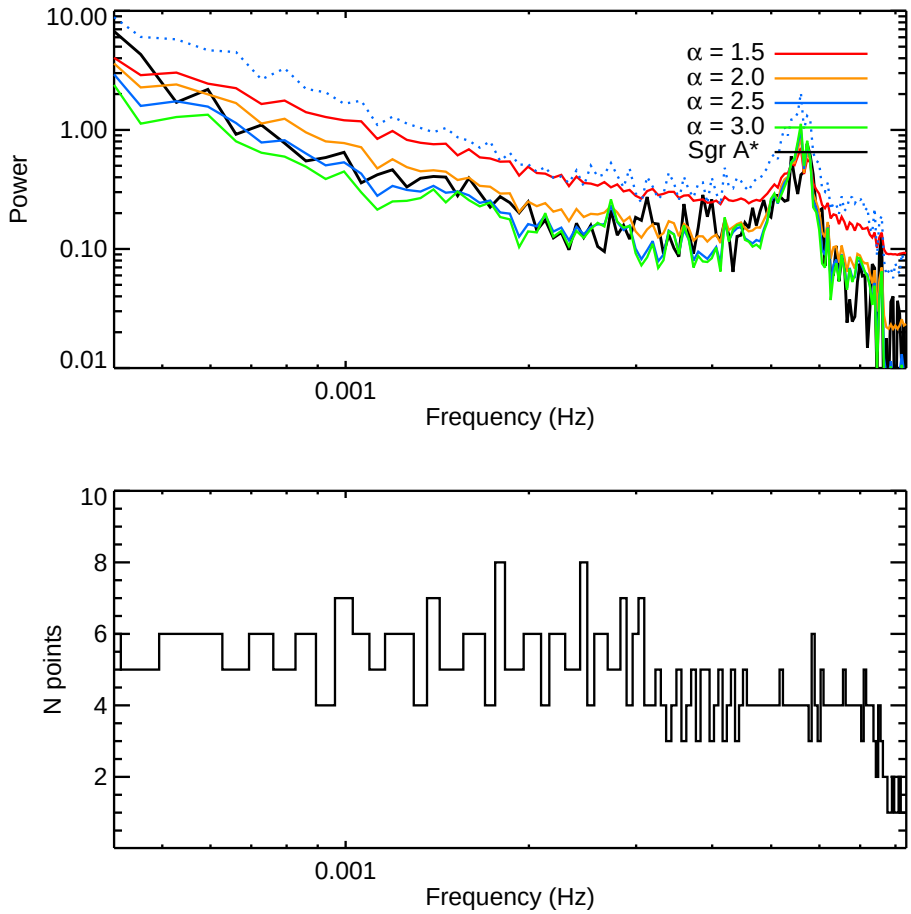

Figure 2.9 **Top**: averaged periodogram from 5 nights of K' observations (black line) with durations greater than 80 min (resulting in the exclusion of 2007 Aug 12). Colored lines are the average of 10^4 Monte Carlo simulations of combining data sets with the same sampling, for three different red noise power laws. The dotted blue line corresponds to the 3 σ threshold of power for red noise with $\alpha = 2.5$. The large spike at 0.0056 Hz (3 min) is an artifact resulting from the regular dithers in the observations. **Bottom**: plot of the number of points contributing to the averaged periodogram at each frequency.

that its power must be above the 99.7% (3σ) confidence interval from a Monte Carlo simulation with 10^5 realizations of red noise light curves. This method of establishing the significance of peaks in the periodogram is similar to the one proposed by Vaughan (2005) for evenly sampled data, but modified here to account for our unevenly sampled data set by using the Lomb-Scargle periodogram instead of the Fourier transform. The resulting periodograms are shown in Figure 2.8. The individual periodograms show peaks at low frequencies, but these appear to be consistent with red noise, with no peaks having power greater than the 3σ threshold derived from the Monte Carlo simulations. No significant peaks were found when we repeated the same procedure for PSD power law indices between 1.0 and 3.0.

The periodograms of the comparison sources are much flatter than that of Sgr A*, as expected for white noise sources. However, there is some power at very low frequencies ($<$ 40 min), which may be the result of some small time correlated systematic in the observation such as variations in seeing or AO performance over a night. Light curves and periodograms from 2006-06-21 of the three comparison sources S0-17, S0-38, and S2-133 are shown in figure 2.10. The periodograms of these sources from the other nights of observations are also comparably flat.

By adding an artificial sinusoidal periodic signal to the red noise simulations, we can address our sensitivity for detecting QPOs in the presence of red noise. In order to test this, a periodic sinusoidal signal was added to a simulated light curve with a red noise PSD slope of 2.5, with an amplitude that is a fraction of the maximum signal in the underlying red noise light curve. This fractional amplitude of the periodic signal was increased until the periodogram showed a peak at that frequency above the previously determined 3σ threshold over 98% of the time. For example, for the time sampling and duration corresponding to

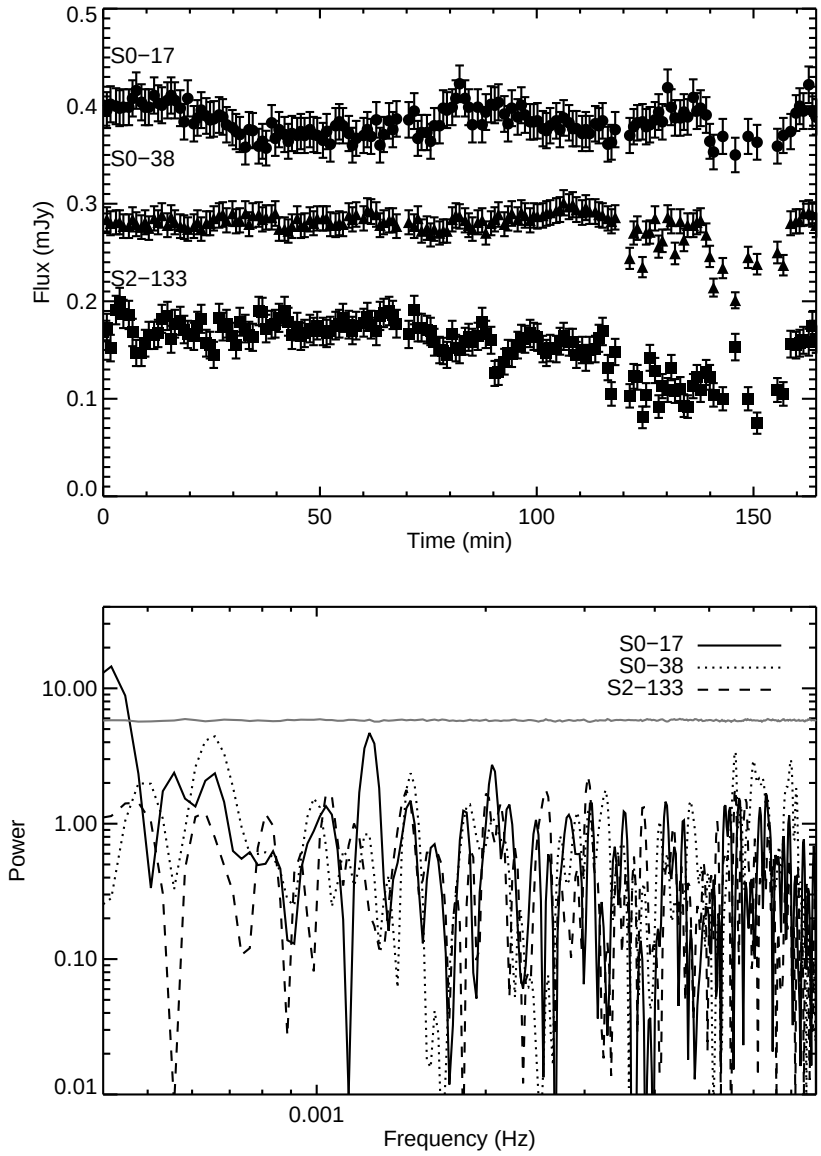

Figure 2.10 **Top**: Light curves of the stellar comparison sources from 2006-06-21. The light curve of S0-38 is offset by 0.18 mJy for clarity. **Bottom:** The corresponding periodograms of the comparison sources. In solid gray is the 3 σ threshold for white noise ($\alpha = 0$).

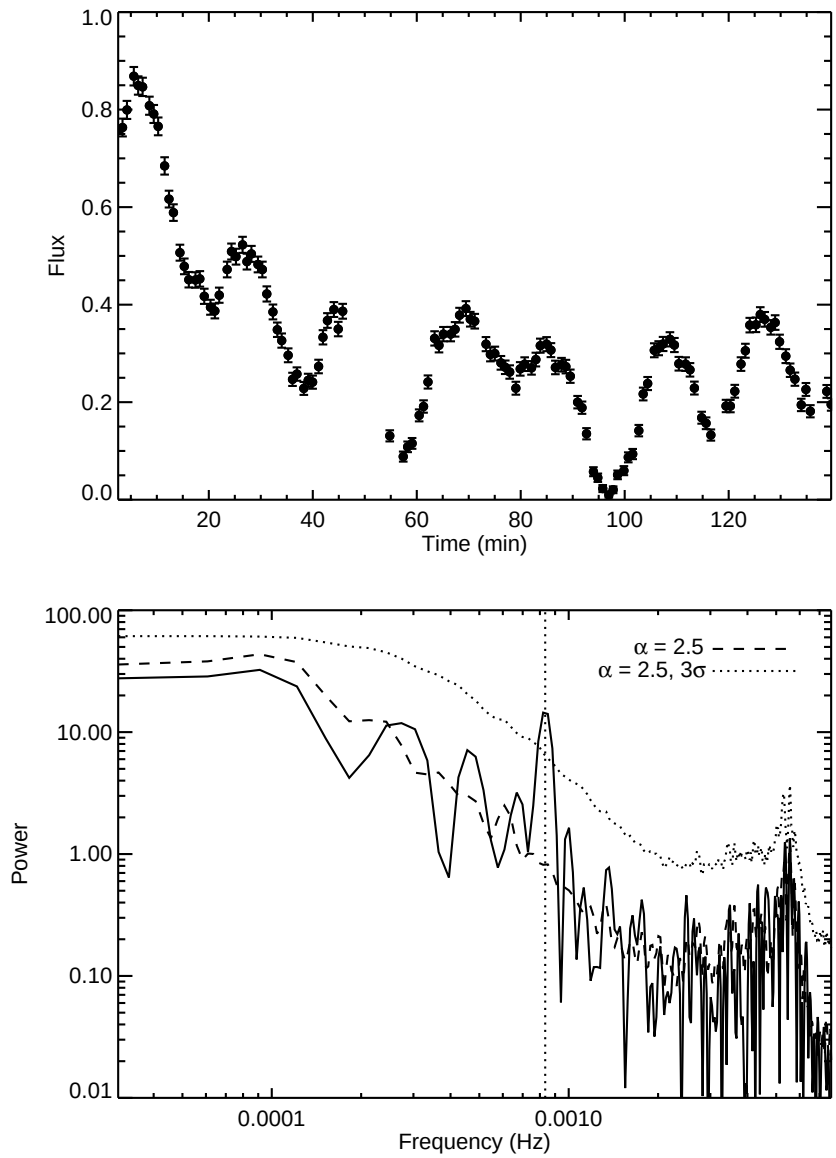

Figure 2.11 **Top:** Simulated light curve with the same time sampling as 2006 May 03 with a 20 minute periodic signal with an amplitude 15% of the maximum flux seen that night. Error bars in the light curve are based upon the noise properties of that night. **Bottom:** The corresponding periodogram of the simulated light curve (solid line) along with the average (dashed) and 3σ threshold of red noise power from the Monte Carlo simulations (dotted line). We can recover the signal at 20 min (vertical dotted line) at above our established confidence threshold.

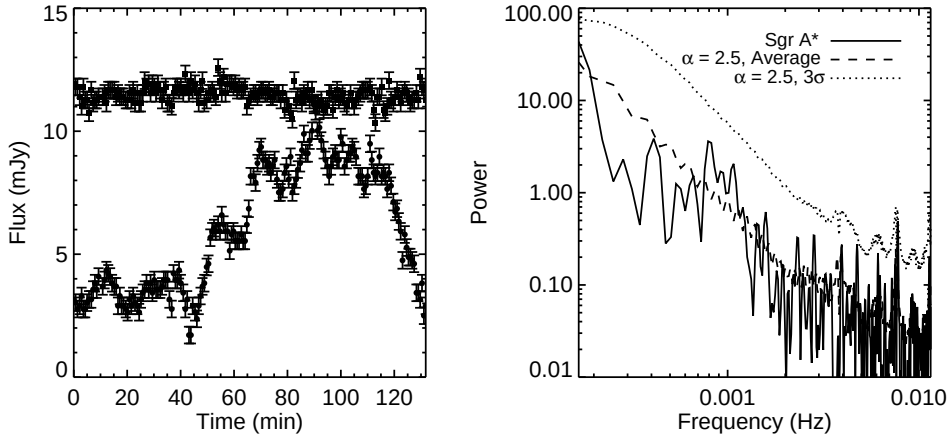

Figure 2.12 **Left:** The de-reddened light curve of Sgr A*, from 2003 June 16, as extracted by Meyer et al. (2006) (filled circles) along with a comparison source, called S1 in that paper (squares, offset by 6 mJy for clarity). **Right:** The periodogram of the Sgr A* light curve (solid) with the mean power (dashed) and 3σ thresholds set by Monte Carlo simulations of red noise with a power law slope of $\alpha = 2.5$ (dotted).

the observations on 2006 May 3, we find that we are able to detect a 20 min periodic signal with an amplitude that is at least 20% of the maximum flux density (Figure 2.11). The sensitivity for the detection of a QPO increases with frequency because the underlying red noise component has less power at higher frequencies (e.g. a 10 (40)-minute QPO signal will result in power greater than expected from red noise when its amplitude is 5% (30%) of the maximum flux density). Our sensitivity for the detection of a periodic signal is similar for the other observed light curves with similar durations (> 2 hours).

We note that attempting to remove the broad, 40-100 minute emission peaks with a low-order functional fit to increase sensitivity to periodic signals will introduce a statistical bias, because that will only remove some combination of low frequency power without actually removing the entire red noise component. Because the light curves are consistent with a red noise process at all time scales,

including the longer broad maxima, any statistical analysis must be performed without first modifying the light curves. For example, the light curve reported by Genzel et al. (2003a), the first used to argue for the possible presence of a periodic variation, shows no significant periodicity when subjected to the red noise analysis described here. Figure 2.12 shows the analysis of this night using the light curve re-extracted by Meyer et al. (2006). A significant signal was found when a low order polynomial fit to the light curve was removed in Meyer et al. (2006). However, this significance may be biased by the removal of a number of low frequency components from the light curve.

2.2.2.2 Structure Function

The first order structure function is often used to determine the time scale and the intrinsic variability in AGN light curves (e.g., Simonetti et al., 1985; Hughes et al., 1992; Paltani, 1999). Here, we use the structure function to determine the PSD slope for each night because it is more straightforward to calculate errors in the structure function. For a set of measurements, $s(t)$ at times t, the first order structure function $V(\tau)$ is defined as:

$$V(\tau) \equiv < [s(t+\tau) - s(t)]^2 > \tag{2.3}$$

Because this data set is unevenly sampled, we determined the structure function by calculating $[s(t+\tau) - s(t)]^2$ for all possible pairs of time lags and place them into bins with widths of one fourth of the lag times. Variable bin sizes were chosen in order to more evenly distribute the number of points in each bin, since there are many more samples at small lags than at large lags. The median lag time in each bin is assigned to be the lag time for that bin, while the average of the $V(\tau)$ values in each bin is used as the value of the structure function at that

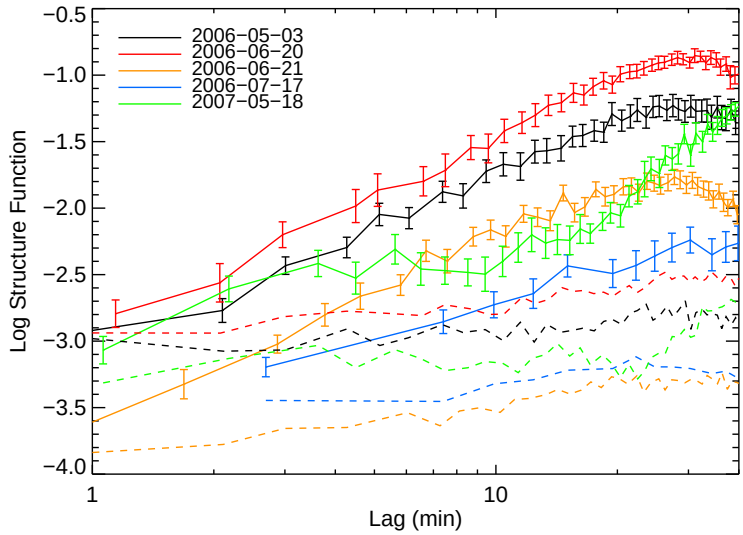

Figure 2.13 The structure functions for five of the K' nights for Sgr A* (solid) and the comparison source, S0-17 (dashed). Error bars are calculated from $\sigma/\sqrt{N}$, where σ is the standard deviation and N the number of points in the bin. Error bars for S0-17 are of comparable sizes, but are omitted for clarity.

lag. The error associated with each bin is $\sigma_{bin}/\sqrt{N_{bin}}$, where σ_{bin} is the standard deviation of the $V(\tau)$ values in the bin and N_{bin} is the number of points. We do not consider lags with fewer than 5 points in that bin. The resulting structure functions are presented in Figure 2.13.

Structure functions typically show a power law portion and two plateaus - one at the time scale of the noise and one plateau at lags longer than the variability time scale of the underlying physical process. The power law portion of the structure function is a measurement of the variability of the process. If the underlying process is stationary, then the logarithmic slope, β (where $V(\tau) \propto \tau^{\beta}$), of this region can be related to the power index, α of the PSD ($P \propto f^{-\alpha}$). Because the light curves in this study have finite sampling and duration, this relationship must be determined separately for each night. To convert the measured structure function slope into the PSD slope, we measured the slope of an average of 10^3

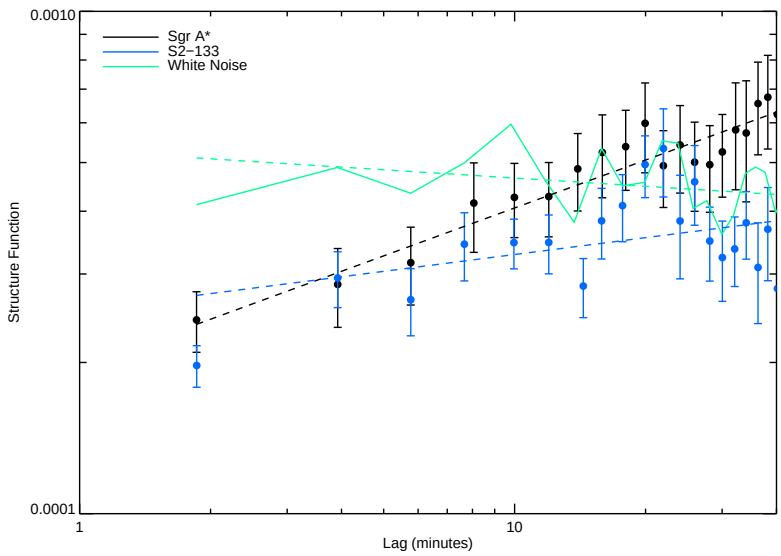

Figure 2.14 The K' structure function of Sgr A* (black), S2-133 (blue), and simulations of white noise (green) for 2007 August 12..

structure functions (β) from simulated light curves for a number of PSD slope values (α). The relationship between the measured structure function slope and the PSD slope is linear for values of α between 1.0 and 3.5 (Figure 2.16). These linear fits are used below to convert between the two slopes. We will use the structure function to compute the PSD because it is more straightforward than fitting the periodogram, given the limitations of the time sampling.

The structure function for Sgr A* shows a power law portion at periods greater than about 1 minute and a flattening at periods greater than about 40 minutes. This flattening is probably not a sign of a turnover in the intrinsic variability time scale, but is rather from the poor sampling at longer periods, as shown by large variations in the value of the structure function from Monte Carlo simulations of red noise using the same time sampling. This suggests that Sgr A* is likely to be variable at all the time scales probed in this study. Fits were made to the power law region of the structure function, typically up to about half or one-third of

the total time of observations for each night, and are summarized in Table 2.2. The best fit power law index for the nights of 2006 May 3 and 2006 June 20, and 21 has $\beta = 1.4 \pm 0.1$ ($\alpha = 2.7 \pm 0.1$), between 1 to 20 minutes, consistent with the fit of $\alpha \approx 2.5$ for the slope of the combined periodogram. The other three nights have slopes ranging from $\beta \approx 0.8$ to $\beta \approx 0.3$. The night with the flattest slope (2007 August 12) is also the night where the emission from Sgr A* was faint for the duration of the observation. Figure 2.14 shows that though the slope, $\beta = 0.26 \pm 0.04$, is flatter than on other nights, it is significantly steeper than that of S0-17 ($\beta = 0.04 \pm 0.04$), S2-133 ($\beta = 0.11 \pm 0.05$), and simulations of white noise ($\beta = -0.01$), which shows that the emission is not from a constant background source. The differences in slope between different nights may be attributable to the increase in photon noise at these faint fluxes (see Section 2.3). For all nights, the S0-17 structure function is also flat, with a slight rise at longer time scales (also from poor sampling). The structure function of Sgr A* for the L' night on 2005 July 28 has a best fit slope $\beta = 0.77 \pm 0.18$, corresponding to $\alpha = 1.84 \pm 0.27$, which is within the range of observed K' power law slopes (Figure 2.15).

2.2.2.3 Auto-correlation

To compare the Sgr A* variability between each night, we computed the auto-correlation function for each observation. The auto-correlation is defined as:

$$AC(\tau) \equiv < [s(t+\tau)s(t)] > \tag{2.4}$$

where $s(t)$ is the measured flux at time, t, and τ is the time lag. Because the light curves are unevenly sampled, we computed the auto-correlation at all possible lags and then placed the pairs in bins, similar to our method for the computing

Table 2.2. PSD fits from the structure function

Date (UT)	Fit Range (min)	β^{a}	α^{b}
2006 May 03	1-20	1.37 ± 0.09	2.74 ± 0.13
2006 June 20	1-20	1.40 ± 0.08	2.79 ± 0.12
2006 June 21	1-15	1.42 ± 0.18	2.79 ± 0.27
2006 July 17	1-40	0.71 ± 0.09	1.80 ± 0.16
2007 May 18	1-20	0.79 ± 0.11	1.95 ± 0.20
2007 August 12	1-30	0.26 ± 0.04	1.06 ± 0.08

[a]Slope of the power law portion of the structure function, $V(\tau) \propto \tau^{\beta}$

[b]Slope of the PSD, $P(f) \propto f^{-\alpha}$

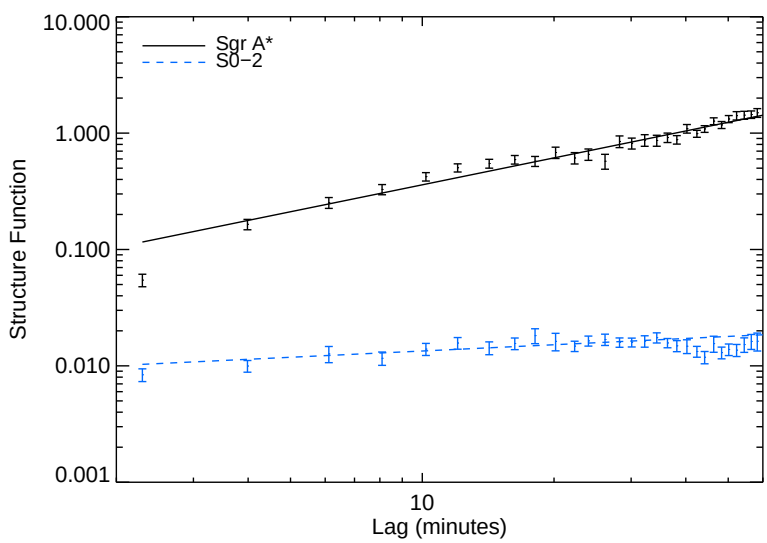

Figure 2.15 The structure function of Sgr A* (black), S0-2 (blue) at L' on 2005 July 28. The best fit power law between 3 to 40 min is also plotted. The best fit power law for Sgr A* is $\beta = 0.77 \pm 0.18$, corresponding to $\alpha = 1.84 \pm 0.27$ (see Section 2.2.2.2 for details).

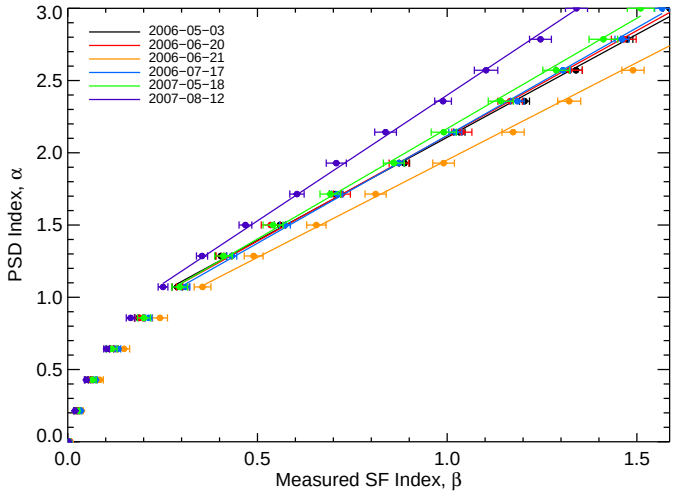

Figure 2.16 The relationship between intrinsic PSD power index and the measured power law of the structure function as simulated for the time sampling on each night. The line fits are made for PSD power law slope $\alpha > 1.0$ in the linear region of the relationship between the intrinsic PSD power law and the structure function power law.

of the structure function. We find that the correlation coefficients at time scales up to 40 minutes are consistent across all nights. At time lags greater than 40 minutes, the auto-correlations appear to diverge from each other. This is mostly likely from poor sampling at those frequencies. From Monte Carlo simulations of red noise with the same time sampling as the data set, we find that the lags greater than about 40 minutes have large variations in auto-correlations coefficients; we therefore defer interpretations of lags greater than 40 minutes until more data is available to better sample these time scales.

2.3 Discussion

Our analysis shows that the Sgr A* near-infrared light curves observed in this study are entirely consistent with red noise with no significance evidence for a

QPO signal near 20 min (or any other time scale). In addition, power is seen at the shortest time scales measured in the periodogram (2 min), well below the orbital period at the last stable circular orbit of a spinning black hole ($\sim$ 5–30 min). This indicates that the high frequency variability is not simply from Keplerian motion of a single orbiting 'hot spot' producing the near-IR flux modulations (Meyer et al., 2006; Trippe et al., 2007). The high frequency variability must originate from small areas of the accretion flow. In addition to power at high frequencies, the light curve for 2007 May 18 shows a strong spike in flux at about 10 min with a duration of $\sim$ 5 min, and a rise time of only $\sim$ 3 min, which also suggests that regions of the accretion flow responsible for the variability can be as small as 0.4 AU.

It is important to note that the significance threshold used in this study tests whether the periodogram power of peaks exceeds 3σ *at a given frequency.* It does not take into account that we are scanning over a large range of frequencies. If one searches enough frequencies, a peak of arbitrary power will appear at a random frequency. If a peak in the periodogram was found in this study that may indicate a periodic signal, then additional simulations should be performed to determine its statistical significance by accounting for the range of frequencies probed. This is referred to as the false alarm probability in Horne & Baliunas (1986) and has been calculated analytically for the case of white noise. In the case of red noise, the additional simulations would also need to account for the fact that larger peaks are more likely at low frequencies (Meyer et al., 2008, 2009).

2.3.1 Comparisons with X-ray variability

The timing analysis of Sgr A* in the infrared may be a way to compare the signatures of physical processes operating in the accretion flow of Sgr A* to

those of AGNs. Because AGN variability studies are usually performed on X-ray observations, the ideal comparison of the variability of Sgr A* to that of AGNs should be done at X-ray energies. However, X-ray emission from the inner accretion flow of Sgr A* can only be currently detected above the diffuse background during large flaring events. Simultaneous multi-wavelength studies of Sgr A* have shown that every detectable X-ray flare shows corresponding peaks in the near-IR, with no apparent time lag (Yusef-Zadeh et al., 2006; Eckart et al., 2006a). The spectral slope is also similar at X-ray and infrared wavelengths ($S_\nu \propto \nu^{-0.6}$: Bélanger et al., 2005; Yusef-Zadeh et al., 2006; Hornstein et al., 2007), which supports a model in which the X-ray photons are the result of synchrotron self Compton scattering of lower energy photons from the population of electrons that produce synchrotron emission seen in the infrared. If the infrared and the X-ray emissions are produced by the same population of electrons, then our infrared measurements can be used as a proxy for the X-ray variability; we find that the periodograms of the infrared light curves of Sgr A* are in fact consistent with having intrinsic PSD slopes similar to those reported for AGNs at X-ray wavelengths ($\alpha \approx 1 - 3$) (e.g. Lawrence & Papadakis, 1993; Kataoka et al., 2001; Markowitz et al., 2003). Our observations are consistent with Sgr A* being variable at all time scales between ~ 2 minutes to ~ 1 hour with no changes in PSD slope between these time scales during the observations period on any single night. This steeply rising power law cannot be extended to arbitrarily low frequencies because the integrated power would diverge. For example, AGNs typically show either one or two breaks in their power spectrum, with recent evidence suggesting that these breaks scale with the mass and accretion rate of the AGN (McHardy et al., 2006). The lack of a break in the Sgr A* periodogram is not unusual because the breaks seen in AGNs are at time scales on the order of days or weeks (Markowitz et al., 2003). Using the relationship between the

break frequency, the black hole mass, and accretion rate found by McHardy et al. (2006) for stellar mass black holes and AGNs, the predict break frequency for Sgr A* is $\sim 1 \times 10^6$ days. However, a direct comparison to AGNs is difficult at this time because the physical scales involved are so different; the cores of AGNs in which variability is usually measured have sizes on the order of parsecs, whereas Sgr A* is unresolved in this study at a resolution of 65 mas, or $\sim$ 540 AU. The accretion luminosities of AGNs with well measured timing properties are substantial fractions of their Eddington luminosity compared to the 10^{-9} Eddington luminosity for Sgr A*, which may make the comparison inapplicable as well. Nevertheless, the variability properties of Sgr A* are valuable additions to the broadband spectrum since any models that can produce the observed spectrum should also be able to account for the timing characteristics.

2.3.2 The effect of measurement noise on the inferred PSD slope

While it may appear from the results in Section 2.2.2.2 that the slope of the power spectrum is changing between nights, the red noise simulations show that, as the amplitude of the red noise signal decreases, photon noise will increasingly dominate the measurement of the slope, thus biasing the measurement of the true slope of the underlying red noise process. To determine when photon noise becomes important to the slope measurements, we performed Monte Carlo simulations of light curves with time sampling from 2008 August 12 and assuming an intrinsic $\alpha = 2.5$ for various values of the ratio of the standard deviation of the red noise signal to the standard deviation of the expected measurement noise ($\sigma_{red\ noise}/\sigma_{white\ noise}$). Average values of α were extracted from 200 simulated light curves at each value of $\sigma_{red\ noise}/\sigma_{white\ noise}$ from 0.1 - 100.0 (Figure 2.17). We find that as $\sigma_{red\ noise}/\sigma_{white\ noise}$ becomes smaller, the measured value of α

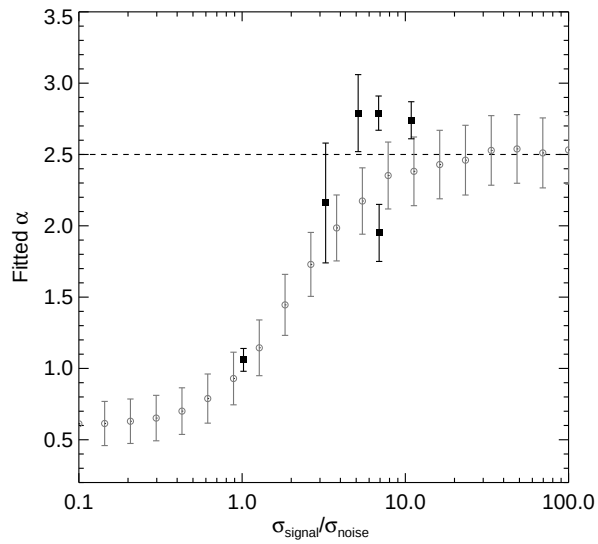

Figure 2.17 Plot of the fitted power law slope α as a function of the ratio between the standard deviation of the light curve (signal) and the photon noise expected at the mean flux density for each K' night (solid black squares). Open grey circles shows the results of MC simulations with the same time sampling as 2007 August 12, showing that as the red noise signal becomes comparable to the measurement noise, the measured slope of the power spectrum becomes flatter than the intrinsic value of $\alpha = 2.5$ used in the simulation.

becomes flatter. The simulation showed that a measurement of $\alpha = 1.0$ can arise even from a red noise process with $\alpha = 2.5$ if $\sigma_{red\ noise}/\sigma_{white\ noise} = 1.1$. We find that the measured value of α will asymptote to 2.5 when $\sigma_{red\ noise}/\sigma_{white\ noise} >$ 7.9. This result suggests that the measurement of $\alpha = 1.06 \pm 0.08$ for 2007 August 12 can be explained as having the same intrinsic PSD slope, α, as the other nights, but made flatter by a more prevalent white noise component. Note that this is an effect of a white noise source on top of a red noise signal, which can be caused simply by the measurement noise at faint flux densities or the presence of an unresolved stellar source. Figure 2.17 shows the relationship between the measured value of α and the ratio of standard deviation of the observed light curves to the expected noise level for the corresponding mean flux density ($\sigma_{signal}/\sigma_{noise}$) for

all K' nights. The measured value of α appears to asymptote on nights when the red noise amplitude is stronger. This relationship is consistent with that found in the Monte Carlo simulations, where the nights with lower values of $\sigma_{signal}/\sigma_{noise}$ have flatter red noise spectra than those on the nights with greater fractional signal variance. These results show that the differences between the measured slopes for different nights may be explained by the effect of measurement noise on light curves with faint fluxes.

We also considered how a slightly time correlated source would affect the power law slope measurements by including a time correlated source with a small α into the simulations and varying its signal strength as the above treatment with white noise. This is motivated by the fact that there is a slight slope to the structure function of our comparison source S2-133. For example on 12 August 2007, S2-133 has a structure function power law slope of $\beta = 0.11 \pm 0.05$ corresponding to $\alpha = 0.7 \pm 0.2$. We find that the addition of such a background source increases the measured Sgr A* PSD power law slope α by a maximum of 0.1, which is about the same level as our fitting error. The effect of a slightly time correlated background source thus appears to be a source of systematic error, but one which does not significantly affect our results.

2.3.3 Limits on a quiescent state of Sgr A*

A notable feature of the light curves in these observations is that there appears to be a lower limit, or 'floor' to the light curves from each night. This lower limit is not an observational constraint, because we are able to reliably detect stars within $0''.5$ of Sgr A* to K$' \approx 19$ mag compared to the faintest Sgr A* observation at $K' \approx 17$ mag. A question to be investigated in future studies is whether this represents a 'quiescent' state of Sgr A*, characterized by lower

variability at that flux level or is a faint star confused with Sgr A*. If the low flux density state is a physically distinct state, then the large flux variations would be the result of additional emission of energy above this quasi-steady state. To examine the nature of this faint state, we can look to the peak of the distribution of flux densities fainter than ~ 0.3 mJy for each night. We find that the flux density of the peak of this distribution shifts slightly between different nights of observations. However, this shift appears only to be marginally significant given the lower photometric accuracy at the fainter flux levels. Before physical models can be applied to the faint state, a more detailed analysis of the light curves is necessary to establish whether this state exists. If the faint state of Sgr A* can be modeled as arising from the steady accretion of mass, then the slight drift of this mean flux level may be explained by a gradual change in the accretion rate. Another explanation for the drift in the mean Sgr A* flux density is that it is due to very long timescale flux variation from the red noise power law behavior of the flux as in AGNs.

It is clear that Sgr A* can now always be detected in the infrared using LGS AO and that even at low flux densities, the $K' - L'$ color of the source appears to be redder and have PSD slopes steeper than a star, but the measurement errors do not rule out the possibility of a faint stellar component in the near-infrared flux from the location of Sgr A*. More observations during both the faint and bright states of Sgr A* are necessary to confirm whether there truly exists a quiescent state with different timing behavior. Since Sgr A* is much redder than any stellar source, observations at L' would be much less affected by stellar contamination than at K', thus the test for a quiescent state may be more conclusive at L'. Note that the existence of a quiescent state does not affect the timing analysis for periodic signals because the mean flux density is subtracted from a light curve to remove the zero frequency power before creating the periodogram.

While no QPO signal was detected in this study, this does not preclude the possibility for a transient periodic signal in other observations. In addition, a periodic signal with an amplitude below our detection threshold would also be difficult to detect unless the signal is consistently at the same frequency such that it would become statistically significant in a combined periodogram. More observations of Sgr A* would be helpful to investigate such low amplitude QPO signals.

2.4 Conclusion

We have obtained 7 near-infrared light curves of Sgr A* using NGS and LGS AO and through Monte Carlo simulations, test for a periodic signal in the presence of red noise with unevenly sampled data. We find no statistically significant QPO signals in any of the Sgr A* light curves observed in this study; the variability appears to be consistent with a physical process having a power spectrum index $\alpha \sim 2.5$ in the averaged periodogram, with variations between $\alpha = 1.0$ to 2.8 between different nights. A determination of the true PSD power law slope of Sgr A* will require at least double the number of light curves observed in this study so that more sophisticated spectral estimation techniques can be used (e.g. Priestley, 1981; Papadakis & Lawrence, 1993). While more data will be necessary to reliably determine the intrinsic PSD slope, it is unnecessary to invoke a periodic signal to describe the variability of the light curves observed in this study. We have also shown the importance of preforming statistical tests for QPO signals using the entire Sgr A* light curve. Removing broad large amplitude peaks eliminates some combination of low frequency power, artificially boosting the significance of mid-range frequencies without actually removing the underlying red noise component.

The mechanism producing the infrared variability in Sgr A* in these observations may be related to the processes occurring in AGNs or accreting black hole binaries, based on the similarity of their timing properties. Detailed model comparison between Sgr A* and other accreting black hole systems will require continuous observations over longer time scales and at faster time sampling to detect possible low and high frequency breaks, respectively, in the power spectrum.

CHAPTER 3

High angular resolution integral-field spectroscopy of the Galaxy's nuclear cluster: a missing stellar cusp?

3.1 Introduction

Over 30 years ago, theoretical work suggested that the steady state distribution of stars may be significantly different for clusters with a massive black hole at the center than those without (e.g. Bahcall & Wolf, 1976; Cohn & Kulsrud, 1978; Young, 1980). Stars with orbits that bring them within the tidal radius of the black hole are destroyed and their energy is transferred to the stellar cluster. In the steady state, this energy input must be balanced by the contraction of the cluster core, which appears as a steeply rising radial profile in the number density of stars toward the cluster center. This radial profile is usually characterized by a power law of the form $n(r) \propto r^{-\gamma}$, with a power law slope, γ, that is steeper than that of a flat isothermal core. For a single-mass stellar cluster, Bahcall & Wolf (1976) determined the dynamically relaxed cusp will have $\gamma = 7/4$. The presence of such a steep core profile, or cusp, is important observationally because it may represent a simple test for black holes in stellar systems where dynamical mass estimates are difficult, such as in the cores of galaxies. The stellar cusp is also important theoretically as it is a probable source of fuel for the growth

of supermassive black holes and its presence is often assumed in simulations of stellar clusters having a central black hole (e.g., Merritt, 2005, and references therein).

Theoretical work has progressed from the early simulations by Bahcall & Wolf (1976) to include many complicating effects, including multiple masses, mass segregation, and stellar collisions, on the density profile of stellar clusters in the presence of a supermassive black hole (e.g., Bahcall & Wolf, 1977; Murphy et al., 1991; Alexander & Hopman, 2008). These theories predict cusp slopes within a black hole's gravitational sphere of influence ranging from $7/4 \geq \gamma \geq 7/3$ for a multiple mass population to as shallow as $\gamma = 1/2$ for a collisionally dominated cluster core. An important assumption of all cusp formation models is that the stellar cluster be dynamically relaxed. Without this assumption, the stellar distribution would show traces of the cluster origin in addition to the influence of the black hole.

The Galactic center is an ideal place to test these theories of cusp formation as it contains the nearest example of a supermassive black hole (Sgr A*, with a mass $M_\bullet = 4.1 \pm 0.6 \times 10^6$ $M_\odot$, Ghez et al., 2008; Gillessen et al., 2009). Located at a distance of only 8 kpc, the radius of the sphere of influence of the Galactic center black hole ($\sim$ 1 pc) has an angular scale of $\sim 25''$ in the plane of the sky, two orders of magnitude larger than any other supermassive black hole. In order to plausibly test stellar cusp formation theories, the stellar population used to trace the cusp profile must be older than the relaxation time, which is of order 1 Gyr within the sphere of influence of Sgr A* (e.g., Hopman & Alexander, 2006). In the Galactic center, late-type red giants (K to M) are the most promising tracers of the stellar distribution since they are $>$ 1 Gyr old, bright in the NIR, and abundant. On parsec size scales, these stars dominate the flux, so early seeing

limited observations of the surface brightness profile in the NIR at the Galactic center were successfully used to show that the structure of the nuclear star cluster at large scales has a density power law of $\gamma \approx 2$ (Becklin & Neugebauer, 1968). Integrated light spectroscopy of the CO absorption band-head at 2.4 μm (which is dominated by red giants) also confirmed this slope down to within ~ 0.5 pc from the black hole (McGinn et al., 1989; Haller et al., 1996). These measurements, as well as integrated light spectroscopy from Figer et al. (2000) of the inner $0''.3$, found a lack of CO absorption in the inner $\sim$ 0.5 pc of the Galaxy. It was unclear at the time whether this represented a change in the stellar population with fewer late-type stars in the inner region or a change in the stellar density profile. Because the integrated light spectrum is biased toward the brightest stars, contamination from a few young Wolf-Rayet (WR) stars (age $<$ 6 Myr), such as the IRS 16 sources identified in the early 1990s located between 1–2$''$ from the black hole (e.g., Allen et al., 1990; Krabbe et al., 1991), can significantly impact measurements of the underlying stellar density.

Several approaches have been taken to identify the cause of the difference in the CO equivalent width in the integrated light within the inner 0.5 pc of the Galaxy. Scoville et al. (2003) attempted to remove the effects of the bright young stars on the surface brightness distribution through narrow band imaging with NICMOS/HST. They found a surface brightness that began to flatten and drop slightly in the central 0.1 pc. Since fainter young stars can still contribute to the surface brightness, Genzel et al. (2003b) used adaptive optics (AO) imaging with H (1.6 μm) and K_s (2 μm) filters to measure the stellar density using number counts, which they argue more robustly traced the population of red giants. They find $\gamma = 2.0 \pm 0.1$ at $R \geq 10''$ and $\gamma = 1.4 \pm 0.1$ at $R < 10''$, which suggests that there may be a stellar cusp at the Galactic center within the range predicted by Bahcall & Wolf (1977). Further work by Schödel et al.

(2007), which included deeper AO imaging, produced a fit of a broken power law to the observed projected surface number density profile of the form $\Sigma(R) \propto R^{-\Gamma}$, where R is the projected distance from Sgr A* in the plane of the sky, and Γ the projected power law slope. Their best fit broken power law model has a break radius at $R_{break} = 6''.0 \pm 1''.0$ (0.22 pc), with $\Gamma = 0.75 \pm 0.1$ outside R_{break} and $\Gamma = 0.19 \pm 0.05$ as the slope of the stellar cusp inside R_{break}. This indicated that the cusp slope is perhaps flatter than the range predicted by Bahcall & Wolf (1977). However, with only number counts, it was still unclear how much bias to the slope was contributed by the dynamically unrelaxed young stellar population, which represents a large fraction of the bright stars ($K' < 14$) that have been spectroscopically identified in the inner $1''$ (e.g., Ghez et al., 2003; Paumard et al., 2006).

To make further progress, it is necessary to discriminate between the early and late-type stars. One recent approach has been through narrow-band imaging to target wavelengths where there are measurable differences between spectral features of the two types of stars. For example, the CO bandhead absorption features starting at 2.29 μm are very strong for late-type stars (K & M), and absent for early-type stars (O & early B). Using the CO narrowband images from the Gemini North Galactic Center Demonstration Science Data Set, Genzel et al. (2003b) found that the fraction of late-type stars declines between $10''$ and $1''$ from the Galactic center, and thus, may be flatter than expected from number counts. However, this narrowband dataset was shallower than that of the broadband images used in the number counts measurements and had trouble differentiating between the two types of stars at $K > 13$. More recently, Buchholz et al. (2009) took deeper narrowband images ($K < 15.5$) in CO and found an even more shallow slope in the inner region of the cluster. Their best fit slope of $\Gamma = -0.17 \pm 0.09$ at $R < 6''.0$ suggests that the late-type stars may even be slightly

declining toward the cluster center. While number counting with narrowband images has greater discriminating power than broadband images, this method has limitations. First, this method is strongly dependent on how well the dataset can be calibrated based upon existing spectroscopically determined samples, which is limited to K< 13. In addition, limits on the CO equivalent widths depend on how precisely the slope of the stellar continuum can be measured with narrow band filters.

A spectroscopically selected sample would be ideal to separate the late-type, presumably dynamically relaxed population from that of the young early-type stars. Until recently, much of the spectroscopy taken of stars in the Galactic center has been seeing-limited and limited in sensitivity to $K < 13$ (see Genzel et al., 2000; Blum et al., 2003; Figer et al., 2003). These surveys found a drop in the fraction of late-type stars toward the central $\sim 10''$, but because they were sensitive only to the brightest giants, the uncertainty remained as to whether the fainter stars would show the same trend. Nevertheless, these results combined with measurements from imaging all point toward fewer stars in the central 0.5 pc than would be expected for a relaxed cusp.

By combining the advantages of high spatial resolution from AO imaging with the discriminating power of spectroscopy, the advent of integral-field spectroscopy (IFU) behind AO has potential to provide the most sensitive method of measuring the stellar cusp profile in the inner 0.5 pc of the Galaxy. Measurements with the SINFONI IFU at the VLT have shown that it is possible to identify young stars at better than 100 mas angular resolution (Paumard et al., 2006; Gillessen et al., 2009). Here, we report on a high angular resolution spectroscopic survey of the central 0.15 parsec of the Galaxy using laser guide star adaptive optics with the OSIRIS IFU at the Keck II telescope. The survey reaches a completeness of 40%

at $K' \approx 15.5$, two magnitudes fainter than previously reported spectroscopic surveys of late-type stars in this region. The observations and data reduction method are described in Section 3.2 and 3.3. Using these observations, it is possible to separate the presumably dynamically relaxed late-type population from the young, unrelaxed population (Section 3.4). We find that the surface number density of late-type stars is significantly flatter than the range of power laws predicted by Bahcall & Wolf (1977) (Section 3.5). This measurement rules out all values of $\gamma > 1.0$ at a confidence level of 99.7%. In Section 3.6, we discuss possible dynamical effects that may lead to the flat observed slope and implications for future measurements of the stellar cusp at the Galactic center.

3.2 Observations

Near-IR spectra of the central $4''$ of the Galaxy were obtained between 2006 and 2009 using the OSIRIS integral field spectrograph (Larkin et al., 2006) in conjunction with the laser guide star adaptive optics (LGS AO) system on the Keck II telescope (Wizinowich et al., 2006; van Dam et al., 2006). The laser guide star was propagated at the center of our field and for low-order tip-tilt corrections, we used the $R = 13.7$ mag star, USNO 0600-28577051, which is located $\sim 19''$ from Sgr A*. The AO system enabled us to obtain nearly diffraction limited spatial resolution ($\sim$ 70 mas) in our long-exposure (15 min) 2 μm data sets. All observations were taken with the narrow band filter Kn3 (2.121 to 2.229 μm) centered on the Br γ hydrogen line at 2.1661 μm, with a pixel scale of 35 mas and a spectral resolution of $\sim$ 3000. With this filter, OSIRIS has a field of view of $1.''68 \times 2.''24$ per pointing and offers sensitivity to both early and late-type stars. Early-type stars from OB supergiants to B type main sequence young stars show a prominent Br γ line, while late-type (K & M) evolved giants contain strong Na

Table 3.1. Summary of OSIRIS observations

Field Name	Field Center[a] (″)	Date (UT)	N_{frames}[b]	FHWM[c] (mas)
GC Central (C)	0, 0	2008 May 16	11	84×85
GC East (E)	2.88, -0.67	2007 July 18	10	85×70
GC South (S)	-0.69, -2.00	2007 July 19	10	73×63
GC West (W)	-2.70, 0.74	2007 July 20	11	110×86
GC Southeast (SE)	1.67, -2.23	2008 June 03	11	68×63
GC North (N)	0.33, 2.01	2008 June 07	7	102×85
		2008 June 10	5	75×70
GC Northeast (NE)	2.55, 1.27	2008 June 10	5	74×68
GC Southwest (SW)	-2.9, -1.12	2009 May 26	4	92×80
GC Northwest (NW)	-1.99, 2.42	2009 July 21	6	71×64

[a]RA and DEC offset from Sgr A* (RA offset is positive to the east).

[b]Frames have an integration time of 900 s.

[c]Average FWHM of a relatively isolated star for the night, found from a two-dimensional Gaussian fit to the source.

I lines in this wavelength range.

With the goal of covering an $\sim 8'' \times 6''$ area centered on Sgr A*, we divided this region into 9 fields (see Figure 3.1). We will refer to these pointings by their approximate orientation with respect to Sgr A* (i.e. GC Central, GC East, GC Southeast, GC South, GC West, GC North, GC Northeast, GC Southwest, and GC Northwest). We obtained between four to ten 900 sec exposures ($\sim$ 2.5 hr total exposure time) for each field. For all but the central field, the exposures were dithered in a nine position pattern that covered the center, sides and corners of a $0''.2 \times 0''.2$ square. For the field centered on Sgr A*, the dither positions were the four corners of a $1'' \times 1''$ square in an effort to keep the $1'' \times 1''$ surrounding Sgr A* within the field of view of all exposures. The survey region is oriented at

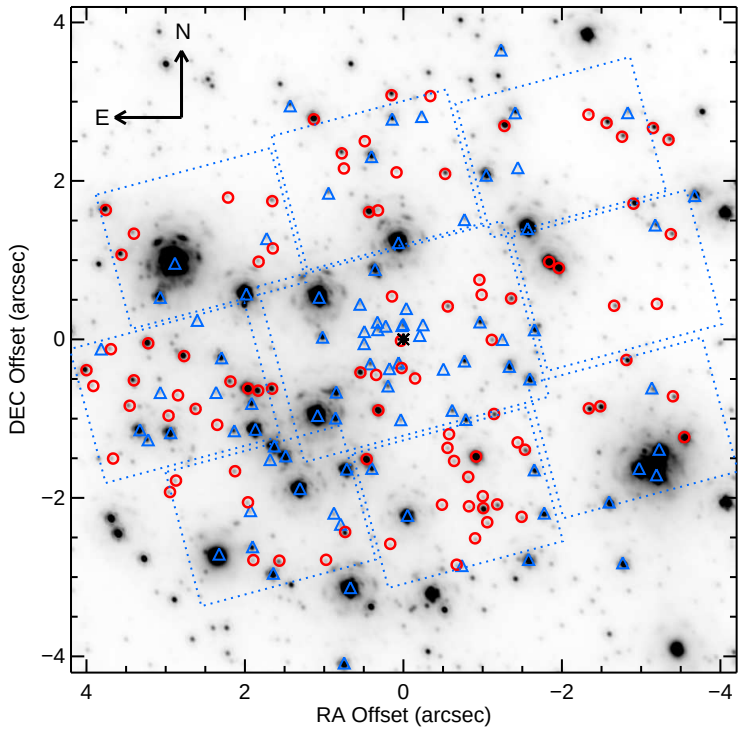

Figure 3.1 The currently surveyed region overlaid on a K′ (2.2 μm) image of the Galactic center taken in 2007. Sgr A* is marked at the center with a *. Spectroscopically identified early (blue triangles) and late-type (red circles) stars are marked. Each field is enclosed by dotted lines. Some spectral identifications are outside of the marked lines because they were found at the edge of the dithers.

a position angle (PA) of $\sim$ 105 degrees, with the longer direction oriented along major axis of the disk of young stars rotating in the clockwise direction in the plane of the sky (Paumard et al., 2006; Lu et al., 2009). Table 3.1 summarizes these observations.

3.3 Data Reduction

Data cubes with two spatial dimensions and one spectral dimension were produced using the OSIRIS data reduction pipeline provided by Keck Observatory. The pipeline performs dark current subtraction, cosmic ray removal, and wavelength rectification. The cubes were not corrected for the effects of chromatic differential atmospheric dispersion because this effect is small within the wavelength range of Kn3, shifting the centroid of stars by only 0.1 spatial pixel between the shortest and longest wavelength channel.

For each field, stellar positions were estimated by running *StarFinder*, a point spread function (PSF) fitting program (Diolaiti et al., 2000), on images made from collapsing the data cubes along the spectral dimension. First, a mosaic was made by combining the individual dithers within each field with the OSIRIS pipeline using an average for all overlapping spatial pixels. An image was then created from the mosaicked cube by taking the median of the spectral channels at each spatial pixel. Next, between 1–3 of the brightest, most isolated stars were chosen by hand as PSF reference stars for *StarFinder*. This PSF was then used to determine the centroids of all the stars in the mosaic in an initial pass. After the first attempt at identifying sources, we ran an additional iteration of *StarFinder* to improve the estimate of the PSF, which is then used in a second pass to determine centroids. The stars identified by this process were cross-checked with the nearest epoch of deep images taken at K' using LGS AO with the NIRC2 imager on Keck II (Ghez et al., 2008) in order to remove false detections in the noisier OSIRIS data and to obtain accurate broadband photometric measurements for these stars. As a final step, *StarFinder* was run on each individual cube using relative positional priors from the deeper mosaic cubes and the PSF as determined from the OSIRIS mosaic to obtain precise OSIRIS positions in preparation for

spectral extraction from the individual data cubes.

The spectrum of every star was then extracted from each cube by performing aperture photometry for the star at each spectral channel. We used an aperture of radius 2 pixels (70 mas) to extract the stellar spectrum and the median of an annulus with inner radius at 2 pixels and outer radius at 4 pixels to determine the sky background. For regions with very high stellar density, such as within the central arcsecond, the background was manually determined by the median of patches of sky free of stars as close to the target star as possible. The final spectrum of each star was then produced by averaging the spectra of that star from all data cubes from that night. When the signal to noise ratio (SNR) per spectral channel between the spectra were significantly different, they were combined using an average weighted by the SNR (calculated between 2.212 to 2.218 μm).

The combined spectra have SNRs ranging from over 100 for bright stars ($K' < 13$) to ~ 5 for the faint stars ($K' \approx 15.5$) that have marginal line detections. Photon noise appears to dominate the SNR of the final spectra and thus our ability to assign spectral types to most of the stars. In addition, regions with strong gas emission such as along the mini-spiral (Paumard et al., 2004) and within the central arcsecond can be problematic for identifying Br γ absorption lines from early-type stars. Interstellar Br γ emission can be quite strong and can have several kinematic components, which can lead to a systematic bias in the measurement of the Br γ line in the early type stars if the background gas component is not completely corrected. Confusion is also a problem around very bright sources such as the IRS 16 stars, where we were unable to extract several $K' \approx 13$ stars that were identified in NIRC2 images[1].

[1]NIRC2 is less sensitive to confusion because the plate scale is 10 mas compared to 35 mas used in the OSIRIS observations and the higher strehl ratios obtained from the much shorter

An A0V (HD 195500) and G2V (HD 193193) star were observed on each night to correct for atmospheric absorption lines[2]. The A star, having no intrinsic absorption lines other than Br γ and He I in the Kn3 filter, serves as a good indicator of atmospheric and instrumental features. To remove the Br γ and He I line from the A0V spectrum, we replace the region between 2.155 to 2.175 μm with the same region from the G2V star and divided by the empirically observed solar spectrum shifted to the radial velocity of the G2V star (similar to the procedure described in Hanson et al. (1996)). The A star spectrum was then divided by a 10,000 K blackbody to remove the stellar continuum.

3.4 Spectral Identification

Given our survey sensitivity, we expect to be able to detect the early-type stars in the form of bright Wolf-Rayet stars, OB supergiants, main sequence young stars down to B2-B4V, and late-type stars in the form of K-MIII evolved giants. The most important feature of this survey is its ability to differentiate between early and late-type stars. This distinction is apparent when comparing template spectra of early type stars with those of late type giants, even in the limited Kn3 wavelength range; the young stars have featureless spectra except for Br γ and He I at 2.1661 and 2.1641 μm, respectively, while the late-type stars lack these high temperature lines and show a plethora of other atomic and molecular lines, most prominently the Na I lines at 2.2062 and 2.2090 μm.

In order to assign spectral types to the stars, we separate all the extracted spectra by visual inspection into five groups: 1. Spectra with prominent Br γ lines and no Na I lines are identified as early-type stars (e.g., S0-2 in Figure 3.2).

exposures (30 s vs. 900 s)

[2]These stars were observed using natural guide star mode with 30 s integration time and 5 frames per star.

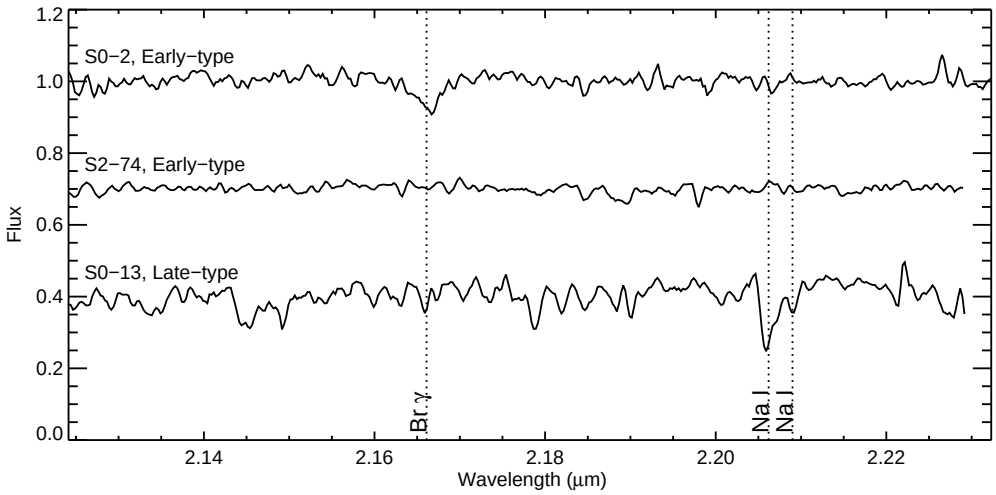

Figure 3.2 Example of observed spectra in the Kn3 narrowband wavelength region of early and late-type stars. The Br γ and Na I lines are used to differentiate between early and late-type stars, respectively. S0-2 is a $K' = 14.1$ early-type star with a strong Br γ line. S2-74 is a $K' = 13.3$ early-type star showing a featureless spectrum in the OSIRIS Kn3 filter wavelength range. S0-13 is a $K' = 13.5$ late-type star showing the Na I doublet. See Figures 2a, 2b, and 2c in Appendix **??** for the spectra of all stars with spectral identification.

2. Spectra with prominent Na I lines, but no Br γ line are identified as late-type stars (e.g., S0-13 in Figure 3.2). 3. Low SNR (< 5) spectra with no apparent lines are classified as unknown. 4. Bright stars with high SNR ($K' < 14$, SNR > 40) spectra with no late-type or Br γ lines are identified as young. These are most likely late O-type stars, which have very small or undetectable Br γ absorption lines at the resolution of this survey (Hanson et al., 1996) (e.g., S2-74 in Figure 3.2). 5. Spectra with both Br γ and Na I lines are identified as late-type if there is strong gas emission nearby, which would explain the Br γ line as an over-subtraction of the background gas (2 stars showed these features). Using these criteria in the survey region, we classified 68 stars as early-type (24 newly identified) and 86 stars as late-type (73 newly identified). The late and early-type stars are reported in Tables 3.2 and 3.3 and labeled in Figure 3.1. The stars with successfully extracted spectra, but have undetermined spectral types are listed in Table 3.4. Our ability to classify the stars is strongly dependent on the SNR of the spectra, with 100% of the stars having SNR > 40 being identified (see Figure 3.3).

Equivalent widths for the Na I lines in the spectra of the late-type stars were measured by normalizing the spectra and integrating between 2.2053 to 2.2101 μm as in Förster Schreiber (2000), after shifting the spectra to rest wavelengths. The Na I equivalent widths range from 1.2 to 4.9 Å, consistent with that of KIII to MIII evolved giants, with RMS uncertainties between 0.1 to 2 Å. There does not appear to be a significant correlation between the equivalent width and K' magnitude, suggesting that the Na I lines are not able to further differentiate between K and M spectral types at the SNR of these measurements (see Figure 3.4). The equivalent widths of the Br γ lines are measured by fitting a Gaussian to the line and integrating the model Gaussian parameters. While the equivalent widths of the Na I lines do not change with brightness, the young stars show a

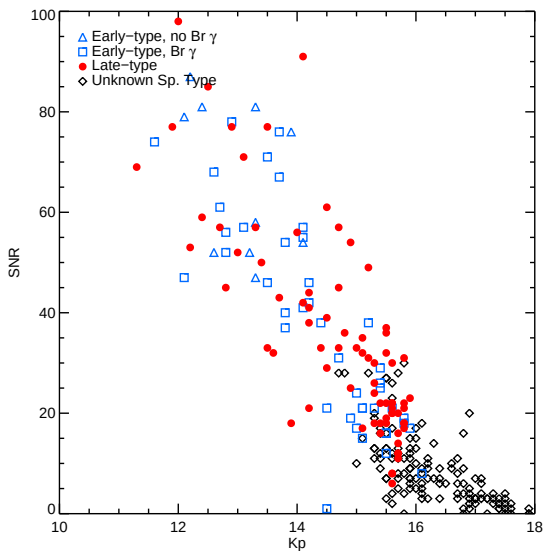

Figure 3.3 The relationship between the SNR and K' for stars observed in this study and their spectral type. The spectral types of every star with SNR > 40 was determined successfully.

significant decrease in the equivalent width of Br γ with increasing brightness as shown in Figure 3.4. These measurements support the assumption that the bright stars ($K' < 13$) with no spectral features in the Kn3 wavelength range are young stars.

This survey is complete to about $K' = 12$ and falls off to about 40% completeness at $K' = 15.5$, measured relative to the stars detected in the same region from imaging, which is complete to $K' = 16.0$ (Ghez et al., 2008). Tables 3.5, 3.6 and 3.7 summarizes the completeness in each of the observed fields both before and after extinction correction (see Section 3.5). We were able to determine spectral types for all stars with extractable spectra and $K' < 14.0$. The sample is not complete to $K' = 14.0$ because the spectra of some bright stars ($K' \approx 13$) detected in broadband images were not extractable due to confusion with the IRS 16 sources. The K' luminosity function of all the stars in the survey is shown

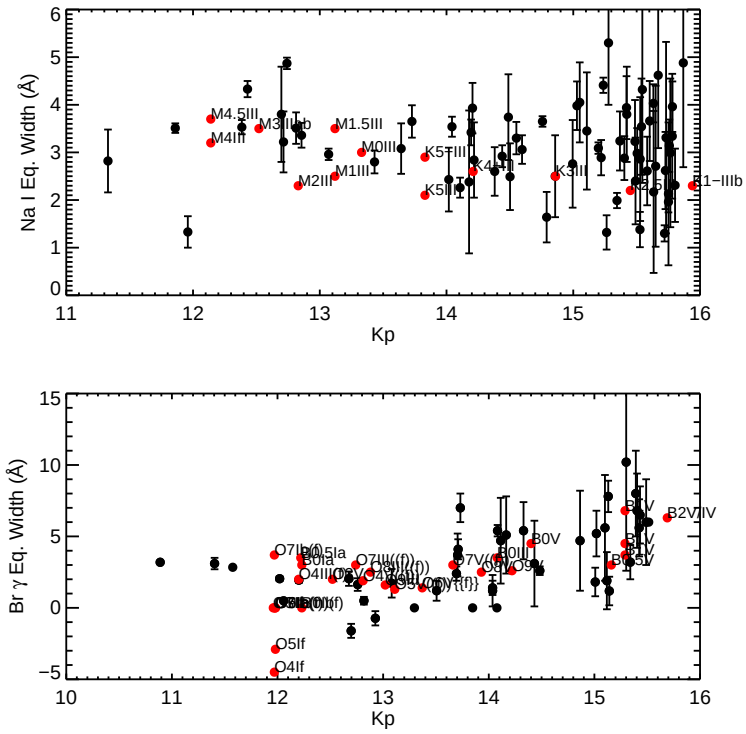

Figure 3.4 **Top**: equivalent width of the combination of Na I lines at 2.2062 and 2.2090 μm as a function of K' magnitude. Also plotted are equivalent width measurements of Na I from Förster Schreiber (2000) with spectral types corrected for the distance and extinction (A_k=3.0) toward the Galactic center (red). **Bottom:** equivalent width of the Br γ hydrogen line at 2.1661 μm. Equivalent width measurements from Hanson et al. (1996) are also plotted for O and B type stars, corrected for the distance and extinction (A_k=3.0) to the Galactic center (red).

in Figure 3.5, with a comparison to that derived from imaging at K'. The K' luminosity functions of the stars in the individual fields are similar to that of the total sample, with the notable exception of the western field, where there are fewer stars detected both in imaging and in spectroscopy. This difference in number of detected stars is most likely due to poor seeing on the night of observation and higher extinction in that region. Figures 3.7 and 3.8 shows the locations of the stars with their spectral types on a collapsed image of each of the OSIRIS fields.

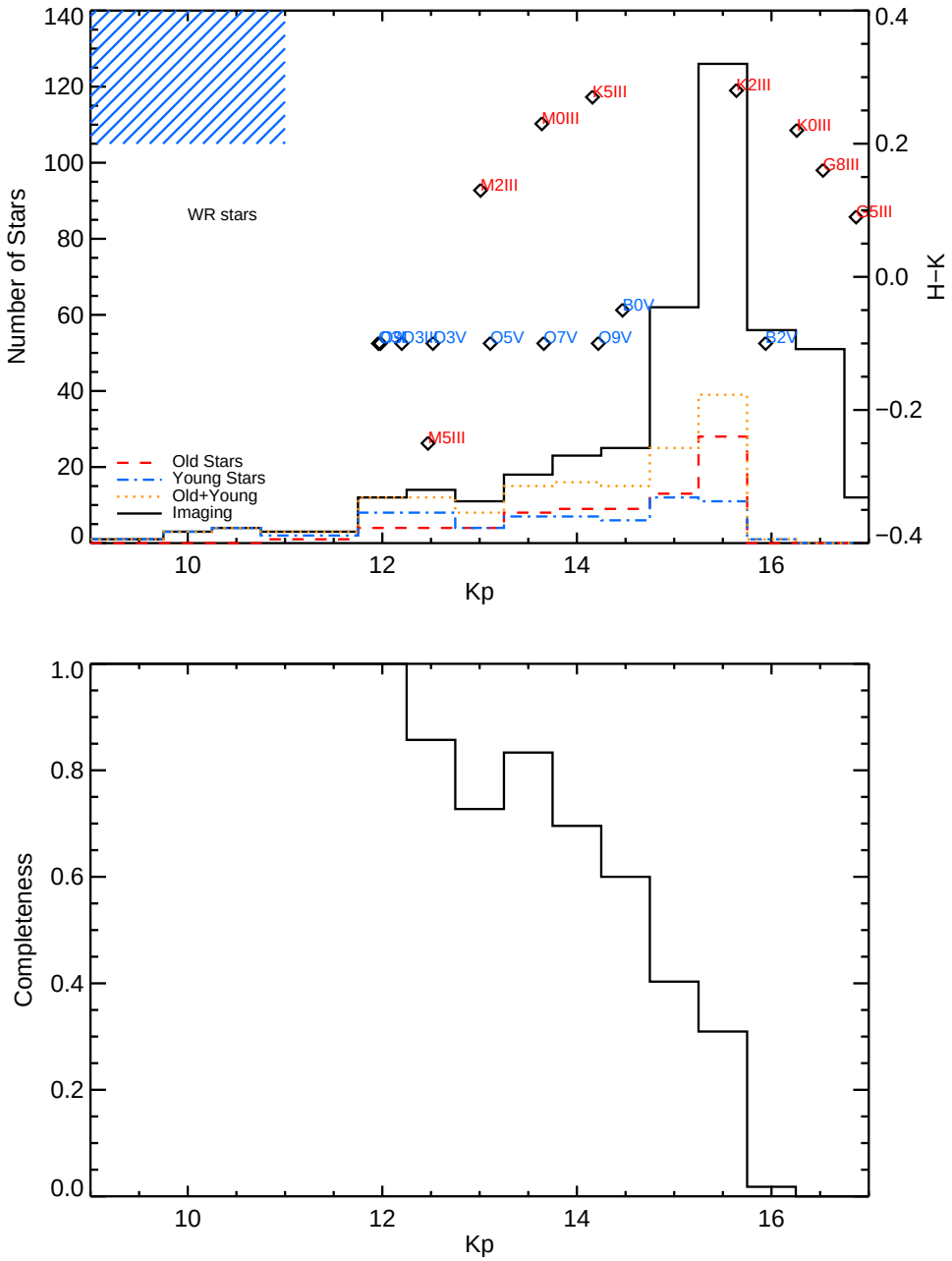

Figure 3.5 The K' luminosity function from the spectroscopic survey in comparison to that found from imaging. In the top plot, we also include for reference, the rough spectral types expected to be observable at each luminosity bin assuming $A_K = 3.0$ and a distance of 8 kpc. The axis on the right shows the H-K color associated with each of the spectral types (Ducati et al., 2001; Martins & Plez, 2006). The WR stars occupy a range in both K' and H-K colors.

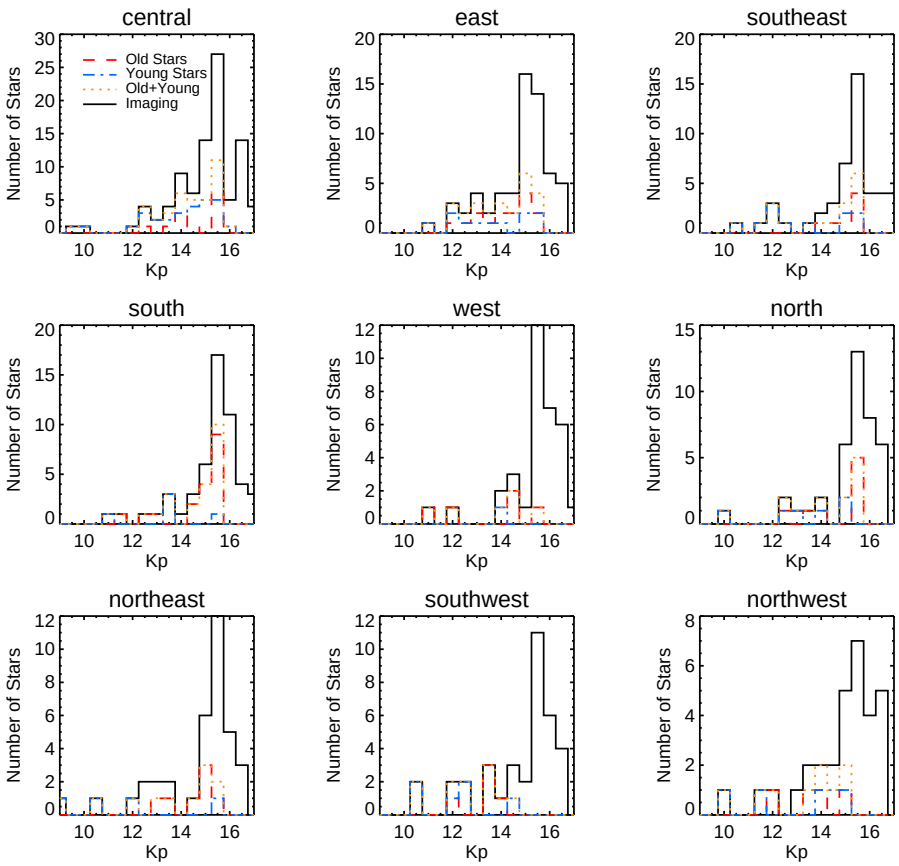

Figure 3.6 The K' luminosity function from the spectroscopic survey in comparison to imaging in each individual pointing.

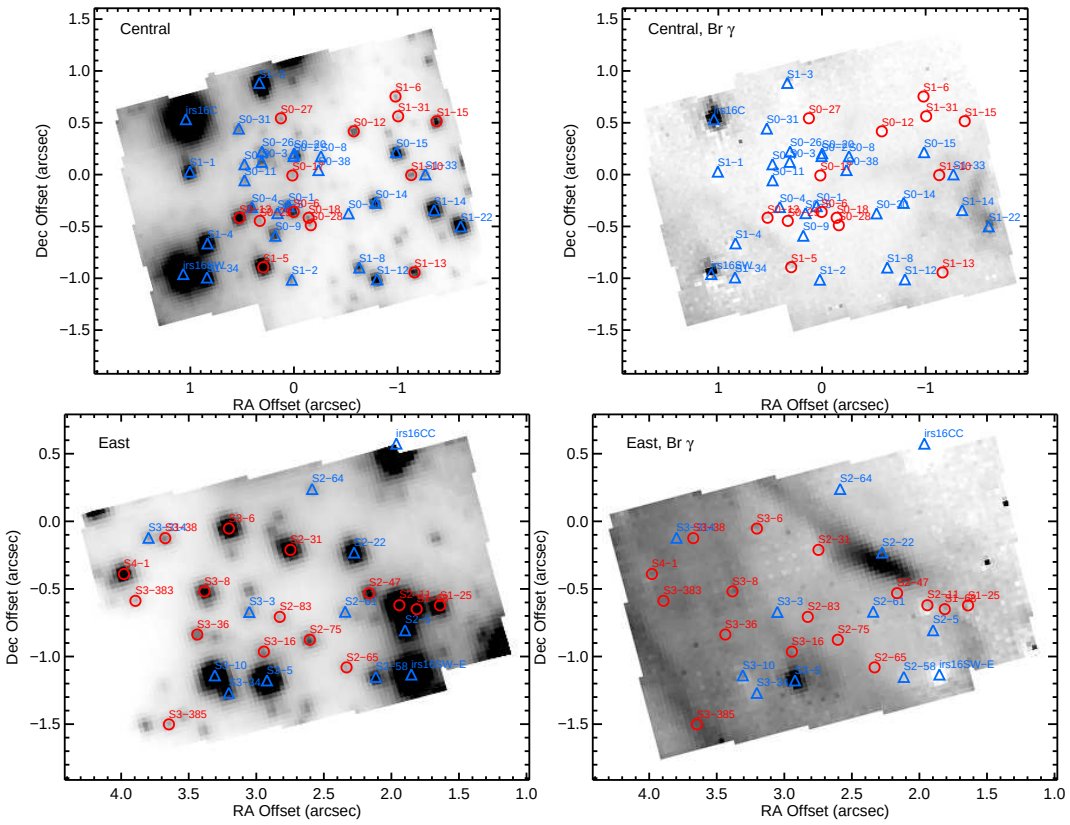

Figure 3.7 Images from collapsing the OSIRIS data cubes along the spectral dimension for each individual pointing of the survey. Right: median of all spectral channels. Left: spectral channels near the Br gamma line showing the gas emission. The images are oriented with north up and east to the left. Spectroscopically identified early (blue triangles) and late-type (red circles) stars are marked.

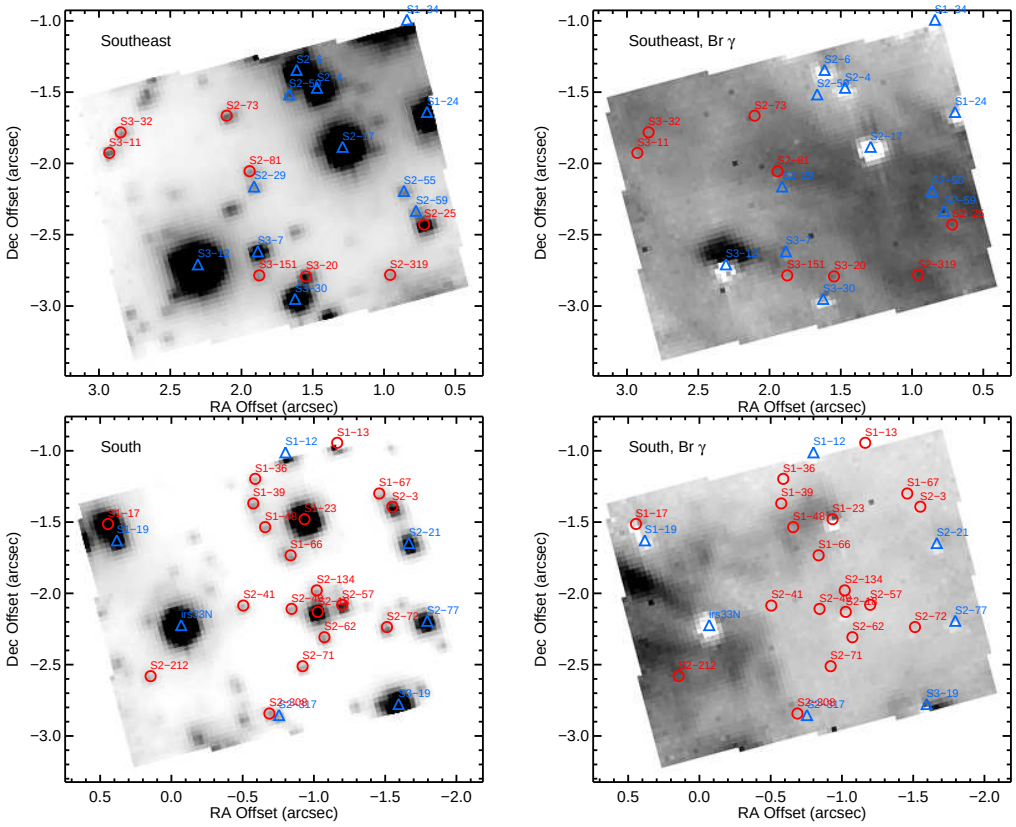

Figure 3.8 Similar to Figure 3.7, with additional OSIRIS fields.

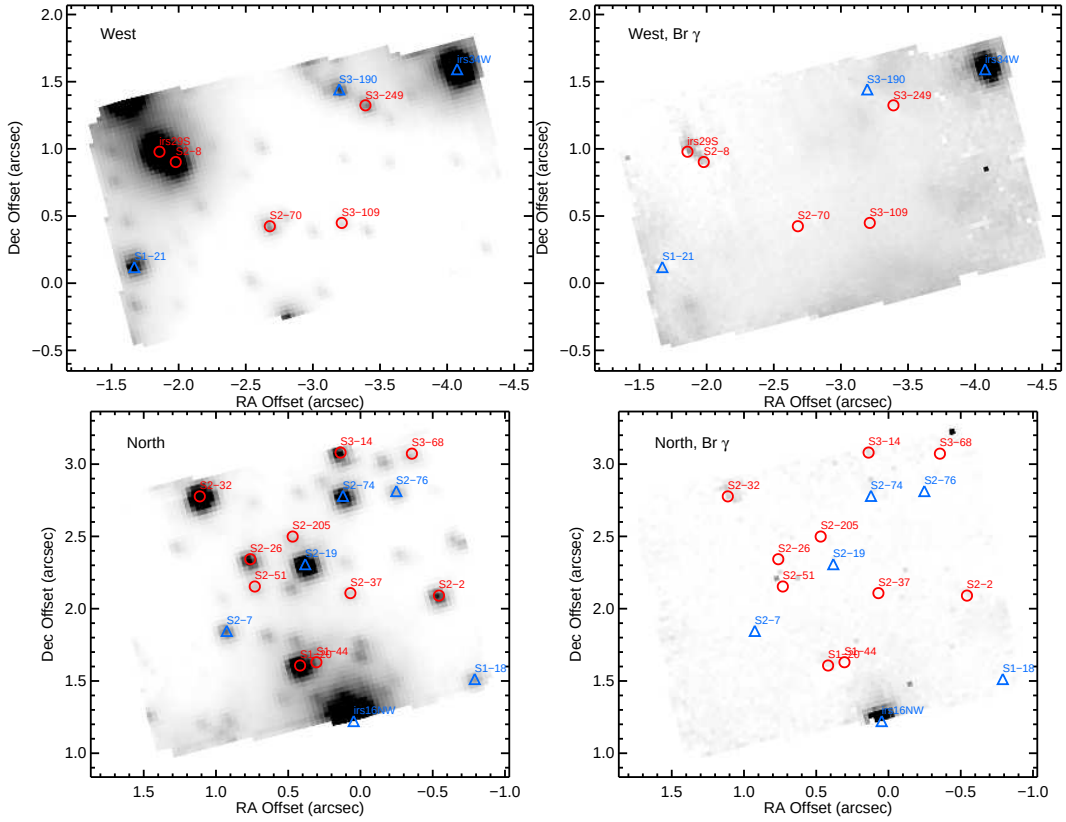

Figure 3.9 Similar to Figure 3.7, with additional OSIRIS fields.

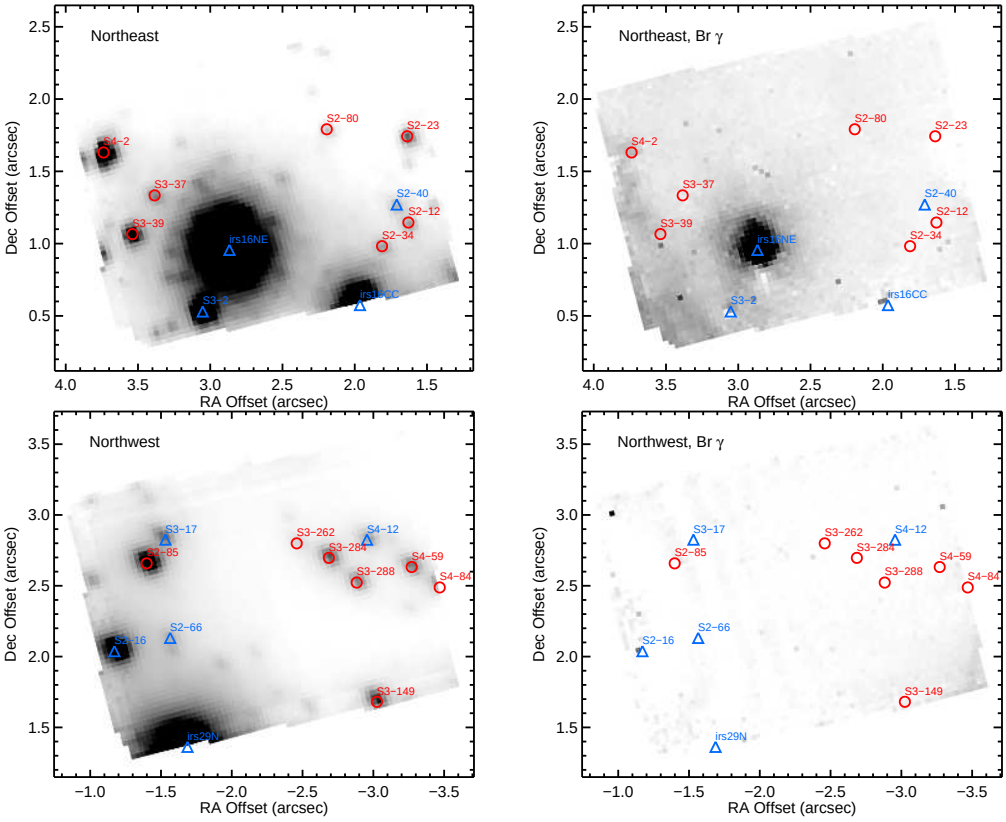

Figure 3.10 Similar to Figure 3.7, with additional OSIRIS fields.

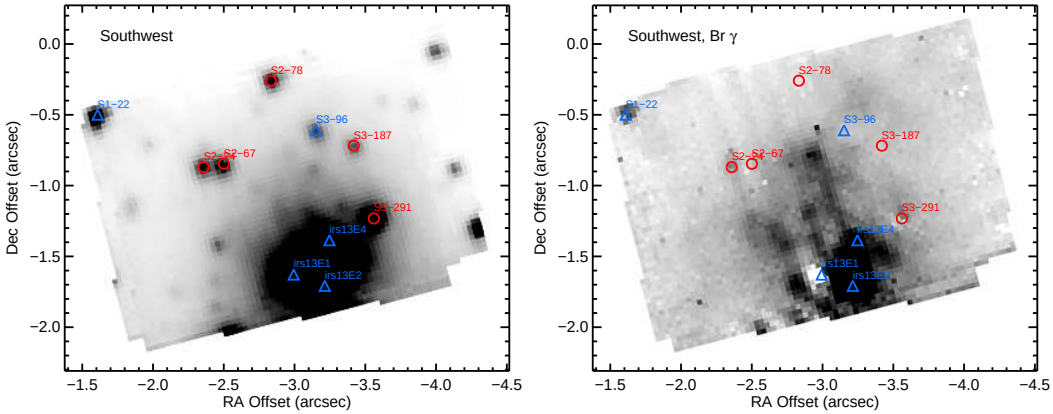

Figure 3.11 Similar to Figure 3.7, with additional OSIRIS fields.

Table 3.2. OSIRIS observations of late-type stars

Name	K′	RA offset (″)	DEC offset (″)	R (″)	Epoch	Note[a]	Na (Å)	σ_{Na} (Å)	N_{obs}[b]	SNR[c]	Field
S0-17	15.70	0.02	-0.09	0.10	2004.47	4	1.30	0.17	11	20	C
S0-6	14.20	0.05	-0.38	0.39	2002.69	4	2.92	0.83	9	44	C
S0-27	15.70	0.14	0.53	0.54	2003.34	1	3.80	0.41	6	12	C
S0-29	15.60	0.32	-0.46	0.56	2004.84	4	4.63	1.40	9	6	C
S0-28	15.80	-0.17	-0.55	0.57	2003.53	4	2.13	1.50	8	31	C
S0-12	14.40	-0.56	0.39	0.68	2002.69	4	2.60	0.51	4	33	C
S0-13	13.50	0.54	-0.44	0.69	2002.69	4	2.80	0.24	6	77	C
S1-5	12.80	0.34	-0.92	0.98	2002.69	4	3.22	0.64	4	45	C
S1-10	14.90	-1.13	-0.03	1.13	2002.99	4	2.50	0.86	5	25	C
S1-31	15.70	-0.98	0.56	1.13	2003.60	1	4.62	1.53	4	11	C
S1-6	15.50	-0.93	0.73	1.18	2003.34	1	3.54	1.01	2	18	C
S1-36	15.80	-0.63	-1.20	1.35	2003.58	1	2.31	0.77	4	18	S
S1-13	14.20	-1.12	-0.92	1.45	2002.91	4	2.38	1.50	3	21	C
S1-15	14.20	-1.36	0.52	1.45	2002.69	1	3.42	0.27	4	38	C
S1-39	15.40	-0.55	-1.37	1.48	2003.22	1	3.94	0.66	7	16	S
S1-17	12.50	0.47	-1.49	1.56	2002.69	1	4.33	0.17	4	85	S
S1-44	15.60	0.30	1.61	1.63	2003.48	1	4.03	0.40	5	22	N
S1-48	15.50	-0.62	-1.53	1.66	2004.20	1	3.23	0.87	10	32	S
S1-20	12.70	0.41	1.61	1.66	2002.69	1	4.87	0.12	12	57	N
S1-23	11.90	-0.93	-1.48	1.74	2002.69	1	3.51	0.10	10	77	S
S1-25	13.50	1.65	-0.63	1.76	2002.69	3	3.51	···	1	33	E
S1-66	15.60	-0.81	-1.76	1.94	2004.87	1	1.38	0.37	10	8	S
S1-67	15.60	-1.44	-1.32	1.95	2003.56	1	2.61	0.72	9	30	S
S1-68	13.40	1.86	-0.61	1.96	2002.69	1	2.47	0.52	4	50	E
S2-12	15.30	1.67	1.17	2.04	2003.08	1	4.41	0.16	5	18	NE
S2-34	15.40	1.81	0.97	2.05	2003.43	1	3.80	1.00	5	18	NE
S2-11	12.00	1.97	-0.62	2.07	2002.69	1	1.33	0.33	8	98	E
S2-3	14.50	-1.54	-1.41	2.09	2002.84	1	2.92	0.23	9	61	S
S2-37	15.80	0.08	2.10	2.11	2003.91	1	3.14	0.55	12	17	N
S2-2	14.10	-0.55	2.06	2.13	2002.88	1	2.26	0.21	11	42	N
S2-41	15.50	-0.47	-2.10	2.16	2004.41	1	2.86	1.30	10	36	S
S2-8	12.20	-1.84	0.96	2.08	2002.69	1	2.82	0.66	9	53	W

Table 3.2—Continued

Name	K′	RA offset (″)	DEC offset (″)	R (″)	Epoch	Note[a]	Na (Å)	σ_{Na} (Å)	N_{obs}[b]	SNR[c]	Field
S2-134	15.60	-0.99	-1.99	2.23	2005.79	1	3.66	0.84	10	8	S
S2-49	15.50	-0.83	-2.10	2.26	2004.14	1	2.88	0.46	10	19	S
S2-47	14.20	2.19	-0.53	2.25	2002.75	1	2.84	0.79	10	41	E
S2-51	15.90	0.76	2.18	2.31	2004.88	1	4.88	2.19	12	23	N
S2-18	13.30	-0.98	-2.14	2.35	2002.83	3	3.18	0.17	10	57	S
S2-23	14.80	1.66	1.77	2.42	2002.93	1	3.64	0.38	4	36	NE
S2-57	14.70	-1.21	-2.12	2.44	2003.76	1	3.06	0.30	10	45	S
S2-24	13.80	-2.33	-0.90	2.50	2003.30	7	6.05	1.72	4	18	SW
S2-26	13.70	0.74	2.42	2.53	2002.65	3	3.65	0.34	12	43	N
S2-62	15.20	-1.07	-2.32	2.56	2004.67	1	2.89	0.37	10	31	S
S2-25	14.10	0.74	-2.45	2.56	2003.50	1	3.54	0.21	8	91	SE
S2-205	15.80	0.48	2.51	2.56	2005.54	1	3.34	1.31	12	22	N
S2-65	15.80	2.35	-1.06	2.58	2004.13	1	1.96	0.22	10	18	E
S2-212	15.70	0.18	-2.59	2.59	2006.75	1	3.31	2.01	7	12	S
S2-67	13.80	-2.50	-0.85	2.63	2003.29	7	6.59	0.75	4	28	SW
S2-70	14.50	-2.64	0.41	2.67	2003.98	1	3.74	0.90	11	29	W
S2-71	15.30	-0.90	-2.53	2.68	2004.72	1	1.99	0.16	10	30	S
S2-72	15.10	-1.46	-2.28	2.71	2004.32	1	3.98	0.51	10	32	S
S2-73	15.20	2.16	-1.64	2.72	2003.15	1	3.09	0.12	11	49	SE
S2-75	14.50	2.63	-0.89	2.78	2002.69	1	2.49	0.70	10	39	E
S2-31	13.10	2.81	-0.20	2.81	2002.69	1	2.96	0.12	10	71	E
S2-78	13.80	-2.81	-0.29	2.82	2003.53	7	4.49	0.73	3	34	SW
S2-80	15.60	2.23	1.78	2.85	2003.58	1	2.40	0.91	5	20	NE
S2-81	15.60	1.97	-2.07	2.86	2004.75	1	2.98	0.53	11	22	SE
S2-83	15.60	2.86	-0.69	2.94	2003.62	1	2.17	1.70	10	21	E
S2-319	15.70	0.99	-2.79	2.96	2005.71	1	2.62	0.81	8	14	SE
S2-85	12.20	-1.26	2.70	2.98	2003.64	7	4.98	0.16	5	55	NW
S2-32	12.40	1.12	2.78	2.99	2003.05	1	3.53	0.15	6	59	N
S3-68	15.80	-0.35	3.06	3.08	2005.93	1	3.96	0.53	5	21	N
S3-14	13.90	0.10	3.09	3.09	2004.54	1	1.98	···	1	18	N
S3-16	15.30	2.99	-0.95	3.13	2003.76	1	5.30	1.30	10	24	E
S3-20	14.90	1.58	-2.80	3.21	2003.83	1	1.64	0.53	11	54	SE

Table 3.2—Continued

Name	K′	RA offset (″)	DEC offset (″)	R (″)	Epoch	Note[a]	Na (Å)	σ_{Na} (Å)	N_{obs}[b]	SNR[c]	Field
S3-6	12.90	3.22	0.01	3.22	2002.80	1	3.36	0.26	10	77	E
S3-109	15.60	-3.20	0.43	3.23	2006.75	1	4.32	1.96	11	20	W
S3-149	13.30	-2.92	1.68	3.37	2005.93	7	4.52	0.08	3	23	NW
S3-151	15.70	1.90	-2.78	3.37	2006.22	1	2.99	1.56	11	16	SE
S3-32	15.50	2.91	-1.77	3.41	2004.51	1	3.24	0.62	9	37	SE
S3-8	14.00	3.41	-0.49	3.44	2002.81	1	2.43	0.67	10	56	E
S3-187	14.40	-3.40	-0.74	3.48	2006.75	7	-4.66	1.12	4	13	SW
S3-11	15.10	2.96	-1.93	3.53	2004.12	3	4.05	0.84	4	35	SE
S3-36	14.70	3.46	-0.83	3.55	2003.76	1	3.65	0.11	9	57	E
S3-249	14.70	-3.38	1.32	3.63	2006.75	1	3.30	0.34	11	33	W
S3-37	15.10	3.39	1.35	3.65	2004.66	1	3.45	1.23	5	17	NE
S3-262	15.10	-2.34	2.83	3.67	2006.75	7	3.77	0.25	6	26	NW
S3-38	15.00	3.69	-0.11	3.69	2005.34	1	2.76	0.92	9	33	E
S3-39	13.60	3.57	1.10	3.73	2002.97	1	3.08	0.53	3	32	NE
S3-284	13.70	-2.58	2.72	3.74	2006.75	7	5.43	0.33	6	53	NW
S3-288	14.30	-2.77	2.54	3.76	2006.75	7	5.49	0.19	6	44	NW
S3-291	12.20	-3.55	-1.26	3.76	2006.58	7	5.59	0.38	4	46	SW
S3-385	15.30	3.67	-1.50	3.96	2005.81	1	1.32	0.36	6	26	E
S4-1	13.50	4.02	-0.37	4.04	2003.92	1	3.09	0.25	9	102	E
S4-2	13.00	3.75	1.67	4.10	2004.01	1	3.51	0.33	3	52	NE
S4-59	13.70	-3.16	2.65	4.13	2006.75	7	3.50	0.09	6	38	NW
S4-84	14.00	-3.35	2.49	4.18	2006.75	7	5.53	0.24	2	31	NW

[a]1. Spectral type first reported in this work. Recent spectral identification: 2. Paumard et al. (2006) 3. Genzel et al. (2000) 4. Gillessen et al. (2009)

[b]Each observation has an integration time of 900 s.

[c]Signal to noise per pixel calculated between 2.212 to 2.218 μm.

Table 3.3. OSIRIS observations of early-type stars

Name	K′	RA offset (″)	DEC offset (″)	R (″)	Epoch	Note[a]	Br γ[b] (Å)	$\sigma_{Br\gamma}$ (Å)	N_{obs}[c]	SNR[d]	Field
S0-2	14.10	···	0.16	0.16	2005.61	2	3.90	1.50	11	67	C
S0-1	14.70	0.04	-0.26	0.27	2006.30	2	0.50	0.30	9	31	C
S0-19	15.50	-0.04	0.35	0.35	2006.25	2	5.70	2.30	11	16	C
S0-3	14.50	0.31	0.12	0.33	2006.38	2	5.40	3.60	9	21	C
S0-5	15.10	0.18	-0.36	0.40	2006.32	2	7.80	1.10	9	15	C
S0-4	14.50	0.40	-0.28	0.49	2005.83	2	5.40	6.00	10	1	C
S0-7	15.50	0.49	0.10	0.49	2006.36	2	6.50	2.00	10	12	C
S0-11	15.30	0.50	-0.05	0.50	2006.73	2	10.20	7.60	9	21	C
S0-9	14.40	0.19	-0.58	0.61	2006.74	4	5.40	2.00	7	38	C
S0-31	15.10	0.54	0.44	0.70	2006.47	2	6.01	1.54	6	21	C
S0-14	13.70	-0.77	-0.27	0.82	2005.51	2	4.10	0.70	7	76	C
S0-15	13.70	-0.95	0.24	0.98	2005.80	2	2.40	0.50	7	67	C
S1-3	12.10	0.40	0.88	0.96	2004.98	2	···	···	5	79	C
S1-1	13.10	1.01	0.03	1.01	2005.20	4	1.72	1.00	5	57	C
S1-2	14.90	0.01	-1.01	1.01	2005.93	2	4.70	3.50	5	19	C
S1-4	12.60	0.83	-0.67	1.06	2005.84	1	···	···	5	52	C
S1-8	14.20	-0.63	-0.89	1.08	2006.17	2	5.10	2.70	4	42	C
IRS16NW	10.10	0.05	1.22	1.22	2004.74	2	···	···	···	···	
IRS16C	9.90	1.10	0.51	1.21	2003.89	2	···	···	···	···	
S1-33	15.00	-1.25	-0.01	1.25	2006.26	1	5.20	1.60	5	17	C
S1-34	13.20	0.85	-0.99	1.31	2006.38	1	···	···	3	52	C
S1-12	13.80	-0.80	-1.01	1.29	2006.21	2	3.70	1.50	4	40	C
S1-14	12.80	-1.34	-0.33	1.38	2005.49	6	0.50	0.27	3	52	C
IRS16SW	10.10	1.06	-0.96	1.44	2004.89	2	···	···	···	···	
S1-19	13.80	0.38	-1.62	1.66	2005.45	1	7.00	1.00	4	37	S
S1-18	15.00	-0.76	1.51	1.69	2006.56	1	1.81	1.00	2	24	N
S1-21	13.30	-1.66	0.13	1.66	2006.16	2	···	···	5	47	W
S1-22	12.70	-1.61	-0.49	1.68	2005.65	2	-1.61	0.49	3	61	C
S1-24	11.60	0.71	-1.62	1.77	2005.64	2	2.84	···	1	74	SE
S2-5	13.30	1.91	-0.81	2.07	2005.68	1	···	···	7	58	E
IRS16CC	10.60	1.99	0.56	2.06	2004.57	2	···	···	···	···	
S2-4	12.30	1.47	-1.47	2.08	2006.04	2	1.94	0.19	11	149	SE

Table 3.3—Continued

Name	K′	RA offset (″)	DEC offset (″)	R (″)	Epoch	Note[a]	Br γ[b] (Å)	$\sigma_{Br\gamma}$ (Å)	N_{obs}[c]	SNR[d]	Field
S2-6	12.00	1.61	-1.35	2.10	2004.69	2	2.04	0.16	7	103	SE
S2-7	14.10	0.95	1.84	2.08	2006.15	2	···	···	12	54	N
IRS29N	10.30	-1.58	1.41	2.12	2005.07	2	···	···	···	···	NW
IRS16SW-E	11.00	1.86	-1.14	2.18	2005.52	2	···	···	···	···	
IRS33N	11.40	-0.05	-2.21	2.21	2006.19	2	3.10	0.40	10	104	S
S2-17	10.90	1.29	-1.88	2.28	2005.14	2	3.19	0.07	11	125	SE
S2-50	15.50	1.68	-1.52	2.26	2005.38	1	8.00	3.00	11	16	SE
S2-16	11.90	-1.02	2.07	2.31	2005.40	2	···	···	1	41	NW
S2-22	12.90	2.30	-0.24	2.31	2005.33	6	-0.73	0.50	10	78	E
S2-19	12.60	0.42	2.31	2.34	2005.53	2	2.04	0.50	12	68	N
S2-21	13.50	-1.66	-1.64	2.34	2006.34	1	1.20	0.70	8	71	S
S2-55	15.40	0.88	-2.19	2.36	2006.53	1	3.20	1.20	11	29	SE
S2-58	14.10	2.14	-1.16	2.43	2005.74	1	4.70	3.00	7	41	E
S2-59	15.40	0.79	-2.33	2.46	2006.48	1	5.60	2.00	10	25	SE
S2-61	15.50	2.37	-0.67	2.47	2006.56	1	6.00	3.00	10	16	E
S2-74	13.30	0.15	2.78	2.78	2006.16	2	···	···	12	81	N
S2-77	13.80	-1.78	-2.19	2.82	2006.16	1	1.40	0.50	9	54	S
S2-76	15.20	-0.23	2.81	2.82	2006.76	1	1.18	1.00	12	38	N
S2-317	15.60	-0.74	-2.86	2.95	2006.40	1	5.10	1.00	3	21	S
IRS16NE	9.10	2.87	1.01	3.04	2003.62	2	···	···	···	···	
S3-2	12.10	3.06	0.53	3.11	2005.43	1	0.49	0.04	3	47	NE
S3-3	15.10	3.06	-0.67	3.14	2006.47	1	1.90	2.00	10	21	E
S3-5	12.20	2.94	-1.18	3.16	2005.66	2	···	···	10	87	E
S3-17	14.10	-1.42	2.86	3.19	2006.60	7	···	···	···	···	NW
S3-96	14.50	-3.13	-0.62	3.19	2006.82	2	···	···	4	28	SW
S3-7	13.90	1.91	-2.61	3.23	2006.34	1	···	···	11	76	SE
IRS13E1	10.90	-2.97	-1.63	3.39	2006.50	2	5.17	1.04	4	108	SW
S3-30	12.80	1.64	-2.96	3.38	2006.39	2	1.63	0.44	8	56	SE
S3-34	13.50	3.22	-1.26	3.46	2006.29	1	2.12	1.28	9	46	E
S3-190	14.10	-3.17	1.45	3.49	2006.47	1	1.20	1.10	11	55	W
IRS13E4	12.00	-3.22	-1.39	3.51	2006.23	2	···	···	4	66	SW
S3-10	12.40	3.33	-1.14	3.52	2005.99	2	···	···	10	81	E

Table 3.3—Continued

Name	K′	RA offset (″)	DEC offset (″)	R (″)	Epoch	Note[a]	Br γ[b] (Å)	$\sigma_{Br\gamma}$ (Å)	N_{obs}[c]	SNR[d]	Field
S3-12	12.00	2.37	-2.73	3.61	2001.39	1	···	···	11	114	SE
IRS13E2	10.80	-3.19	-1.71	3.62	2006.35	2	···	···	3	36	SW
S3-314	15.40	3.81	-0.12	3.82	2006.43	1	6.80	2.60	9	26	E
S4-12	14.90	-2.82	2.86	4.02	2006.40	7	···	···	···	···	NW

[a]1. Spectral type first reported in this work. Recent spectral identification: 2. Paumard et al. (2006) 3. Genzel et al. (2000) 4. Gillessen et al. (2009) 5. Bartko et al. (2009).

[b]Each observation has an integration time of 900 s.

[c]Stars with no reported equivalent widths have no detectable Br γ lines (see Section 3.4), with the exception of the IRS 16 sources, which all have strong Br γ emission lines from strong winds.

[d]Signal to noise per pixel calculated between 2.212 to 2.218 μm.

Table 3.4. OSIRIS spectra with unknown spectral type

Name	K′	RA offset (″)	DEC offset (″)	R (″)	Epoch	SNR[a]
S0-35	15.3	0.06	0.97	0.97	2003.77	16
S1-26	15.6	-0.92	0.39	1	2003.07	12
S1-29	15.4	1.08	0.17	1.09	2005.09	11
S1-32	15.3	-0.96	-0.64	1.15	2003.21	20
S1-7	15.9	-1.03	-0.53	1.16	2003.86	13
S1-85	15.5	0.92	-0.82	1.23	2006.75	4
S1-40	15.9	-1.39	-0.62	1.52	2004.23	7
S1-41	15.8	0.99	1.15	1.52	2003.69	4
S1-42	15.9	0.94	1.26	1.57	2004.04	9
S1-45	15.3	-1.27	1.04	1.65	2003.04	13
S1-47	15.6	-1.58	0.46	1.65	2003.14	1
S1-50	15.4	1.5	0.68	1.65	2003.7	9
S1-128	15.8	1.33	-0.99	1.66	2006.55	0
S1-51	15	-1.65	-0.18	1.66	2002.99	10
S1-52	15.2	0	1.67	1.67	2003.15	28
S1-53	15.3	1.67	-0.12	1.67	2003.12	11
S1-54	15.5	-1.52	0.74	1.69	2004.25	3
S1-55	15.5	1.59	0.6	1.69	2004.17	7
S1-56	15.8	-1.11	1.35	1.75	2003.85	11
S1-61	15.9	-1.49	-1	1.79	2003.96	6
S1-62	15.3	0.5	1.75	1.82	2003.21	19
S1-59	15.5	0.02	1.82	1.82	2003.33	27
S1-147	15.9	1.18	-1.47	1.89	2006.75	7
S1-64	15.5	0.64	1.81	1.92	2003.08	13
S1-159	15.9	1.3	-1.43	1.93	2005.94	9
S1-65	15.7	1.46	1.27	1.93	2003.85	5
S2-89	15.9	1.07	-1.7	2.01	2006.75	5
S2-42	15.6	0.46	2.1	2.15	2004.02	23
S2-200	15.7	-2.53	0	2.53	2005.25	12
S2-63	15.4	-0.65	2.48	2.56	2003.98	12
S2-219	15.8	-1.6	-2.07	2.62	2005.34	8
S2-261	15.6	-2.61	1	2.8	2006.04	11

Table 3.4—Continued

Name	K′	RA offset (″)	DEC offset (″)	R (″)	Epoch	SNR[a]
S2-268	15.5	-2.78	0.49	2.82	2006.32	13
S2-304	15.9	2.52	1.47	2.91	2006.39	12
S2-306	15.6	-0.48	-2.89	2.93	2006.75	17
S2-84	15.6	1.65	-2.47	2.97	2004.29	26
S3-48	15.9	-3	0.37	3.02	2006.32	15
S3-50	15.7	-1.87	-2.38	3.03	2006.75	13
S3-51	15.1	-0.15	3.02	3.03	2005.88	15
S3-62	15.7	2.68	-1.48	3.06	2006.4	28
S3-65	15.7	-1.27	-2.8	3.07	2005.72	11
S3-4	14.7	3.08	-0.52	3.13	2002.91	28
S3-90	15.8	2.74	-1.56	3.15	2005.21	30
S3-91	15.7	-1.73	-2.67	3.18	2006.75	8
S3-116	15.9	2.25	2.37	3.27	2006.11	9
S3-24	15.6	3.26	0.41	3.29	2004.87	4
S3-167	15.5	-3.08	1.42	3.4	2006.75	16
S3-169	15.5	-3.39	0.38	3.41	2006.75	27
S3-31	15.5	3.4	0.38	3.42	2004.42	7
S3-33	15.4	3.32	-0.85	3.43	2004.25	16
S3-286	15.3	3.42	-1.54	3.75	2004.66	13
S3-319	15.4	3.55	-1.42	3.83	2006.39	17
S4-47	15.9	2.56	-3.23	4.12	2006.75	11
S4-67	15.7	2.8	-3.05	4.14	2006.75	7

[a]Signal to noise per pixel calculated between 2.212 to 2.218 μm.

3.5 Results

With spectroscopic identification of the stars brighter than $K' \sim 15.5$, we are able to separate the presumably dynamically relaxed old stars from the unrelaxed young population. The stellar number density profile is constructed in radial bins of $0.''5$ over the area that was sampled in this survey out to a radius of $\sim 3''$, with error bars scaling as $\sqrt{N}$, where N is the number of stars in each bin. It is clear that, while the number density of early-type stars increases quite rapidly toward the central arcsecond, the late-type stars have a very flat distribution (Figure 3.12). Outside the central arcsecond, the projected number density of early-type stars drops to about half that of the late-type stars. For a quantitative comparison to stellar cusp models, we fit a power law to the surface number density of both populations. The late-type population is best fit with a power law slope $\Gamma_{old} =$

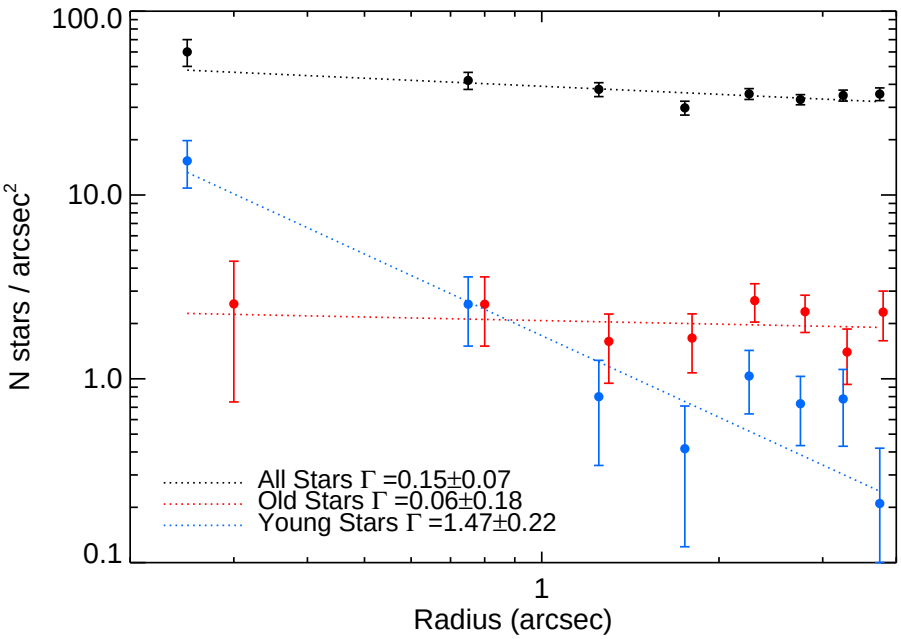

Figure 3.12 Plot of the surface number density as a function of projected distance from Sgr A* in the plane of the sky for different populations: old (late-type, red), young (early-type, blue), and total number counts from K' imaging.

0.06±0.18, while for the early-type stars, $\Gamma_{young} = 0.97 \pm 0.28$. For comparison, we also measured the projected stellar number density over the same survey region using LGS AO K' imaging from July 2008, which is much deeper ($K' < 20$), but with no spectroscopic discrimination. We find that $\Gamma_{imaging} = 0.15 \pm 0.07$, comparable to that found by Schödel et al. (2007) using only number counts. The spectroscopically determined late-type slope is flatter than that determined from number counts alone, but is consistent within the $\sim 2\sigma$ formal fitting errors.

The survey has complete azimuthal coverage out to a radial distance of $\sim 1.''5$ from Sgr A*. Beyond this radius, the radial coverage extends out to $\sim 4''$, but the azimuthal coverage is complete due to two fields missing in the northwest and southwest. We find that these missing two fields do not significantly impact

Table 3.5. Results and survey completeness

					Observed		A_K Corrected[d]	
Field	N_{SF}[a]	N_{ID}[b]	A_k[c]	RMS_{A_k}	K′[e]	Completeness	K′	Completeness
C	100	28	3.24	0.04	15.5 - 16.0	0.4	15.5 - 16.0	0.4
E	37	25	3.05	0.06	15.5 - 16.0	0.3	15.0 - 15.5	0.3
SE	60	25	3.29	0.10	15.5 - 16.0	0.4	15.0 - 15.5	0.5
S	35	6	3.28	0.05	15.5 - 16.0	0.6	15.0 - 15.5	0.6
W	35	19	3.44	0.12	14.5 - 15.0	0.7	14.0 - 14.5	0.4
N	40	14	3.39	0.12	15.5 - 16.0	0.4	15.0 - 15.5	0.4
NE	32	7	3.13	0.07	15.0 - 15.5	0.5	15.0 - 15.5	0.5
SW	32	10	3.43	0.20	14.5 - 15.0	0.3	14.0 - 14.5	0.4
NW	65	11	3.68	0.10	15.0 - 15.5	0.4	14.0 - 14.5	0.8

[a]Number of stars detected by *StarFinder*.

[b]Number of stars with determined spectral types.

[c]Extinction values from Buchholz et al. (2009).

[d]Extinction correction using (A_k - 3.0), with A_k from the extinction map in Buchholz et al. (2009).

[e]Faintest magnitude bin where the completeness is at least 30%.

the radial profile of the late-type stars, as removing one or two of the outer observed fields from the analysis leads to the same power law slope, within the measurement uncertainties. In addition, previous observations of the late-type stars in this region have found the distribution to be isotropic (e.g. Genzel et al., 2003b; Trippe et al., 2008).

Potential systematic errors to the radial profile measurement may arise from variable extinction and incompleteness between each field. In order to study how these two factors impact our result, the radial profile was computed using stars with extinction corrected magnitudes only over regions that are at least 30% complete. To do so, the extinction map reported by Buchholz et al. (2009) was used to correct for the variations in extinction between each star by adding $A_K - 3.0$ to each star to bring them to the same canonical $A_K = 3.0$ extinction to the Galactic center (see Table 3.5 for the average and RMS value of A_K in each field). Then, the K' luminosity function was recomputed for each field to

Table 3.6. Field Completeness

Magnitude Bin[a]	Central	E	SE	S	W	N	NE	SW	NW
9.00	0.00	0.00	0.00	0.00	0.00	0.00	1.00	0.00	0.00
9.50	1.00	0.00	0.00	0.00	0.00	0.00	0.00	0.00	0.00
10.00	1.00	0.00	0.00	0.00	0.00	1.00	0.00	0.00	1.00
10.50	0.00	0.00	1.00	0.00	0.00	0.00	1.00	1.00	0.00
11.00	0.00	1.00	0.00	1.00	1.00	0.00	0.00	0.00	0.00
11.50	0.00	0.00	1.00	1.00	0.00	0.00	0.00	0.00	1.00
12.00	1.00	1.00	1.00	0.00	1.00	0.00	1.00	1.00	1.00
12.50	1.00	1.00	1.00	1.00	0.00	1.00	0.00	1.00	0.00
13.00	1.00	0.75	0.00	1.00	0.00	1.00	0.50	0.00	0.00
13.50	0.75	1.00	1.00	1.00	0.00	1.00	0.50	1.00	0.50
14.00	0.67	0.75	0.50	0.00	0.50	1.00	0.00	1.00	1.00
14.50	0.83	0.50	0.33	0.67	0.67	0.00	1.00	0.33	0.50
15.00	0.36	0.38	0.43	0.67	0.00	0.33	0.50	0.00	0.40
15.50	0.41	0.29	0.38	0.59	0.08	0.38	0.17	0.00	0.00
16.00	0.20	0.00	0.00	0.00	0.00	0.00	0.00	0.00	0.00

[a]Left side of the magnitude bin.

Table 3.7. Extinction Corrected Field Completeness

Magnitude Bin[a]	Central	E	SE	S	W	N	NE	SW	NW
9.00	0.00	0.00	0.00	0.00	0.00	0.00	0.00	0.00	0.00
9.50	1.00	0.00	0.00	0.00	0.00	1.00	0.00	0.00	1.00
10.00	0.00	0.00	0.00	0.00	0.00	0.00	1.00	1.00	0.00
10.50	0.00	1.00	1.00	0.00	1.00	0.00	0.00	1.00	0.00
11.00	0.00	0.00	1.00	1.00	0.00	0.00	0.00	1.00	1.00
11.50	1.00	1.00	1.00	1.00	1.00	0.00	0.00	1.00	1.00
12.00	1.00	1.00	1.00	1.00	0.00	1.00	1.00	1.00	0.00
12.50	1.00	1.00	0.00	1.00	0.00	1.00	0.33	0.00	0.00
13.00	1.00	0.80	0.00	1.00	0.00	1.00	0.00	0.00	0.67
13.50	0.67	1.00	0.67	1.00	1.00	1.00	1.00	1.00	1.00
14.00	0.71	0.75	0.00	0.50	0.40	0.00	0.00	0.40	0.75
14.50	0.83	0.50	0.33	0.75	0.00	0.33	0.50	0.00	0.00
15.00	0.36	0.33	0.47	0.62	0.09	0.40	0.45	0.00	0.00
15.50	0.31	0.25	0.00	0.14	0.00	0.10	0.00	0.00	0.00
16.00	0.00	0.00	0.00	0.00	0.00	0.00	0.00	0.00	0.00
16.50	0.07	0.00	0.00	0.00	0.00	0.00	0.00	0.00	0.00

[a]Left side of the magnitude bin.

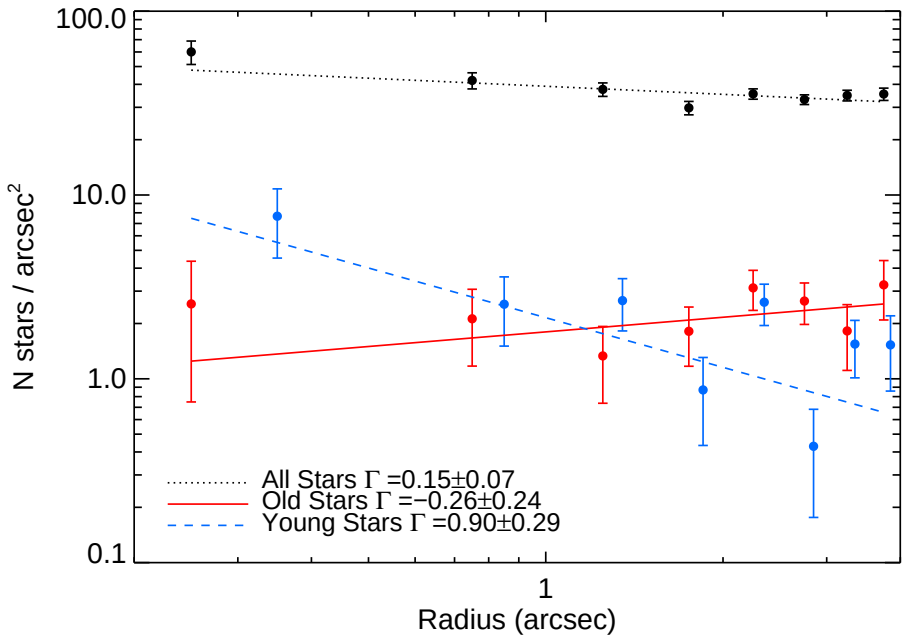

Figure 3.13 Plot of the surface number density as a function of projected distance from Sgr A* in the plane of the sky for different populations: old (late-type, red), young (early-type, blue), and total number counts from K' imaging. These radial profiles have been corrected for completeness and extinction using the method detailed in Section 3.5.

determine the K' magnitude bin beyond which the completeness falls to less than 30%. Table 3.5 shows this magnitude bin for each field before and after extinction correction. This separates the fields into three groups in terms of their 30% completeness : all fields are at least 30% complete down to $K' = 14.5$; all fields except W, SW, and NW are complete to $K' = 15.5$; the central field is complete to $K' = 16.0$. We calculate the radial profiles in each magnitude bin using only fields that are at least 30% complete at that magnitude. For all stars with $K' < 14.5$, we use all the fields, while for stars with $14.5 \leq K' < 15.5$, the western field was dropped from the measurement; the $15.5 \leq K' < 16.0$ magnitude bin was not included because only the central field is complete to at

least 30% at that magnitude. The radial profiles from the $K' < 14.5$ and $14.5 \leq K' < 15.5$ magnitude bins were then summed to produce the final measurement of the surface density, with errors added in quadrature (see Figure 3.13). A total of 60 early-type and 69 late-type stars are included in the final radial profile measurement. The early-type stars have $\Gamma_{young} = 0.90 \pm 0.29$, while for the late-type stars, $\Gamma_{old} = -0.26 \pm 0.24$. Neither of these values differ significantly from the case without extinction and completeness correction. The rest of the analysis will use these values for the measured surface number density profile.

Beyond a radius of $1''$, there are more young stars detected in the eastern and southeastern fields compared to the other observed regions. This excess is in the direction of the major axis of the projected coherent disk of young stars orbiting in the clockwise direction in the plane of the sky (Lu et al., 2009). however, after accounting for the completeness and differences in A_K, neither the number of young, nor old stars shows a statistically significant excess.

3.6 Discussion

The effects of projection of a three-dimensional cluster onto the plane of the sky must be taken into account for quantitative interpretations of the measured surface density profile. The projection onto the sky plane of a spherically symmetric cluster can be done using the integral:

$$\Sigma(R) = 2 \int_R^\infty \frac{rn(r)dr}{\sqrt{r^2 - R^2}} \tag{3.1}$$

where R is the distance from the center of the cluster in the plane of the sky, r is the physical radius of the star cluster, $\Sigma(R)$ is the projected surface density, and $n(r)$ is the volume number density. Because this integral diverges for all $\gamma < 1.0$,

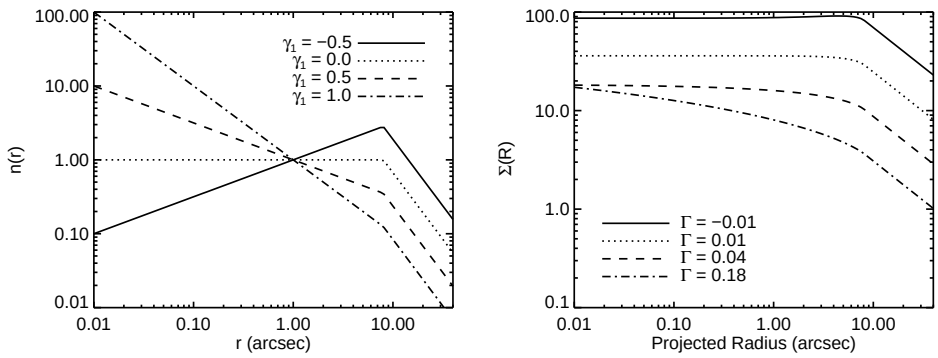

Figure 3.14 Left: broken power law density profiles with break radius, $r_{break} = 8.0''$ and outer power law $\gamma_2 = 2.0$, and varying inner power laws γ_1. Right: the projected surface number density profile of each of the broken power laws. The fitted inner surface density power law Γ is flat for $\gamma_1 \lesssim 0.5$.

where $n(r) \propto r^{-\gamma}$, the density in the outer region of the cluster must fall off steeply to accommodate a shallow power law at the center of the cluster. While we do not observe a break in the cluster density profile within our $4''$ survey, one was observed by Schödel et al. (2007) and others at scales larger than our survey. In order to account for the outer region of the star cluster, we therefore model the number density profile as a broken power law:

$$n(r) \propto \begin{cases} r^{-\gamma_1} & r < r_{break}, \\ r^{-\gamma_2} & r \geq r_{break}. \end{cases} \tag{3.2}$$

Using the measurements from Schödel et al. (2007), we set $r_{break} = 8''$ and $\gamma_2 = 1.8$ (the deprojected values of $R_{break} = 6''$ and $\Gamma = 0.8$, from the surface density measurements using this broken power law model) to constrain the parameters of the outer cluster density profile. We assumed that contamination from young stars is less severe in the region outside of our survey, so using an outer cluster density profile measured from total number counts should introduce only a small bias. For example, the density of bright young stars falls off relatively steeply as

R^{-2} (Paumard et al., 2006; Lu et al., 2009, but see also Buchholz et al. (2009)). To determine the constraints on the physical density profile in the inner region, we performed Monte Carlo simulations of clusters with γ_1 between -2.0 and 2.0. For each value of γ_1, 10^4 realizations were performed. In each realization, 69 stars (the number of late-type stars used to measure the radial profile) were drawn from the broken power law distribution after correcting for the limited area observed in this survey. The locations of these stars were then binned and fitted the same way as the data. We find that for $-2.0 < \gamma_1 < 0.5$, the projected inner radial profiles are flat with $\Gamma \approx 0$ (see Figure 3.14). Figure 3.15 shows the relationship between γ_1 and Γ as determined from the MC simulations. Using this relationship and the observed inner radial profile, $\Gamma = -0.27 \pm 0.16$, we can set an upper limit of 1.0 to the value of γ_1 at the 99.7% confidence level.

Although the slope measurement in this survey cannot constrain whether there is a 'hole' in the distribution of late-type stars or just a very shallow power law within the central $4''$, the inferred slope is significantly flatter than the range of γ_1 between 7/4 and 3/2 predicted by Bahcall & Wolf (1977). In fact, a flat core density profile without a cusp can fit the data equally well. Below, we discuss several plausible dynamical scenarios that may deplete the number density of the late-type giants observed in this study, as well as possible observational prospects for making further progress.

3.6.1 Mass segregation

The true population of dark mass that consists of stellar remnants such as neutron stars or stellar black holes is unknown, but theoretically, there is a strong case for a large population of such remnants due to mass segregation (Morris, 1993). As these dark remnants migrate inward, they will scatter the lighter stars outward.

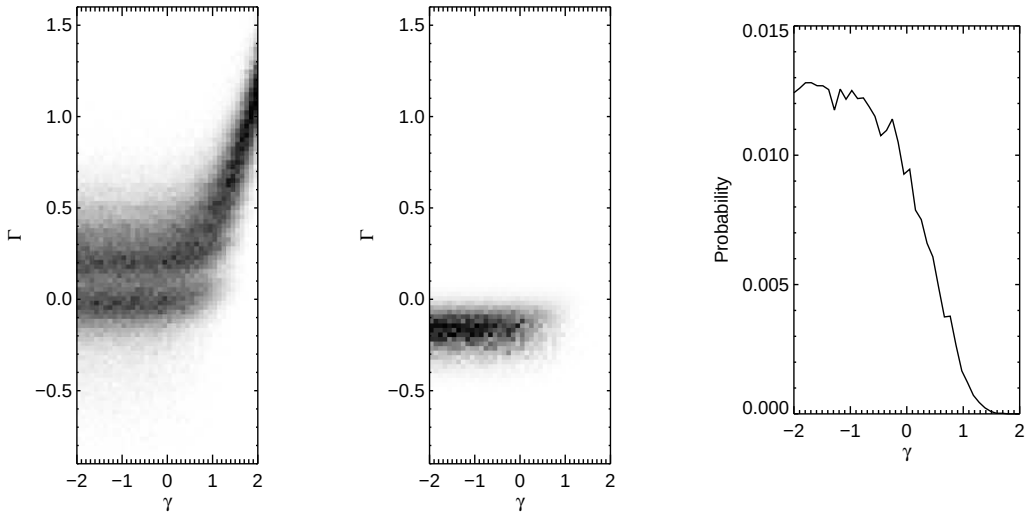

Figure 3.15 Left: the results of the Monte Carlo simulations of different inner radial power laws γ and the resulting measured projected power law of the radial profile, $\Gamma = -0.26 \pm 0.24$. Center: using our measurements, we can constrain some of the parameter space for Γ vs. γ. Right: we marginalize over Γ to determine that our measurement constrains γ to be less than 1.0 at a 99.7% confidence level.

Recent simulations by Alexander & Hopman (2008) showed that a population of ~ 10 $M_\odot$ stellar remnants can sink into a much steeper density distribution ($2 \lesssim \gamma < 11/4$) than the lighter stars ($3/2 < \gamma < 7/2$), if the stellar remnants are relatively rare compared to stars. This results in a very dense cluster of stellar remnants, but the prediction of the stellar cusp from strong mass segregation does not differ substantially from the Bahcall & Wolf (1977) values. Thus, mass segregation cannot be the only mechanism responsible for the inferred lack of a cusp in the evolved red giant population.

3.6.2 Envelope destruction by stellar collisions

The M and K type giants in this survey have radii that vary between 20 to 200 $R_\odot$, which results in substantial cross sections for collisions with other stars in this high density environment (e.g. Bailey & Davies, 1999; Dale et al., 2009). This

may lead to a preferential depletion of red giants toward the center, which would result in a biased measurement of the underlying stellar cusp slope, since most of the surviving stars in the cusp would be unobserved main sequence stars with smaller radii. The depletion of giants has been suggested in the past based upon low spatial resolution spectroscopy of the CO band-head at 2.29 μm (McGinn et al., 1989) as well as in narrow band imaging (Genzel et al., 2003b; Buchholz et al., 2009). Theoretically, a collisionally dominated cusp can be as shallow as $\gamma = 0.5$, which is within the range of slopes allowed by our upper limits, for an isotropic distribution, (i.e., for a distribution function that depends only on energy), although this result no longer holds in the case of a more general distribution function (Murphy et al., 1991). While the collisional destruction of giants can operate efficiently within the region observed in this survey, the effectiveness of this mechanism drops very quickly with distance from the black hole. For example, Dale et al. (2009) found that collisional destruction of giants becomes less likely beyond about 0.1 pc from Sgr A*. While this survey covers a region out to ~ 0.16 pc in projection from Sgr A*, previous observations such as from Buchholz et al. (2009) suggest that the flattening in the late-type giant radial profile extends out even further to ~ 0.24 pc in projection. If the assumptions about the steep distributions of stellar mass black holes and other stellar remnants in the simulations of Dale et al. (2009) are correct, then this would suggest that the collisional destruction of giants is not the dominant mechanism for clearing the cusp of stars. Observational constraints on the effectiveness of this mechanism can be made by comparing the radial density profiles of giants of varying stellar radii. Collisional destruction should preferentially remove stars having larger radii at a given distance from the black hole (see Section 3.6.4 for further discussion).

3.6.3 IMBH or binary black hole

A more dramatic change to the stellar cusp can be achieved through the infall of an IMBH. Baumgardt et al. (2006) performed N body simulations of the effects on the central star cluster with an initial cusp slope of $\gamma = 7/4$ due to the infall of IMBHs of mass 3×10^3 $M_\odot$ and 10^4 $M_\odot$. They find that the IMBH will deplete the cusp of stars, which will cause the inner portion of the cluster to resemble a core profile after the IMBH has spiraled into the central black hole, and that it would take over $\sim$ 100 Myr after the IMBH infall to replenish the stellar cusp. For the case of a 10^4 $M_\odot$ IMBH, the density profile has a flat core, with a core radius of $\sim$ 0.2 pc, which is roughly consistent with that observed in this survey and by Buchholz et al. (2009).

The existence of a binary massive black hole in the Galactic center can also contribute to the loss of stars in this region. A star passing within the orbit of the companion massive black hole will undergo dynamical interactions with the binary, which can result in the star achieving ejection velocity (Merritt & Milosavljević, 2005). In addition, similar to that of an infalling IMBH, a merger with a massive black hole system more recently than the dynamical relaxation time will result in a system that is still out of equilibrium at this time (Merritt et al., 2007).

Current measurements impose only modest limits on the possibility of an infalling IMBH and a binary black hole. Trippe et al. (2008) found no obvious kinematic signatures of a recent infall of an IMBH using 3D velocity measurements of the late-type stars, however, a more complete study of the phase space distribution of the stars will be necessary to ascertain the likelihood of an IMBH clearing the cusp of stars (see Gualandris & Merritt (2009) for a more extensive discussion of current constraints on the existence of an IMBH at the Galactic

center). Current measurements of the reflex motion of the black hole at radio wavelengths place the limit to the mass of a companion black hole at $< 10^4$ $M_\odot$ with semi-major axes 10^3 AU $< a < 10^5$ AU (Reid & Brunthaler, 2004). Precise measurements of the possible reflex motion of the black hole using stellar orbits can provide stronger constraints in the future on the presence of a companion black hole (Ghez et al., 2008).

3.6.4 Prospects for future observations

Given the current state of measurements of the cusp density, it is unclear which, if any, of these dynamical interactions are responsible for the shallow inferred cluster slope. The strong degeneracy between the surface number density and the de-projected volume density makes it difficult to determine the extent of the depletion of red giants within the inner 0.1 pc. Limits to the line of sight distance of these stars from Sgr A* will be necessary to resolve this degeneracy. Within the central arcsecond, it may be possible with direct orbit fits to measure the orbital elements of stars located physically near the black hole. For example, at least one of these late-type stars, S0-17 (which passed within 65 mas of Sgr A* in the plane of the sky in 2007) has an orbit measurement that places its periastron distance closer than 8 mpc (1600 AU) from the black hole (Gillessen et al., 2009). This indicates that while there are fewer late-type stars expected in the central region, it is not entirely devoid of these stars. Even for stars without well-determined orbits, acceleration limits can be used to constrain the 3D distribution of the late-type population, and thus help determine whether there is a 'hole' or simply a flattening of the radial density profile toward the center of the cluster.

Determining which mechanism is responsible for the shallow slope of the late-type stars is important because it is related to whether we can use these stars

as tracers of the underlying stellar cluster. The main sequence, $\gtrsim$ 1 Gyr old stars, represents a significant fraction of both the mass and number density of the stellar cusp, but is currently unobservable spectroscopically; spectral types later than A have $K' > 19$, compared to our current sensitivity limit of 15.5 at K'. Fortunately, in a relaxed population, the red giants should have the same phase space distribution as main sequence stars of comparable mass, so their radial density profile should be identical. However, the red giants have substantially larger radii than the main sequence stars, so they are more likely to be destroyed if collisions are important. It may be possible to observationally constrain whether collisions are the dominant mechanism responsible for the observed slope of the radial density profile by spectral typing the late-type stars more precisely than was possible in this survey. For example, the equivalent width of the CO band head at 2.29 μm, which varies over a wider range than the equivalent width of Na I observed in this study, should permit one to distinguish between individual spectral sub-types. With a factor of $\sim$ 6 change in the radii of red giants between spectral types K3III and M5III (van Belle et al., 1999), a difference in density profile between different spectral types would provide a test of whether collisions affect the distribution of these stars.

3.7 Conclusions

We completed a survey using high angular resolution integral field spectroscopy of the inner $\sim$ 0.16 pc of the Galaxy in order to measure the radial profile of the late-type stars in this region. The survey reached a depth of $K' < 15.5$ and is able to differentiate between early and late-type stars. The survey provided spectral types for 60 early-type and 74 late-type stars, with 22 and 61 previously unreported early and late-type stars, respectively. We find a late-type stellar

surface density power-law exponent $\Gamma = -0.27 \pm 0.19$, which limits the volume number density profile slope γ to be less than 1.0 at the 99.7% confidence level, and even allows for the presence of a central drop in the density of late-type giants. We present three scenarios that may lead to the depletion of late-type stars, but are unable to constrain the candidate mechanism sufficiently to determine which is dominant. Given the current measurements, we cannot yet determine whether the distribution of observed giants is representative of the distribution of stellar mass. Being able to infer the underlying dynamically relaxed stellar population will be crucial in order to establish whether the Galactic center is lacking the type of stellar cusp long predicted by theory. Obtaining an unbiased measurement of the stellar distribution is important because such cusps have considerable impact on the growth of massive black holes as well as on the evolution of nuclear star clusters. Progress in achieving this goal will be possible with improved kinematics and spectral coverage in order to break the degeneracy in the surface number density profile to better establish the three-dimensional distribution of the stellar cluster.

CHAPTER 4

Using kinematics to constrain the distribution of stars at the Galactic center

4.1 Introduction

The degeneracy in the projection from a three-dimensional cluster density profile onto the plane of the sky must be overcome in order to better constrain the theories for the depletion of the stellar cusp. This chapter is intended to set up the framework for including kinematic information to further constrain the limits set by the observed surface density profile. We will discuss two methods: (1) using velocities and accelerations to set limits on the line-of-sight distance on a star-by-star basis, and (2) comparing the velocity distribution of stars with predictions of different cluster models.

In the first method, the degeneracy in measuring the volume density profile is resolved by direct measurements of the line-of-sight distance to each star. The star cluster in the Galactic center has the unique advantage of having very precise kinematic measurements, which with some assumptions about the potential, can be used to derive the line-of-sight distances of the stars, z, from the black hole. I discuss these methods in Section 4.2 and 4.3.

The second method relies on comparing models of the seven-dimensional phase space distribution function ($f(x, y, z, v_x, v_y, v_z, t)$) to make predictions for the

observed velocity distribution. A viable cluster model should reproduce both the density profile and velocity distribution. Constraining the distribution is also useful in constraining physical models that may create a core in the star cluster. Using the assumptions of spherical symmetry, isotropic velocities, and a gravitational potential dominated by the black hole greatly simplifies the form of the distribution function, which limits the range of models to test. More details on this method are provided in Section 4.4.

We will defer comparisons of these kinematic models with data at this time for two reasons: (1) acceleration measurements in the plane of the sky require a stable reference frame and a precise optical distortion solution for the NIRC2 imager. This issue is being addressed in Yelda et al. (in prep), and we expect to be able to use acceleration measurements soon. (2) The three dimensional velocity available from the survey presented in Chapter 3 limited to the flat region of the density profile of the late-type stars. This core extends out to about $6''$ compared to the edge of the current survey at $3''$. Velocity measurements beyond the core region will be necessary to constrain the range of models allowed by the data.

4.2 Limits on line-of-sight distance with velocities

The simplest method of determining the limits to z for each star comes from comparing the total velocity, V_{tot} of the star to the escape velocity at the star's projected distance, R from the black hole. If we assume the major contributor of the potential to be the black hole mass, M_{BH}, and that the stars are gravitationally bound, then:

$$z < \sqrt{\frac{2GM_{BH}}{V_{tot}^2} - R^2} \tag{4.1}$$

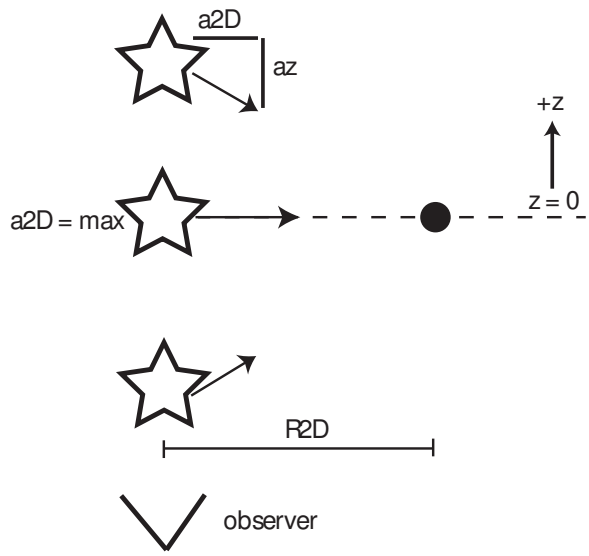

Figure 4.1 A diagram illustrating the acceleration components in the line of sight as well as in the plane of the sky. The acceleration vector points to the black hole. a_{2D} is maximized, while a_z drops to 0 at $z = 0$.

For well-measured high-velocity stars, the limits on z can be quite strict, however, the range of z for low-velocity stars is too large to be useful (in addition if z, is greater than about 1 pc, the sphere of influence of the black hole, a purely Keplerian potential is no longer valid).

4.3 Limits on line-of-sight distance with accelerations

For the stars at the center of the nuclear star cluster, the line-of-sight distance can be measured directly using accelerations. With the assumption that the black hole mass dominates the potential, the true radial distance, r, from the black hole can be simply computed using Newton's law of gravity:

$$a = \frac{GM_{BH}}{r^2} \tag{4.2}$$

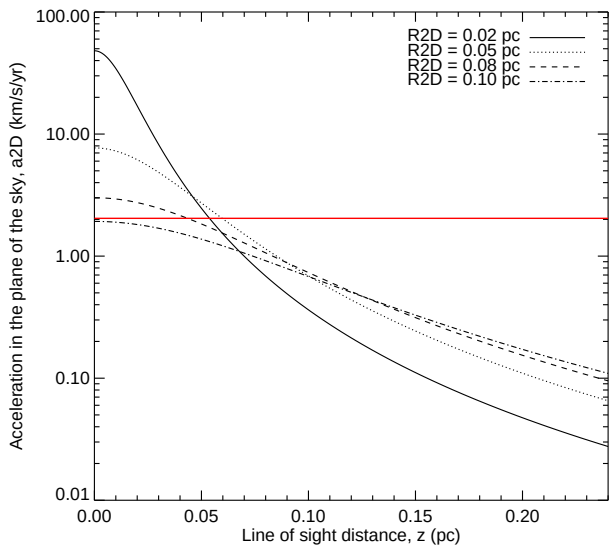

Figure 4.2 The possible values of a_{2D} as a function of z distances are shown for different projected distance R_{2d}. The red line marks the current acceleration measurement precision at 3σ. For any given acceleration uncertainty, there is a range of z values that the measurements are sensitive to, depending on the R_{2D} distance.

where a is the magnitude of the acceleration of the star. This assumes that the acceleration can be measured in both the plane of the sky and along the line-of-sight. It is useful to decompose these two components (see Figure 4.1), because accelerations in the plane of the sky are measured using astrometry and are angular measurements, while the accelerations along the line-of-sight are measured spectroscopically with different measurement uncertainties. The line-of-sight distance, z, can be computed from the plane of the sky acceleration, a_{2D}, using:

$$\begin{aligned} a_{2D} &= -\frac{GM_{BH}}{(R_{2D}^2+z^2)^{3/2}} R_{2D} \\ z &= \left(\left(\frac{GM_{BH}R_{2D}}{a_{2D}}\right)^{2/3} - R_{2D}^2\right)^{1/2} \end{aligned} \tag{4.3}$$

where R_{2D} is the projected distance on the sky.

With the measurements of a_{2D} alone, $\pm z$ is degenerate (the star can be in

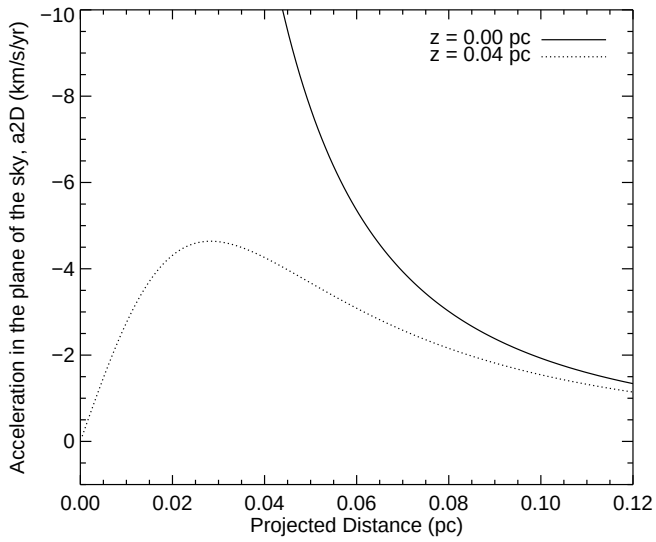

Figure 4.3 The possible values of a_{2D} as a function of R_{2D} distances are shown for different z values. As R_{2D} approaches 0, the expected a_{2D} also falls to zero.

front or behind the black hole), but is not of concern for measuring the radial profile of the number density. More problematic however is that the sensitivity to the line-of-sight distance is dependent on the projected distance, R_{2D}. As R_{2D} approaches 0, the range of detectable z values at a given acceleration uncertainty becomes smaller; the same is true for large values of R_{2D} (see Figures 4.2 and 4.3). There is an intermediate R_{2D} distance which gives the maximum sensitivity in z for a given a_{2D} uncertainty. This behavior is due to the fact that the acceleration vector always points toward the black hole. Figure 4.6 shows this dependence on the range of z values at different R_{2D} distances for a typical astrometric precision.

In contrast, acceleration along the line-of-sight from spectroscopic measurements are more sensitive for stars close to the black hole in the plane of the sky:

$$a_z = -\frac{GM_{BH}}{(R^2+z^2)^{3/2}} z \tag{4.4}$$

However, z is degenerate for measurements of a_z over a range of z. For example,

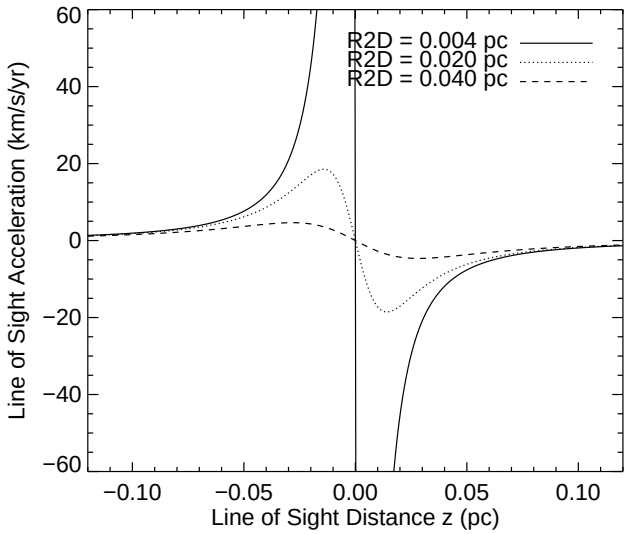

Figure 4.4 The possible values of a_z as a function of z distances are shown for different projected distance R_{2d}. For a given a_z measurement, there is usually a degeneracy in z distance that must be broken by using limits from a_{2D}.

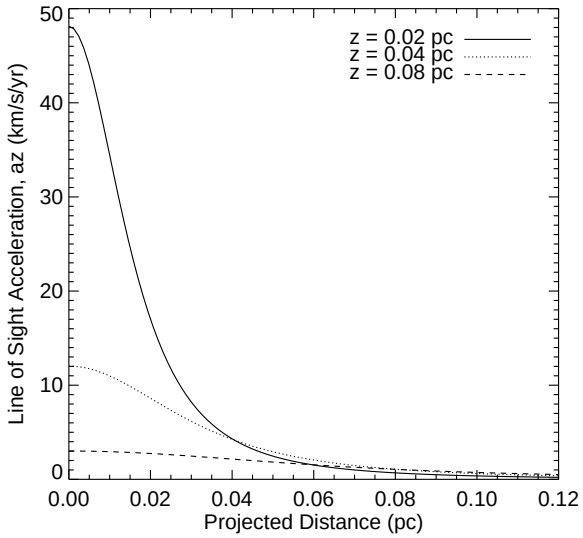

Figure 4.5 The possible values of a_z as a function of R_{2D} distances are shown for different line-of-sight distances z.

if a_z is small, z can be very close to zero, or z can be very large (see Figures 4.4 and 4.5). Limits on a_{2D} are required to break this degeneracy. Figure 4.6 summarizes our sensitivity to z given our average acceleration uncertainties in a_z (9 km/s/yr at 3σ) and a_{2D} (0.051 mas/yr/yr at 3σ). These a_z measurements are based radial velocity measurements from 2006 and 2008, measured using a cross correlation with a template M3III spectrum from the spectral templates from the IRTF (Rayner et al., 2009). We include measurements of stars with continuum SNR > 35, which have velocity errors of about 4 km/s. However, in order to obtain robust acceleration measurements, an additional third epoch is required (measurements from 2009 suffered from calibration problems, which have only recently been resolved). The 3 σ acceleration error in the plane of the sky (a_{2D}) are from values reported in Yelda et al. (2010).

Presently, we should be able to detect all stars within 0.045 pc ($\sim 1.12''$) in volume around Sgr A*. Beyond this volume, we have some sensitivity out to $\sim$ 0.1 pc ($2.5''$). Currently, because we have a longer time baseline of astrometric measurements compared to radial velocities, the z distances of stars are better constrained with a_{2D} than with a_z in the survey region. Acceleration errors should improve in the future with more temporal coverage; by 2014 (5 more years of data beyond the data in this thesis), we predict that we will be able to obtain three dimensional distances out to 0.12 pc ($\sim 2.88''$) from Sgr A*. Further details on the measurements and the three dimensional profile of the cluster will be given in Do et al. (in prep).

4.4 Using velocity distributions

Accelerations could eventually provide unambiguous z distances for the stars, but the distribution of stellar velocities can also be used as an additional constraint

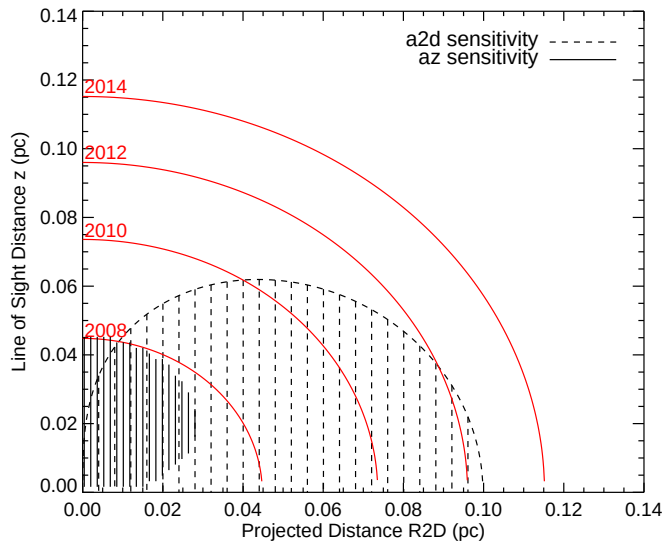

Figure 4.6 The shaded regions correspond to the locations where the typical acceleration uncertainties allow for a significant measurement of z from either the line-of-sight acceleration (a_z, solid lines), or acceleration in the plane of the sky (a_{2D}, dashed). The plot assumes a 3σ error of $a_z = 9$ km/s/s and $a_{2D} = 0.051$ mas/yr/yr. The red lines show the volume of complete coverage in z, from either a_z or a_{2D}, if observations were continued with the same cadence in the future.

to the spatial density profile. Unlike limits on z from acceleration, which depends only on the assumed gravitational potential, the velocity distribution is dependent on the distribution function, which describes the probability of finding a star in a particular position in phase space. The distribution function $f(\boldsymbol{x}, \boldsymbol{v}, t)$ is a function of position, velocity and time, and fully describes the behavior of a stellar system. With some assumptions about the stellar system, we can compare predictions from the distribution function to observable parameters such as the projected density profile and the velocity distributions.

In order to compare to the velocity distribution from observations, we will make several assumptions: (1) the distribution function is time independent; (2) the potential is Keplerian, with $\Psi(r) = GM/r$, which is a reasonable approximation given that we are interested in the region within ~ 0.16 pc in projected distance from the black hole, well inside its sphere of influence; (3) the cluster is spherically symmetric; and (4) the distribution function is isotropic. These assumptions result in a distribution function that is dependent only on the total energy per unit mass, $\varepsilon = \Psi - \frac{1}{2}v^2$ (here, we use the same convention as Binney & Tremaine (2008) of positive ε for bound stars). With the assumption of spherical symmetry and isotropy, it is possible to uniquely invert a given spatial density profile, $\nu(r)$ (and through a change of variable, cast as $\nu(\Psi)$), into a distribution function through the Eddington formula (Binney & Tremaine, 2008):

$$f(\varepsilon) = \frac{1}{\sqrt{8}\pi^2} \frac{d}{d\varepsilon} \int_0^{\varepsilon} \frac{d\Psi}{\sqrt{\varepsilon - \Psi}} \frac{d\nu}{d\Psi}. \tag{4.5}$$

While this inversion is possible, it is simpler to construct a distribution function that is consistent with the observed limits on the slope of the density profile and use the velocity distribution to check the validity of the distribution function. We start by working through some simple models before constructing the distribution

function for an isotropic core.

4.4.1 The Plummer model

The Plummer model is a simple star cluster model that has analytical solutions for a number of dynamical properties, so it is a good choice to illustrate the effect on the velocity distribution from a density profile. The Plummer model potential is a modified Keplerian potential with a softening factor, b, to prevent the potential approaching infinity at the center of the cluster:

$$\Psi = \frac{GM}{(r^2 + b^2)^{1/2}} \tag{4.6}$$

The distribution function of the Plummer model is a special form of the more general distribution function that depends only on a power law of the total energy, $\varepsilon = \Psi - \frac{1}{2}v^2$, where Ψ is the potential, and v is the total velocity (note that $\varepsilon > 0$ for bound orbits):

$$f(\varepsilon) = \begin{cases} C\varepsilon^{n-3/2} & : \quad \varepsilon > 0 \\ 0 & : \quad \varepsilon \leq 0 \end{cases} \tag{4.7}$$

with $n = 5$ for the Plummer model. The density profile ν at radii where $\Psi > 0$ can be found by integrating the distribution function over all velocities:

$$\nu(\boldsymbol{x}) = \int d^3\boldsymbol{v} f(\boldsymbol{x}, \boldsymbol{v}) \tag{4.8}$$

$$\nu(r) = 4\pi \int_0^{\sqrt{2\Psi}} dv v^2 f(\Psi - \frac{1}{2}v^2) \tag{4.9}$$

$$= 4\pi C \int_0^{\sqrt{2\Psi}} dv v^2 (\Psi - \frac{1}{2}v^2)^{n-3/2} \tag{4.10}$$

The limits of the integral range between zero and the escape velocity at r. This equation can be simplified by using the trigonometric substitution $v^2 = 2\Psi\cos^2\theta$. The solution becomes:

$$\nu = c_n \Psi^n, \text{for } \Psi > 0, \text{where } c_n = \frac{(2\pi)^{3/2}(n-\frac{3}{2})!C}{n!} \tag{4.11}$$

for c_n to be finite, $n > 1/2$. For the Plummer model, $\nu(r) \propto 1/(r^2+b^2)^{5/2}$. With the distribution function and the potential, the velocity distribution as well as its moments can be computed. The probability density of total velocities at a projected distance R from the black hole can be computed by integrating along the line-of-sight:

$$F(R,v) = \frac{\int dz f(\boldsymbol{x},\boldsymbol{v})}{\int dz d^3\boldsymbol{v} f(\boldsymbol{x},\boldsymbol{v})} \tag{4.12}$$

$$= \frac{\displaystyle\int \frac{rdr}{\sqrt{r^2-R^2}} f(\varepsilon)}{\Sigma(R)} \tag{4.13}$$

$$\Sigma(R)F(R,v) = \int_0^{\sqrt{\frac{4}{v^4}-1}} \frac{rdr}{\sqrt{r^2-R^2}} (\Psi(r) - \frac{1}{2}v^2)^{7/2} \tag{4.14}$$

with the substitution $dz = rdr/\sqrt{r^2-R^2}$ and the projected density profile:

$$\Sigma(R) = \int dz d^3\boldsymbol{v} f(\boldsymbol{x},\boldsymbol{v}) = \int_R^\infty \frac{rdr}{\sqrt{r^2-R^2}} \nu(r) \tag{4.15}$$

$$= \int_R^\infty \frac{rdr}{\sqrt{r^2-R^2}} \Psi(r)^5 \propto \frac{1}{(1+R^2)^2}.$$

Figure 4.7 shows a plot of $F(R,v)$ for the center of the cluster as well as a scaled projected radius $R = 2$. Note that the width of the distribution is smaller at $R = 2$, consistent with being further from the center of the potential.

The line-of-sight velocity distribution, v_z, can be computed by integrating over

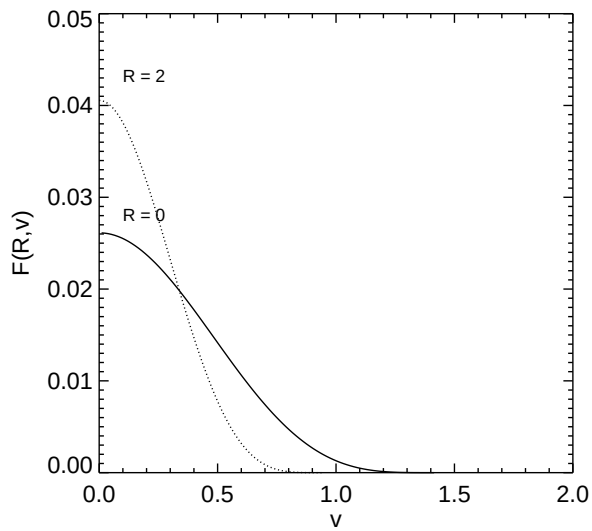

Figure 4.7 $F(R, v)$ for the Plummer Model at the center of the cluster (R=0, solid) and at a dimensionless projected distance of 2 (twice the value of $b = 1$ in this case).

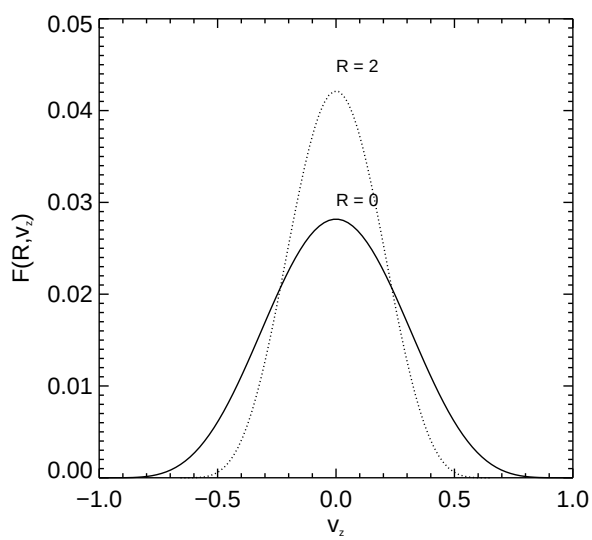

Figure 4.8 Velocity profile along the line-of-sight, $F(R, v_z)$, for the Plummer Model at the center of the cluster (R=0, solid) and at a dimensionless projected distance of 2 (twice the value of $b = 1$ in this case).

the plane-of-sky velocity components – v_R, the velocity in the radial direction, and v_T, the transverse velocity in the plane of the sky:

$$\begin{aligned} F(R, v_z)dv_z &= \int dz \int d^2v_\perp f(\varepsilon) \\ &= \int \frac{rdr}{\sqrt{r^2 - R^2}} \int dv_T dv_R f(\Psi - \frac{1}{2}v^2) \\ &= \int \frac{rdr}{\sqrt{r^2 - R^2}} \int_0^{v_{TMax}} dv_T \int_0^{v_{RMax}} dv_R (\Psi - \frac{1}{2}(v_R^2 + v_T^2 + v_z^2))^{7/2} \\ &= \frac{\pi}{144\sqrt{2}} \int_0^{\sqrt{2\Psi(r)}} \frac{rdr}{\sqrt{r^2 - R^2}} (2\Psi(r) - v_z^2)^{9/2}, \end{aligned} \tag{4.16}$$

where $v_{RMax} = \sqrt{2\Psi - v_z^2 - v_T^2}$ and $v_{TMax} = \sqrt{2\Psi - v_z^2}$. Figure 4.8 shows the probability density $F(R, v_z)$.

The velocity distribution require numerical integration to derive the profile, however, the moments of the velocity, such as the mean and variance, are analytical:

$$\bar{\boldsymbol{v}}(r) = \frac{1}{\nu(r)} \int d^3\boldsymbol{v}\boldsymbol{v} f(\Psi - \frac{1}{2}v^2) = 0 \tag{4.17}$$

$$\sigma^2(r) = \frac{1}{\nu(r)} \int d^3\boldsymbol{v}(v - \bar{v})^2 f(\Psi - \frac{1}{2}v^2) \tag{4.18}$$

$$\sigma^2(r) \propto \frac{1}{\sqrt{1 + r^2}} \tag{4.19}$$

4.4.2 Power law density profiles

The Plummer model is a self-consistent model where the potential is generated by the tracer population (stars) such that, with Poisson's equation ($\nabla^2\Psi = 4\pi G\rho$), the density $\rho(r)$ corresponds to the Plummer potential. This self-consistency is not necessarily required to compute the distribution function if we know the

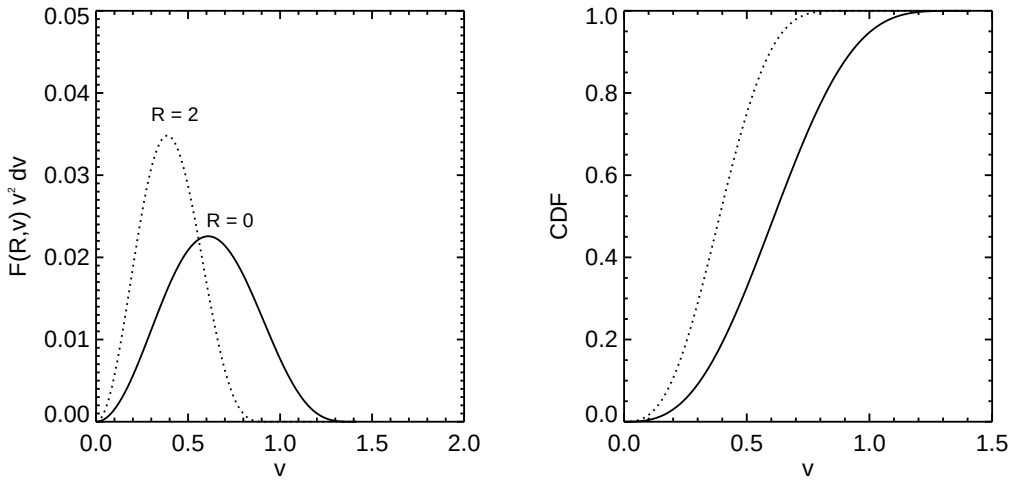

Figure 4.9 Left: The probability that a star is observed with a velocity between v and $v+dv$ for the Plummer model. Right: The probability that a star is observed with a velocity less than v.

potential and the density profile. For an isotropic, spherically symmetric system, a density profile can be inverted with knowledge of the potential to obtain a unique distribution function through Equation 4.5. For power a law number density profile, $\nu(r)$, with a power law slope γ in a Keplerian potential $\Psi = GM/r$:

$$\nu(r) = \nu_o r^{-\gamma}, \tag{4.20}$$

the corresponding distribution function is:

$$f(\varepsilon) = \varepsilon^{\gamma - \frac{3}{2}} \tag{4.21}$$

Using $\gamma = 7/4$, the Bahcall-Wolf cusp slope, as an example, we can derive the expected velocity distributions using the same procedures as for the Plummer

model:

$$f(\varepsilon) = \varepsilon^{1/4} \tag{4.22}$$

$$\Sigma(R)F(R,v) = \int dz f(\varepsilon) = \int_R^{2/v^2} \frac{rdr}{\sqrt{r^2-R^2}}(\frac{1}{r}-\frac{1}{2}v^2)^{1/4} \tag{4.23}$$

where we have substituted $\Psi = 1/r$ and with the surface density profile:

$$\Sigma(R) = \int_R^\infty \frac{rdr}{\sqrt{r^2-R^2}}\nu(r) \tag{4.24}$$

$$= \int_R^\infty \frac{rdr}{\sqrt{r^2-R^2}} r^{-7/4} = -\frac{4\pi\Gamma(3/8)}{\Gamma(-1/8)}R^{-3/4} \tag{4.25}$$

The integral for $\Sigma(r)F(R,v)$ diverges when $v = 0$, but this is not a problem as there is negligible phase space available at $v = 0$. This can be seen when we compute, $P(< v)$ the probability that a star is found with velocity less than v:

$$P(R,<v) = \int_0^v F(R,v)d^3\boldsymbol{v} = 4\pi \int_0^v v^2 dv F(R,v) \tag{4.26}$$

Both $P(R,<v)$ and the integrand are plotted in Figure 4.9 and Figure 4.10 for the Plummer model and the cusp model, respectively. $P(R,<v)$ is essentially the cumulative distribution function for the total velocity, and can be used to compare directly with the observations. Furthermore, since we assumed spherical symmetry in the system, we can compare the velocity distributions taken in annuli around the cluster center:

$$P(R_1 < R < R_2, < v) = 2\pi \int_{R_1}^{R_2} RdR \int_0^v v^2 dv F(R,v) \tag{4.27}$$

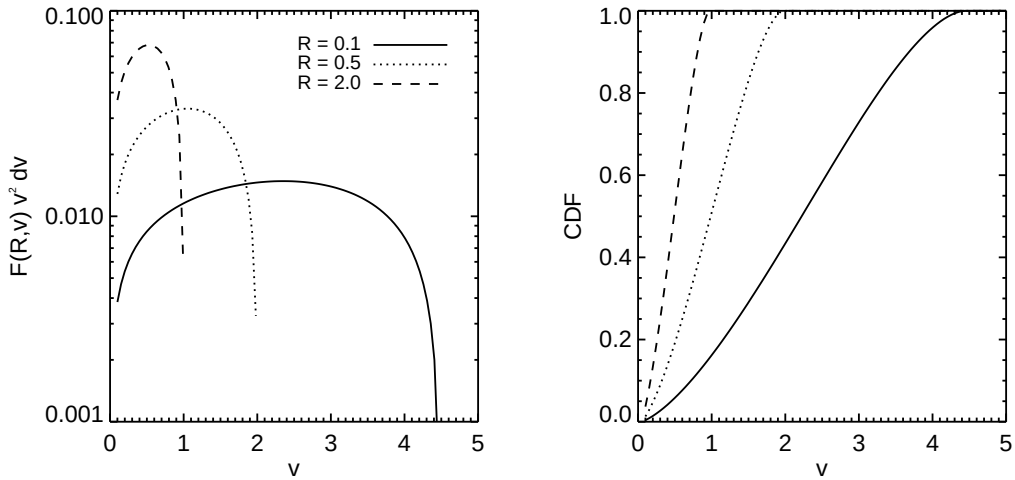

Figure 4.10 Left: The probability that a star is observed with a velocity between v and $v + dv$ for the Bahcall and Wolf stellar cusp model with $\gamma = 7/4$. Right: The probability that a star is observed with a velocity less than v.

4.4.3 An isotropic core model

Based on the limits set by the surface density profile of stars in the Galactic center, the Bahcall and Wolf cusp of $\gamma = 7/4$ is ruled out, so we need to find a distribution function that will produce a flatter core. Since we are working with distribution functions that only depend on energy, we can try a model where certain energies are excluded. Following Merritt (2010), we will remove the most bound stars from the star cluster by introducing an energy cutoff in the power-law form of $f(\varepsilon)$:

$$f(\varepsilon) = \begin{cases} \varepsilon^{\gamma-3/2} & : \quad \varepsilon > 0 \\ 0 & : \quad \varepsilon \leq 0 \\ 0 & : \quad \varepsilon \geq E_b \end{cases} \tag{4.28}$$

where, E_b is the binding energy at the radius r_b, such that $E_b = \Psi_b$. For the purpose of this model, we will set $\gamma = 7/4$, which is very close to the value of $\gamma = 1.8$ found from number counts outside the region where the density profile

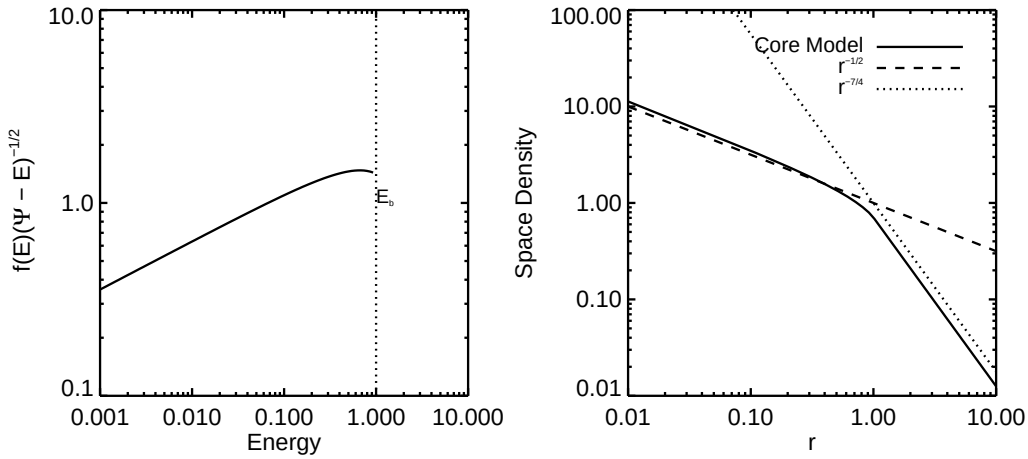

Figure 4.11 Left: The integrand for $\nu(r)$ showing the energy cutoff at ε_b. Right: The resulting density profile is more shallow than the Bahcall and Wolf solution at $r < r_b$, and is within the range allowed by observations.

is flat (Schödel et al., 2007). At $r \geq r_b$, the spatial density profile is as before, $\nu(r) \propto r^{7/4}$. For $r < r_b$:

$$\nu(r) = 4\pi \int f(\varepsilon) v^2 dv \tag{4.29}$$

$$= 4\pi \int_0^{\Psi_b} \sqrt{2(\Psi - \varepsilon)} f(\varepsilon) d\varepsilon \tag{4.30}$$

The full density profile can be computed through numerical integration (see Figure 4.11). For $r \ll r_b$, the density approaches $\nu(r) \propto r^{-1/2}$, which indicates that removing highly bound stars has flatten the number density profile, but has not removed all stars or created a central minimum.

Similarly, we can compute $F(R, v)$ and $P(R, < v)$ using the Keplerian potential $\Psi(r) = GM/r$:

$$F(R, v) = \int_{r_{min}}^{r_{max}} \frac{r dr}{\sqrt{r^2 - R^2}} f(\Psi(r) - \frac{1}{2} v^2) \tag{4.31}$$

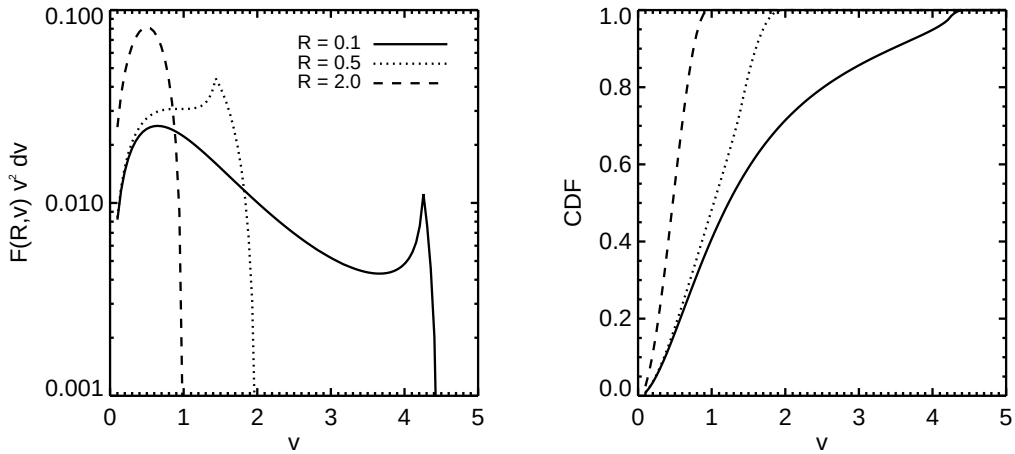

Figure 4.12 Left: The probability that a star is observed with a velocity between v and $v + dv$ for the isotropic core model. Note that beyond $R_b = 1.0$, the probability density is identical to the cusp model in Figure 4.10. Right: The probability that a star is observed with a velocity less than v.

where $r_{min} = \min(R, \frac{1}{1/r_b + v^2/2})$ and $r_{max} = 2/v^2$. There is a minimum radius for each velocity because we removed the most bound stars. This also indicates why there are stars in the region $r < r_b$, since the distribution has a cutoff only in energy. Both $F(R, v)$ and $P(R, < v)$ must be computed numerically. Their distributions are shown in Figure 4.12. These probability distributions for velocities have a very different shape than the purely power law model in Figure 4.10 for $R < r_b$ due to the removal of a range of possible velocities. This comparison indicates that there are notable differences in the shape and mean of the distribution of total velocities as a function of R between models with different density profiles. We note that none of these velocity distributions correspond to a Maxwell-Boltzmann distribution despite the fact that the models are isotropic.

4.4.4 Beyond isotropic models

Because isotropic models with power law density profiles cannot have a power law slope $\gamma < 1/2$ (An & Evans, 2006), we would need to construct anisotropic distribution functions in order to create the presence of a 'hole' in the stellar density profile. For a spherically symmetric system, anisotropy can be included in the distribution function by the inclusion of the angular momentum, L. The inclusion of angular momentum means that there is no longer a unique inversion between $\nu(r)$ and $f(\varepsilon, L)$. Computing the velocity distribution of anisotropic core models is out of the scope of this thesis, but we will briefly describe a method suggested by Merritt (2010); the distribution function of the isotropic core model can be modified to include an angular momentum, J, cutoff: $f(\varepsilon, L) = 0$ for $J \leq J_b$. This model would remove all stars that come within r_b of the black hole, clearing out the central region of the cluster.

4.5 Conclusion

We have shown that the addition of kinematic information should improve the constraints on the true distribution of stars in the region around Sgr A*. For stars with significant acceleration detections, we will be able to constrain their distribution directly. In addition, the three-dimensional velocity measurements of all stars should help us constrain the distribution function of the cluster. We have shown that the predicted velocity distributions are distinctive enough that comparisons with data should rule out certain distribution functions. Some challenges in these comparisons to observations may arise from the assumptions placed on the models. For example, the use of a Keplerian potential is only valid within the sphere of influence of the black hole ($r_s \approx 1$ pc for Sgr A*). While the stars

observed in this thesis are well within r_s in the plane of the sky, if a large number of stars have z distances greater than r_s, then the stellar mass distribution will be important to consider in the models. Ultimately, if we can observationally differentiate between the possible physical scenarios that result in a flattened core (details in Chapter 3), we will learn a great deal about the dynamical history of the environment around a massive black hole.

CHAPTER 5

Conclusions

The advent of laser guide star adaptive optics has rapidly increased our understanding of the environment around a supermassive black hole. It is now possible to study the physical properties of the black hole and its associated accretion flow through its variability in the infrared. Using multiple observations and applying a statistical analysis of the data, we have been able to set new limits on the presence of periodic phenomena responsible for its infrared variability. In particular, it appears unlikely that the large amplitude variability is caused by hot spots of plasma orbiting at the last stable orbit around the black hole; the 'flickering' is much more consistent with the variability observed at the centers of active galaxies, which suggests that some of the same physical processes are occurring in the accretion flow of Sgr A* though on a much smaller scale.

LGS AO has also allowed high angular resolution integral field spectroscopy of this region, resulting in the most detailed population census performed within $\sim$ 0.16 pc of a supermassive black hole. For the first time, we are able to investigate the predictions of a stellar cusp around massive black holes; contrary to these predictions, we find that the old stars have a flat surface density profile close to the black hole. The physical explanation for this puzzling result will affect theories on the growth of the supermassive black hole as well as on the dynamical evolution of other objects in this region.

5.1 Prospects for clarifying the nature of Sgr A*-IR

While we have shown that the near-IR light curves from Sgr A* are consistent with red noise, it is difficult at this time to determine its precise physical origins. The behavior of the Sgr A* light curves are very similar to those seen in AGNs, whose variability has been suggested to arise from instabilities in the accretion flow to changes in the accretion rate. Recently, further evidence of the link between the Sgr A*-IR variability and AGNs was found with the observation of a break frequency in the power law spectrum of Sgr A*. Using near-IR light curves observed from Sgr A* on a scale of minutes up to years apart, Meyer et al. (2009) found a break frequency at 154^{+124}_{-87} minutes, consistent with the relationship between the break frequency of the power spectrum and black hole mass for AGNs observed at X-ray wavelengths (McHardy et al., 2006).

Further insights into the nature of accretion onto Sgr A* can be gained using our current technology with observations of: (1) light curves at faster time sampling, (2) the properties of the faint states of Sgr A*, and (3) the time dependent polarization. The study of Sgr A* at fast time sampling will provide us a unique window into the properties of accretion flow around black holes. While we have been able to constrain the the break frequency of Sgr A* at low frequencies, we have not observed a corresponding break at high frequencies, which may indicate the size scale of structures in the accretion flow. The power spectra of the light curves appear to have a consistent power law slope down to a time scale of ~ 3 min, where the dithering pattern in our data causes a large artifact. To better sample the fast time scales, we can use NIRC2 in its subarray mode to achieve a cadence of 20 s, which corresponds a light travel time of only 0.5 Schwarzschild radii, given the mass of Sgr A*. In this way, we can achieve Nyquist sampling of structures on the order of a Schwarzschild radius. In comparison, the fastest

timescale probed so far for any black hole is on the order of milliseconds for X-ray binaries (Gierliński & Zdziarski, 2003), which corresponds to about 10-20 Schwarzschild radii for a stellar mass black hole. In addition, the nature of the faint state of Sgr A* is important to establish whether there is a distinct quiescent state of Sgr A* and to measure the fraction of light produced by faint unresolved stars as opposed to accretion onto the black hole. Polarization will also offer a new window onto the physics of the accretion flow, and has been suggested to show stronger periodic behavior than the total intensity (e.g. Zamaninasab et al., 2010).

5.2 Origin of the missing stellar cusp

Given the current limits on the stellar density at the Galactic center, we can rule out the density profile in the equilibrium solution from Bahcall & Wolf (1977) for the tracer population of red giants. It is crucial to understand the tracer population as well as the dynamics in this region to properly interpret this result. In principle, the red giants should have had > 1 Gyr to achieve a dynamically relaxed state and should be a good tracer of the underlying stellar distribution. However, since the nuclear star cluster is not an isolated system, dynamical interactions involving objects such as an intermediate mass black hole would change the distribution of stars. In addition, the larger physical size of the red giants compared to main sequence stars may be a factor in increasing the frequency of collisions as well as increasing their cross section for tidal disruption by Sgr A*. More theoretical work with simulations will be required to produce testable predictions of the current configuration of stars in order to compare to observations. In terms of observations, the most important task will be to break the degeneracy in the surface density profile to determine if the volume density

is flat or falls in the core. Kinematic measurements as well as extending the radial coverage beyond the current survey should greatly reduce this degeneracy. Finally, the effect of the size of the red giants can be tested with better spectral typing to determine if there is a difference in the density profiles of giants of different sizes.

APPENDIX A

OSIRIS wavelength calibrations

Every spectrograph requires wavelength calibration in order to transform flux measurement at each pixel of the detector into flux as a function of wavelength. OSIRIS, being an integral field spectrograph, simultaneously measures a spectrum at every spatial pixel location for up to ~ 3000 spectra, all of which must be calibrated. The initial calibration is achieved using an arc lamp at the telescope that scans across all the lenslets (see the OSIRIS User Manual). This calibration is done by the instrument team when major changes to the instrument occur, and is built into the data reduction pipeline.

In 2007, it was discovered that the spectra from different spatial locations in an OSIRIS cube were offset by an average of about 0.1 spectral channel, with maximum offsets up to 0.5 spectral channels on the edges of the Kn3 filter (each spectral channel is 2.5 Å). In the following sections I describe the diagnostics of these wavelength shifts as well as the subsequent correction and stability of the wavelength solution.

A.1 Characterizing the wavelength shifts

The wavelength shifts between different spatial pixels were determined using sky observations. The near-infrared sky has strong OH emission lines, which can be used to test the absolute wavelength calibration (the conversion into Å) as well

as relative offsets between spectra at different spatial locations. Of the OH lines observable in the Kn3 filter ($\lambda = 2.121 - 2.229$ μm), there are 5 strong lines that are not blended with neighboring lines (see Table A.1). In order to determine the effectiveness of the wavelength calibration, I fitted the centroids of these lines with a Gaussian in the spectrum for each spatial pixel in the data cube. Each spectrum was extracted as the median of the neighboring 3×3 spatial pixel at each wavelength channel in order to avoid cosmic rays and bad pixels. I then used the mean difference between the measured wavelengths of the centroids and its corresponding vacuum wavelength to be the average wavelength shift for that spatial pixel. In order to determine whether there is a wavelength dependence to the OH line offsets, I also performed a linear fit to the wavelength difference as a function of wavelength. I find that the linear fit is flat, and not significantly better than using a constant mean to describe the wavelength offsets from vacuum in the Kn3 wavelength range. The mean wavelength offset range from -0.22 Å(3 km/s at 2.1661 μm), with a $\sigma = 0.08$ Å in 2006 to -0.41 Å(5.7 km/s at 2.1661 μm) with $\sigma = 0.09$ Å in 2008.

Table A.1 OH lines used for refining the wavelength calibration in the Kn3 filter

OH Line (Å)
21507.3
21537.6
21802.2
21955.6
22125.5

In addition to using the OH lines as tests of the absolute wavelength calibration, I also measured the relative wavelength solution between each lenslet. Theoretically, after wavelength calibration, the spectrum from every lenslet should have been interpolated onto the same wavelength at each spectral channel. Hav-

ing all the spectra with flux correctly assigned to the same grid of spectral channels is essential to be able to combine the flux from different spatial locations to establish higher signal to noise spectra. Mismatches in the relative wavelength calibration between spaxels can lead to incorrectly measured line widths and centroids when using extraction apertures greater than 1 spaxel in size. In addition, a large offset in the wavelength solution between each lenslet will lead to very poor sky subtraction if the sky is obtained at a different lenslet location, such as for the Galactic center observations. Sufficiently mismatched spectra are apparent in the residual from subtracting skies from two different spatial locations, resulting in small P-Cygni profiles from shifted OH lines.

In order to establish the relative shifts between the spectra from each lenslet, I cross-correlated each spectrum with the one extracted from the central lenslet. In order to avoid bad pixels, the spectrum from each lenslet is the median of a 3x3 box centered on the lenslet of interest (within a 3x3 box, the relative shifts between the spectra do not appear significant).

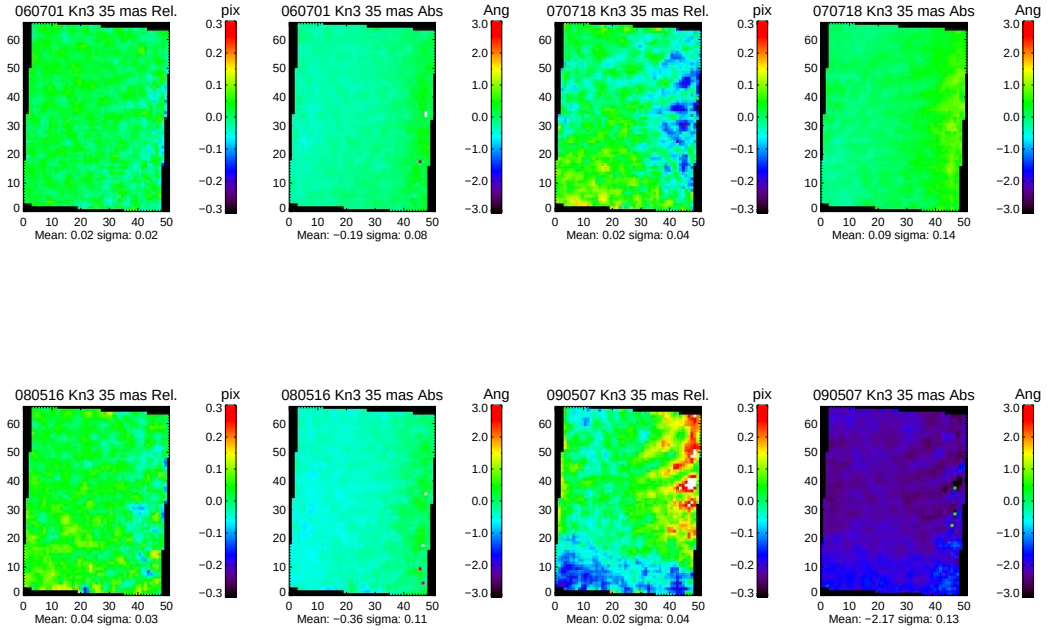

Figure A.1 Both relative and absolute wavelength shifts as measured from the OH lines from 2006-2009. Note that in 2009, the wavelength solution is shifted by about 2 Å compared to previous years due to thermal problems with the spectrograph.

APPENDIX B

Catalog of OSIRIS spectra

Figure B.1 shows the compilation of spectra that were spectral-typed as young based on the presence of Br gamma in the Kn3 wavelength range, while Figure B.11 shows early-type spectra without Br gamma absorption lines. Figure B.15 shows the spectral of all identified late-type stars. These spectra were extracted using the standard 2 pixel radius aperture, with sky subtraction from the median of an annulus starting at 2 pixels out to 4 pixels. These spectra have also been corrected for telluric features and smoothed using a 3 pixel box-car convolution, and are grouped by OSIRIS field locations. More information about each of the spectra can be found in Tables 3.2 and 3.3. Spectra of the IRS16 sources have not been included due to difficulties in determining the radial velocity of the Wolf-Rayet stars (the hydrogen emission lines from the stellar winds obscures the true radial velocity of the spectra).

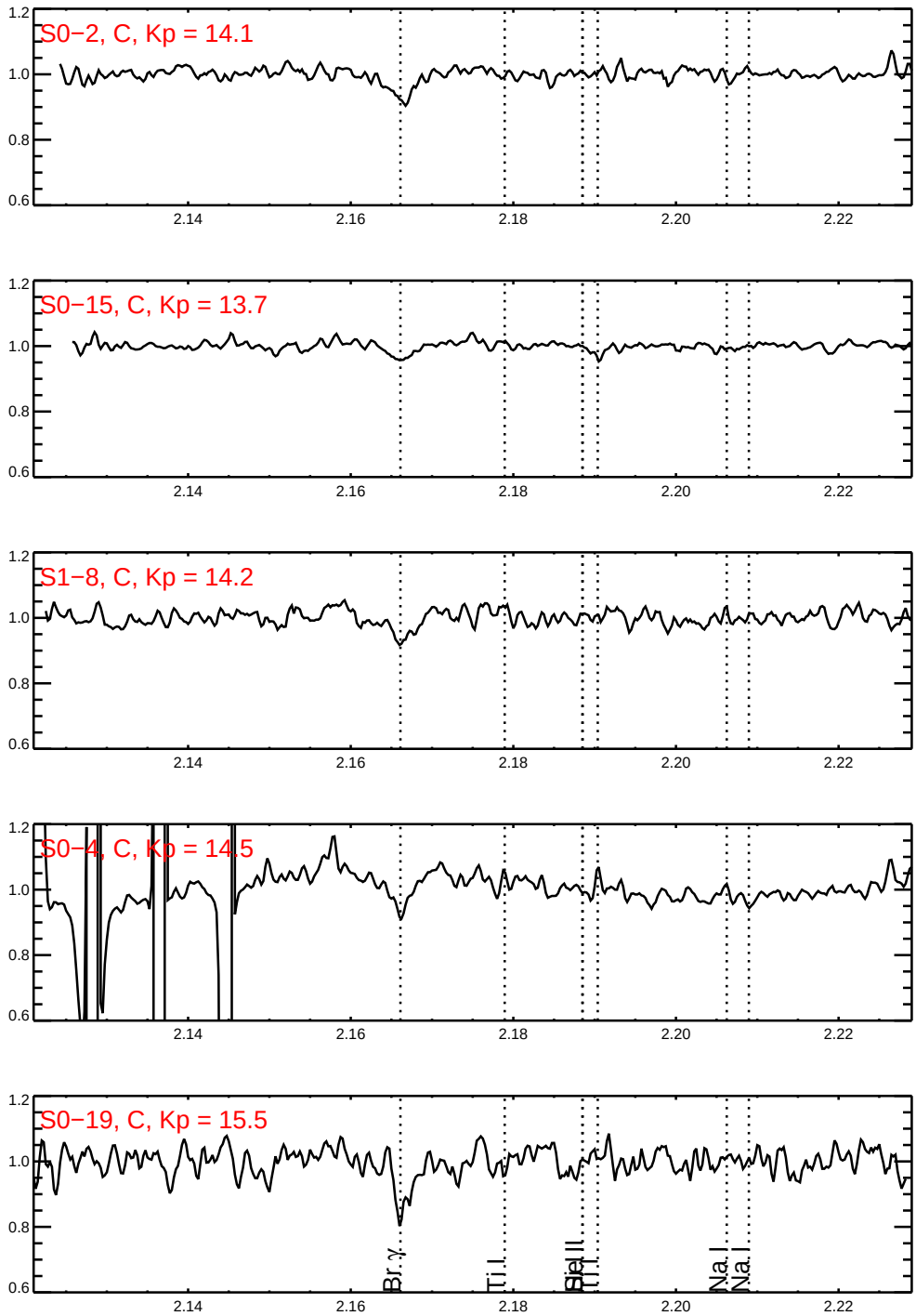

Figure B.1 Early-type stars with Br gamma lines in Kn3, shifted to rest wavelength and grouped by OSIRIS field location.

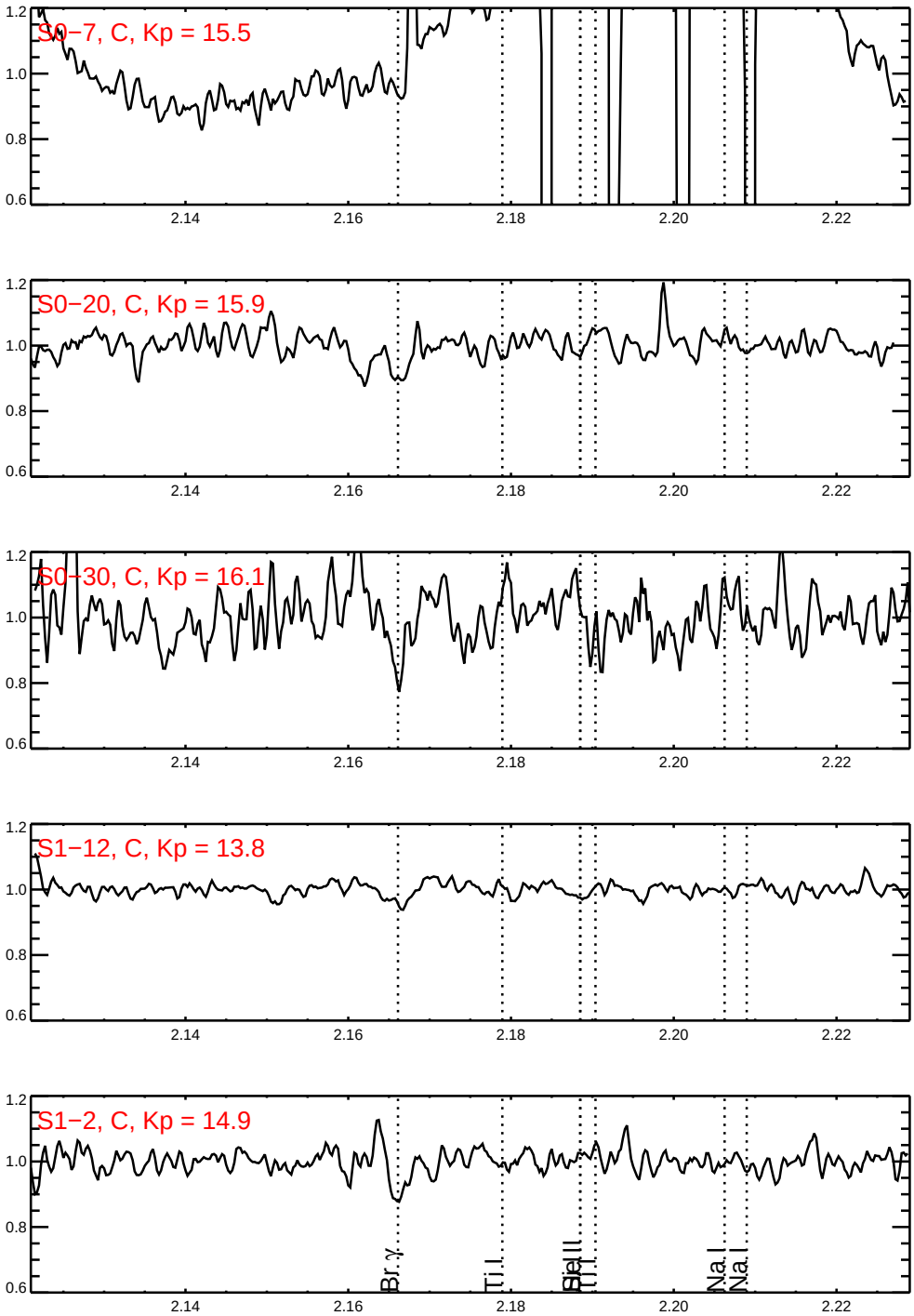

Figure B.2 Continuation of Figure B.1

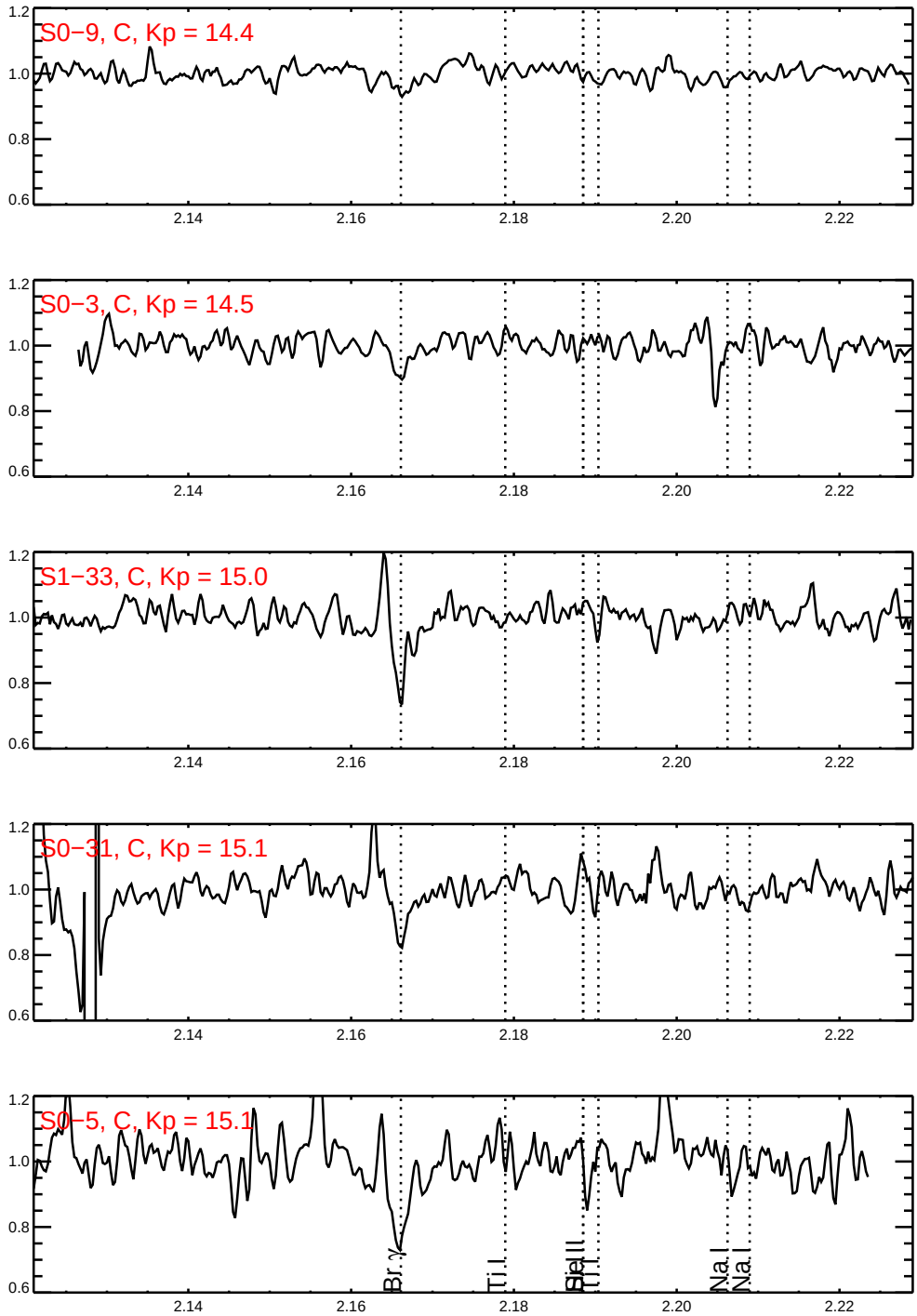

Figure B.3 Continuation of Figure B.1

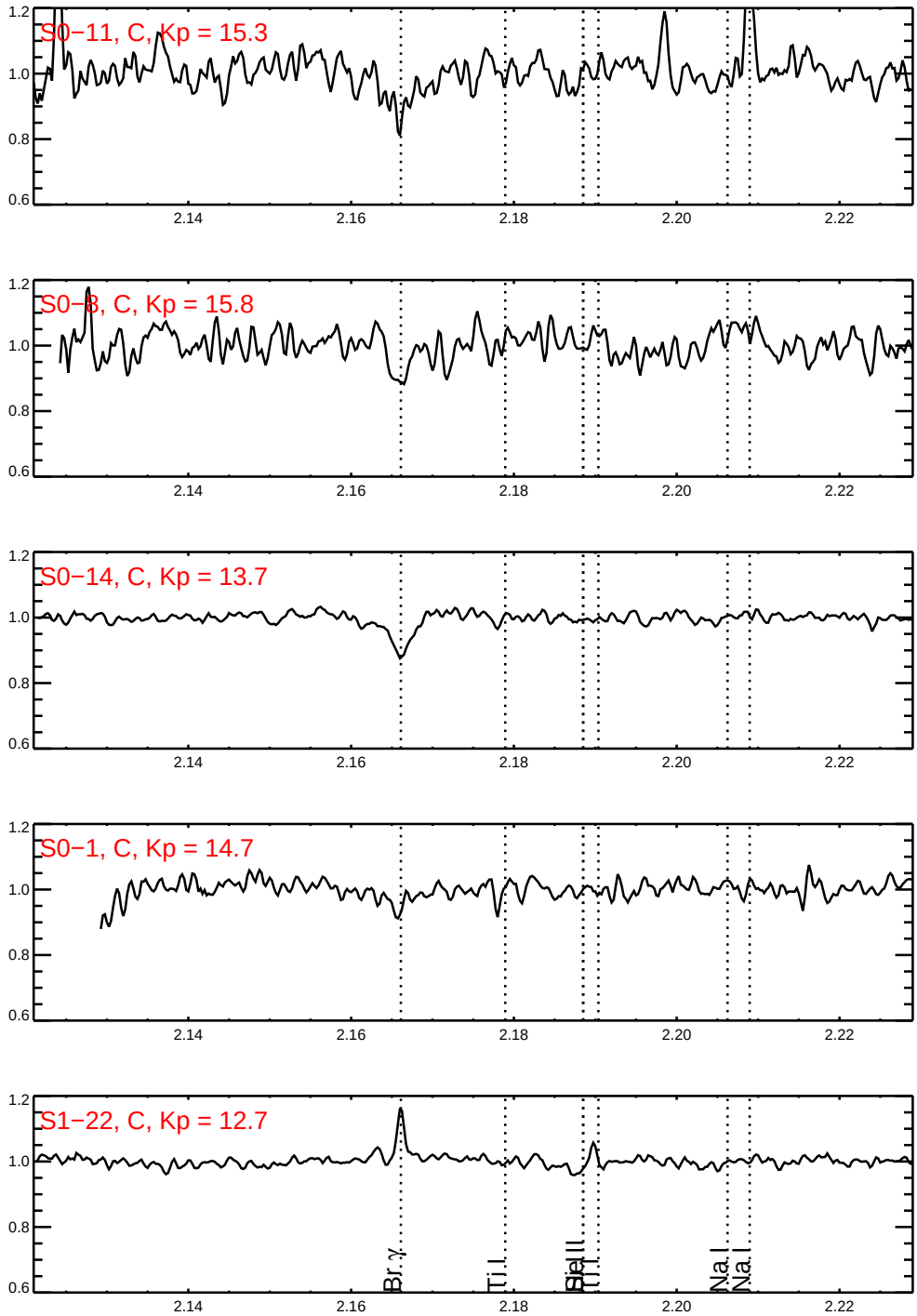

Figure B.4 Continuation of Figure B.1

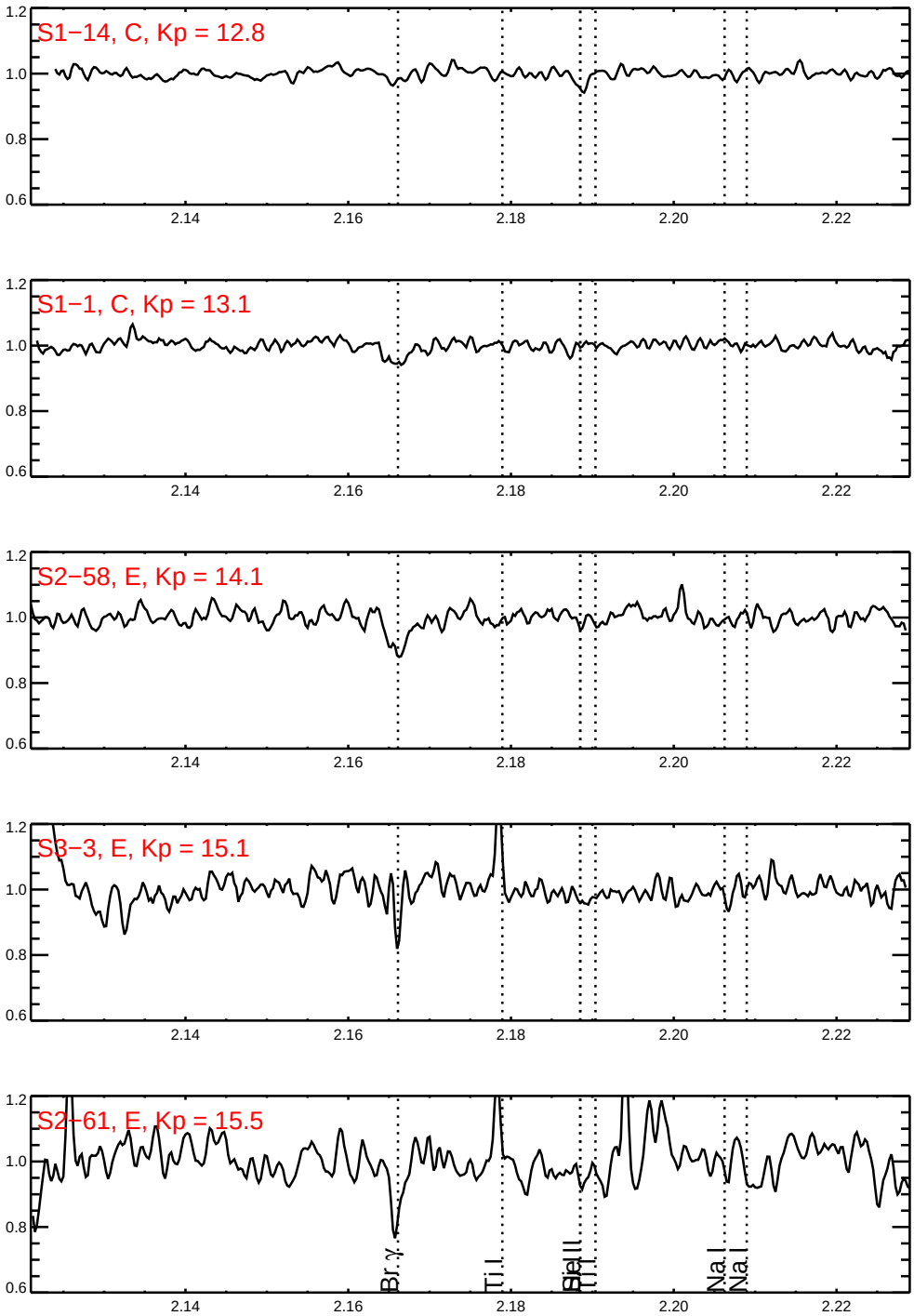

Figure B.5 Continuation of Figure B.1

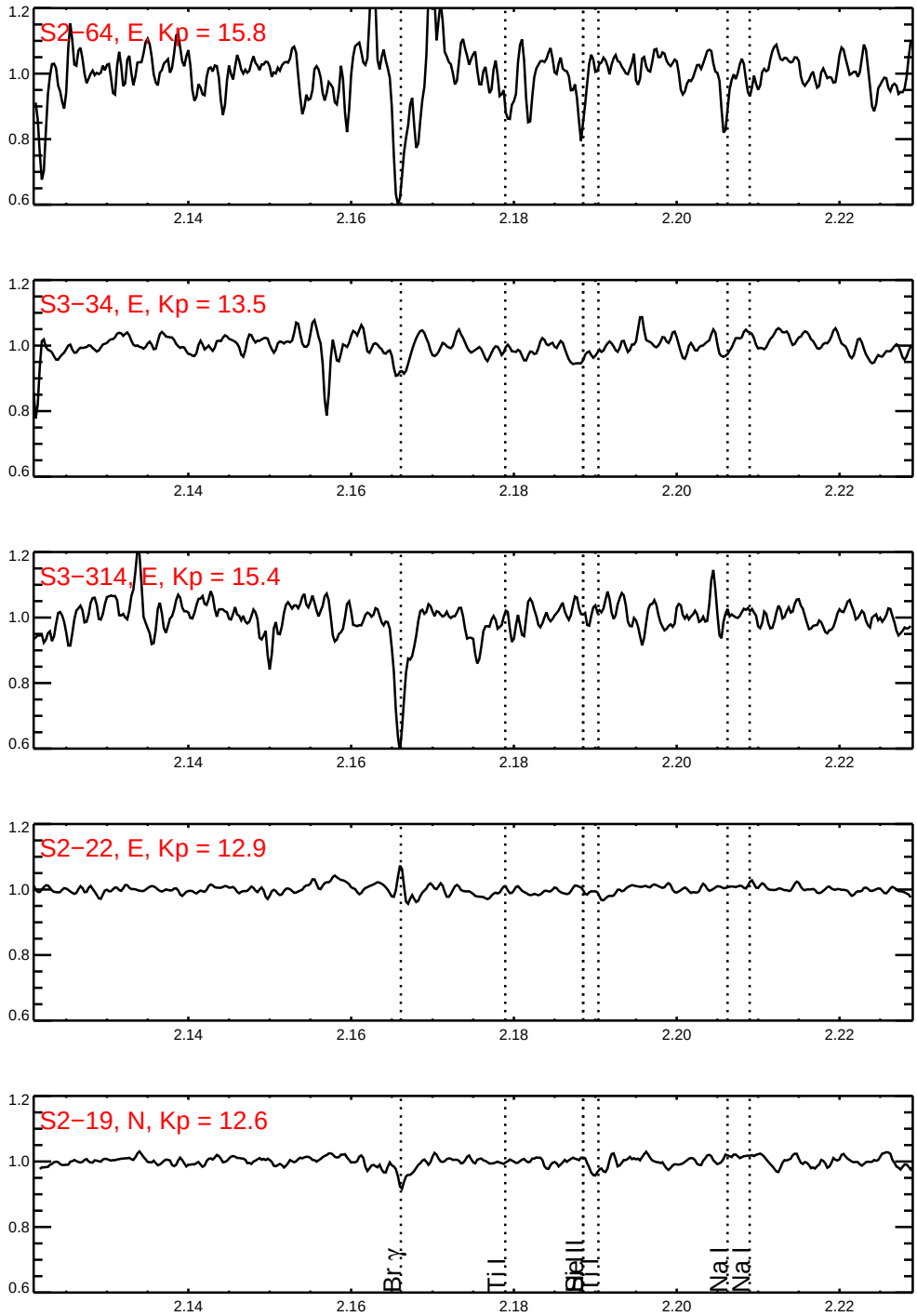

Figure B.6 Continuation of Figure B.1

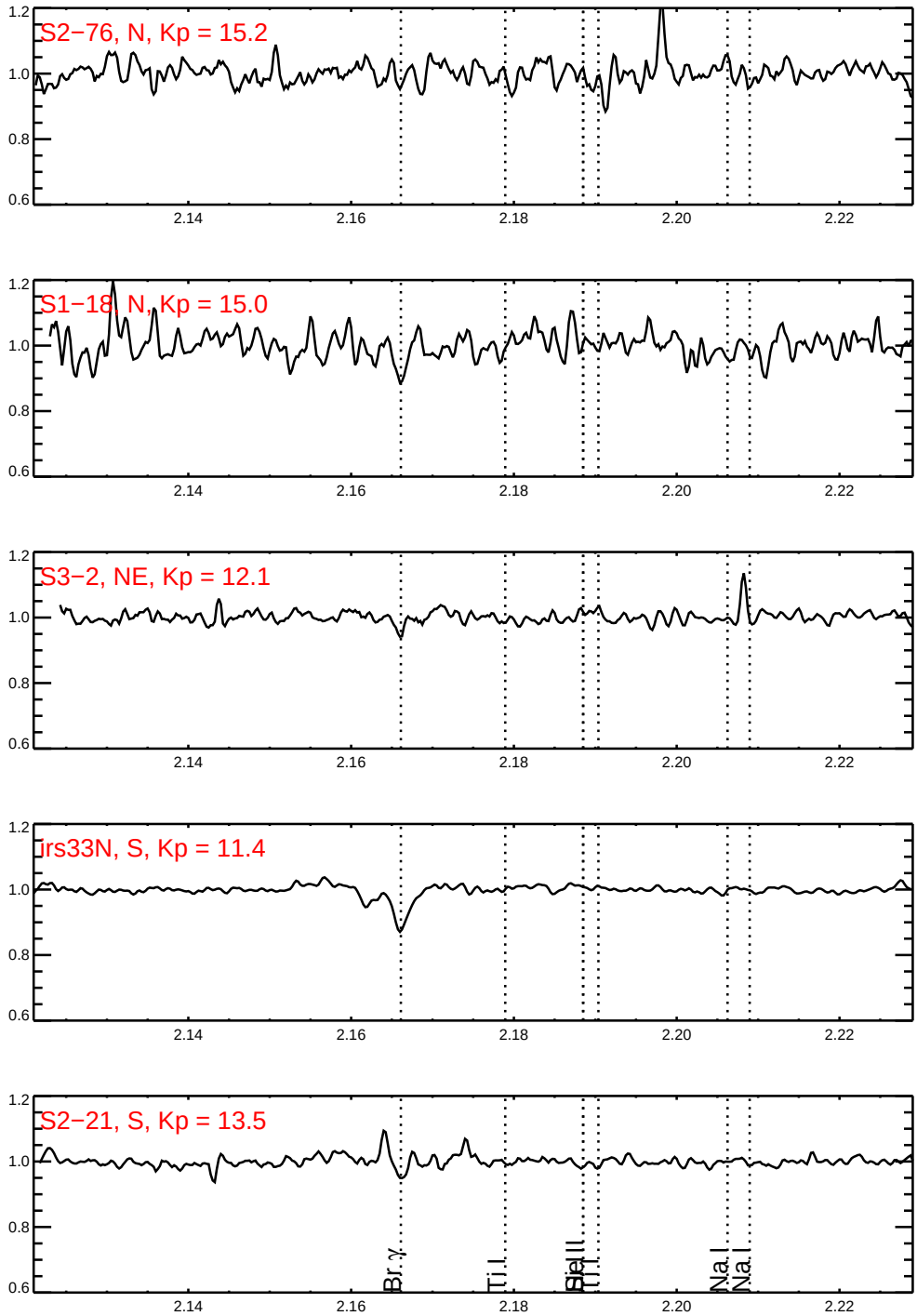

Figure B.7 Continuation of Figure B.1

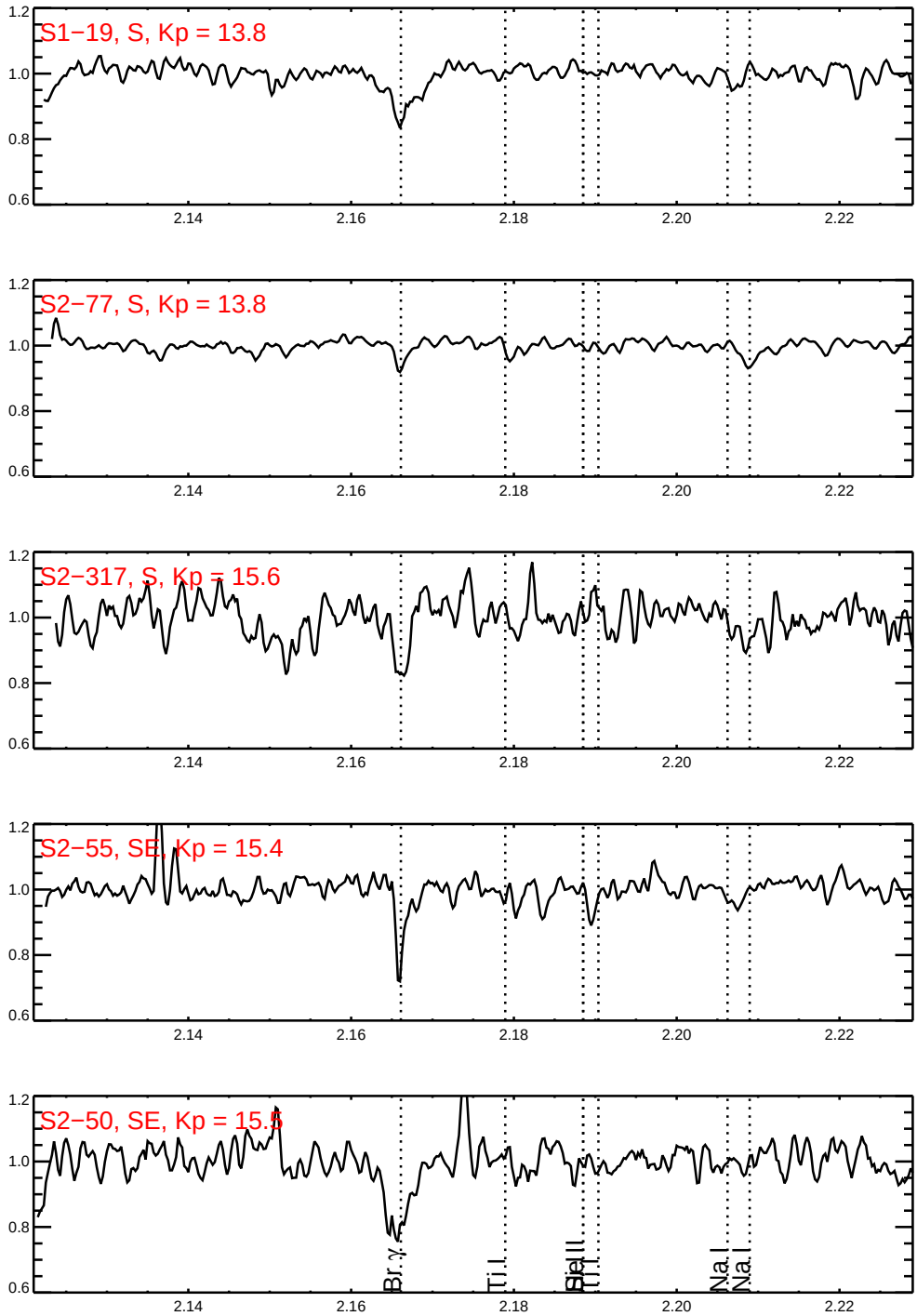

Figure B.8 Continuation of Figure B.1

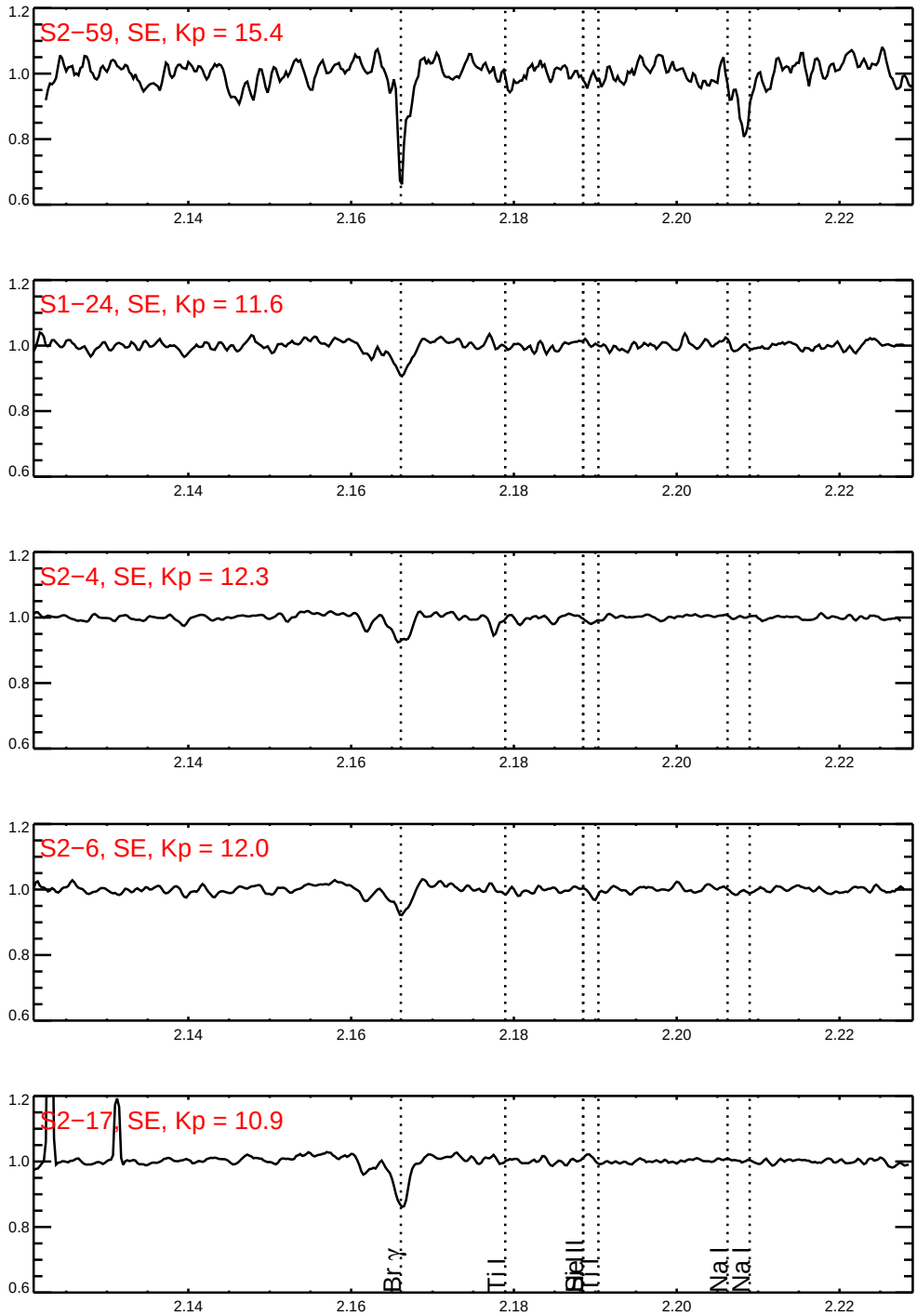

Figure B.9 Continuation of Figure B.1

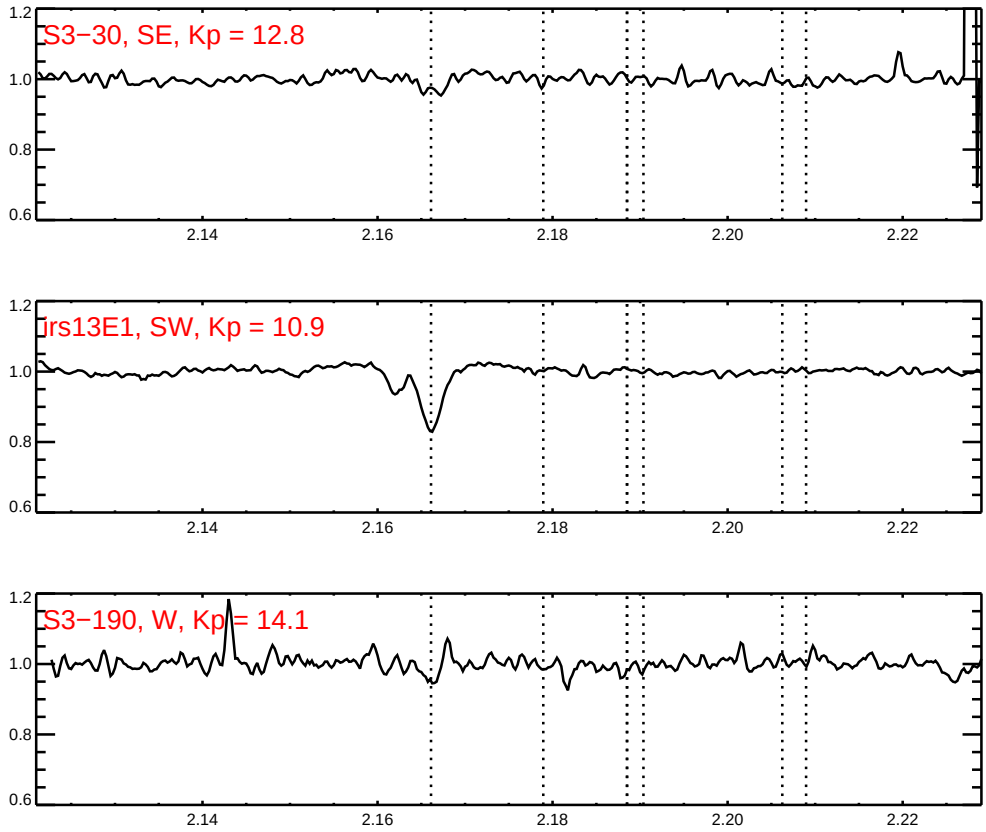

Figure B.10 Continuation of Figure B.1

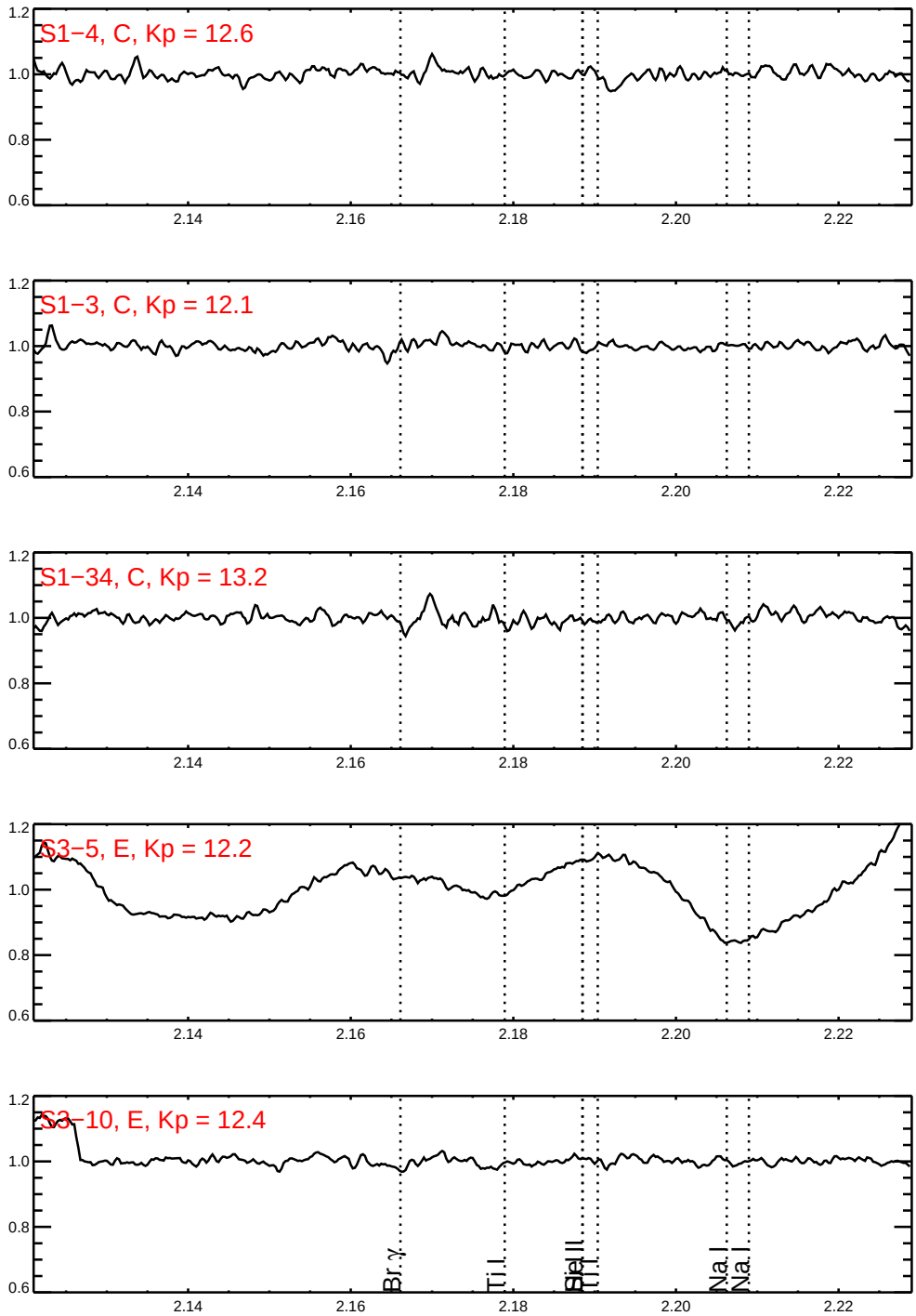

Figure B.11 Early-type stars with featureless spectra in Kn3, shifted to rest wavelength and grouped by OSIRIS field location.

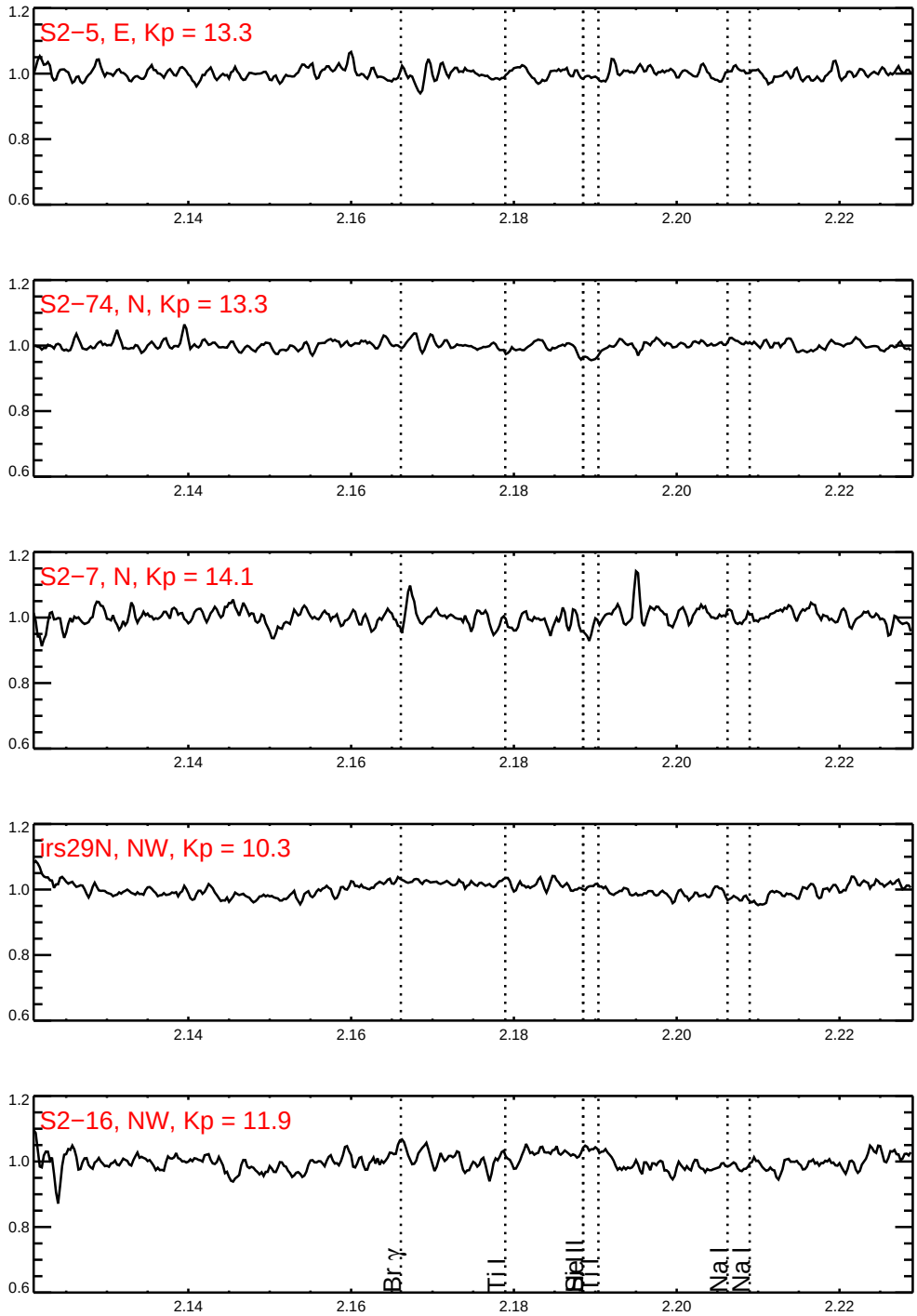

Figure B.12 Continuation of Figure B.11.

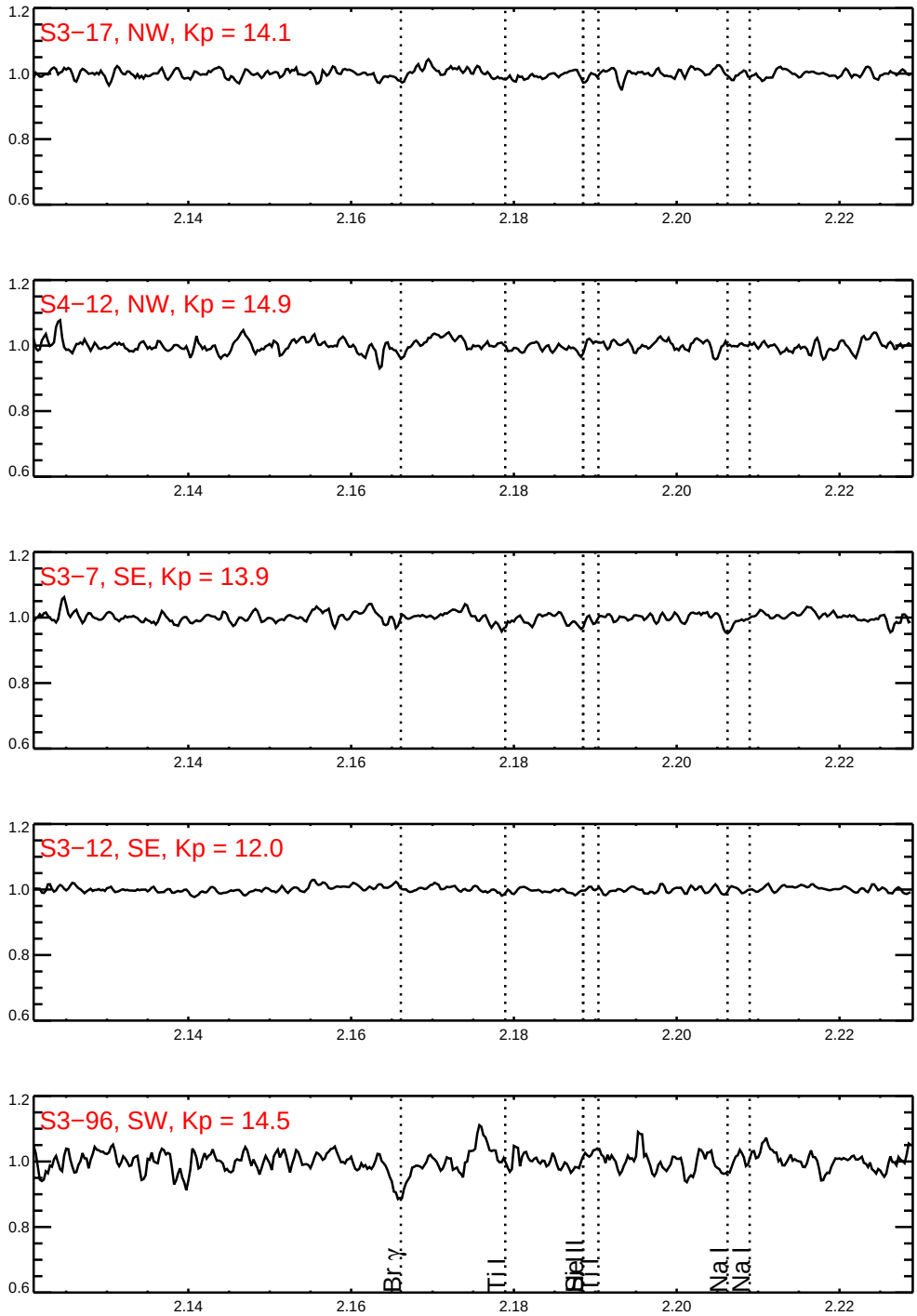

Figure B.13 Continuation of Figure B.11.

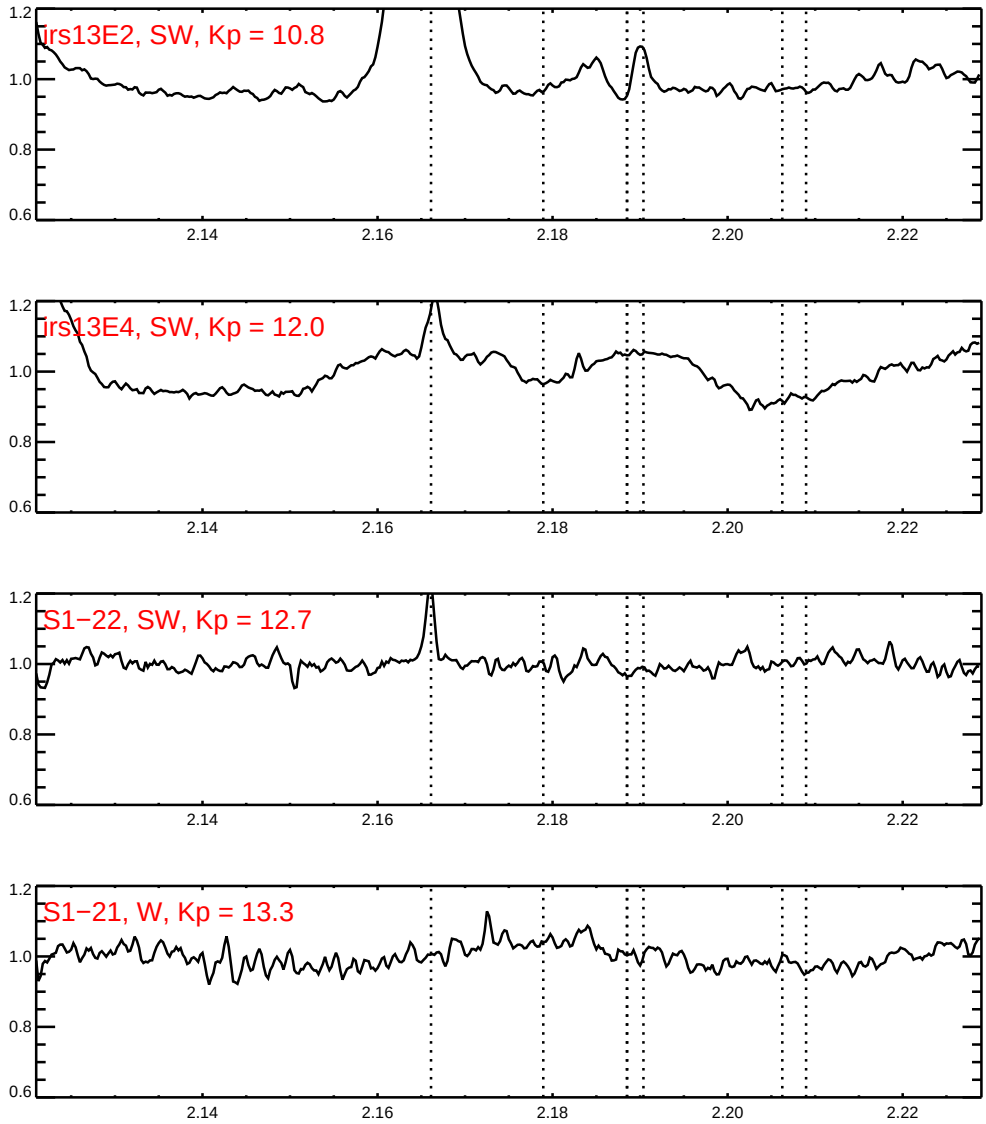

Figure B.14 Continuation of Figure B.11.

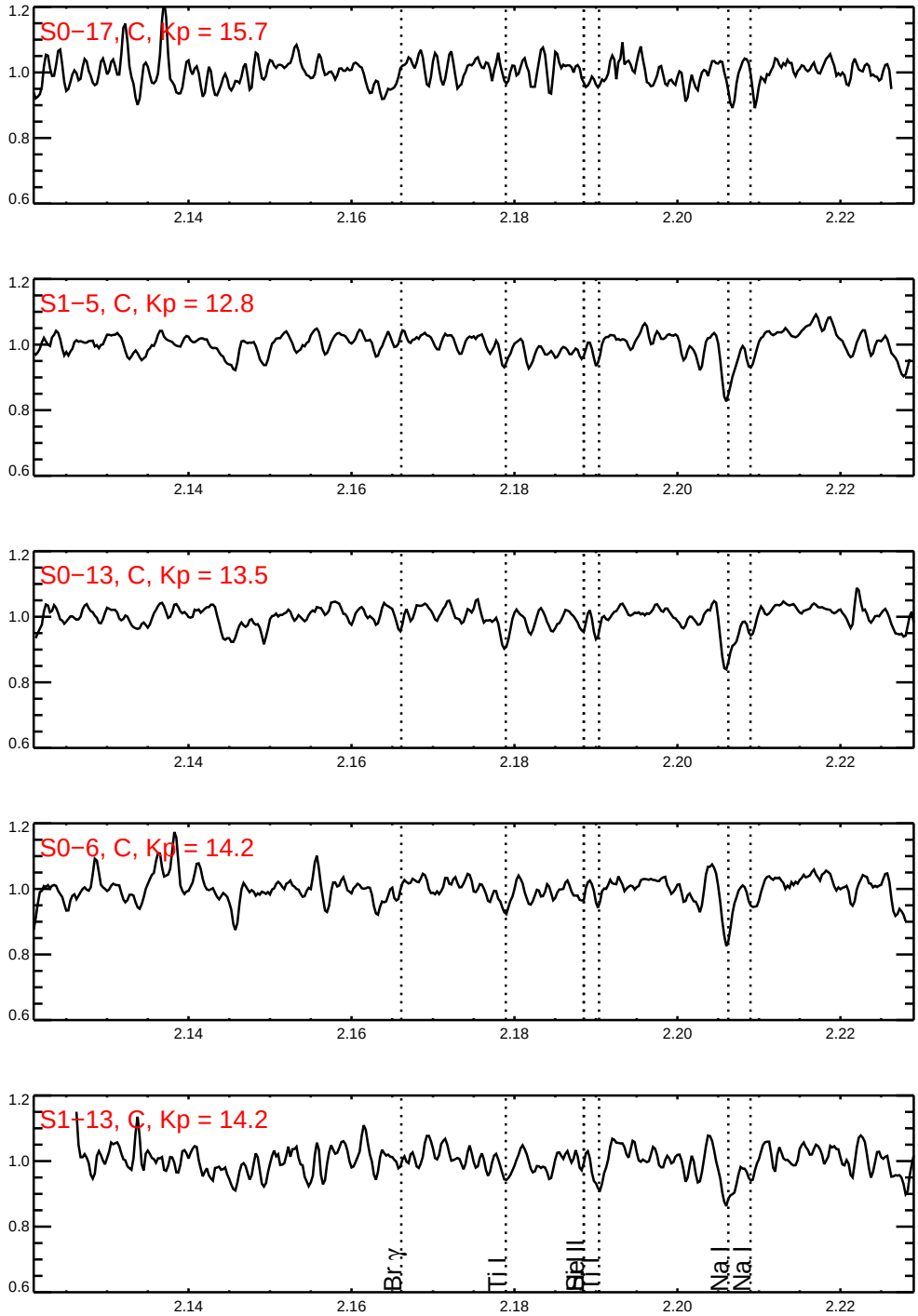

Figure B.15 Late-type stars in Kn3, shifted to rest wavelength and grouped by OSIRIS field location.

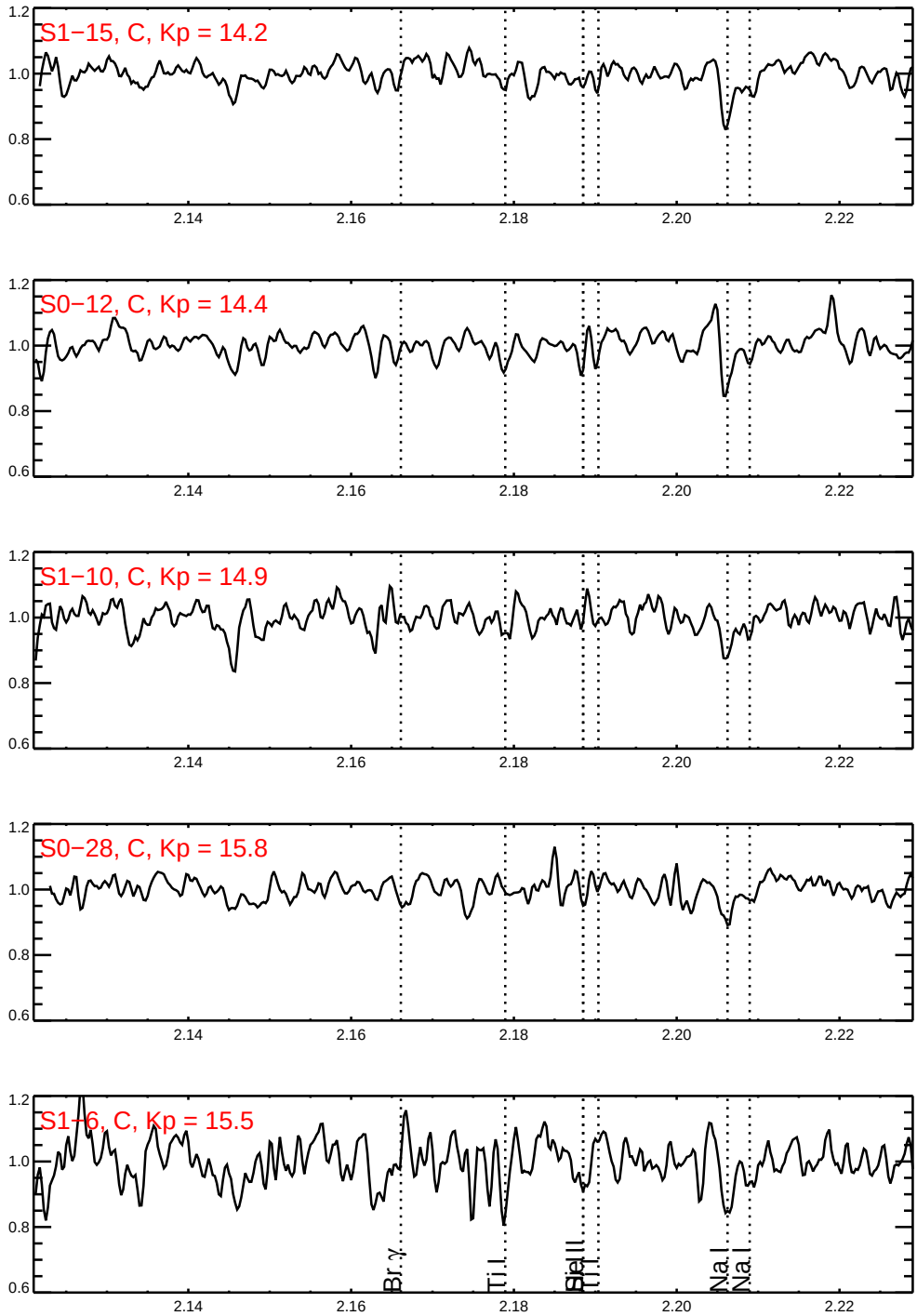

Figure B.16 Continuation of Figure B.15.

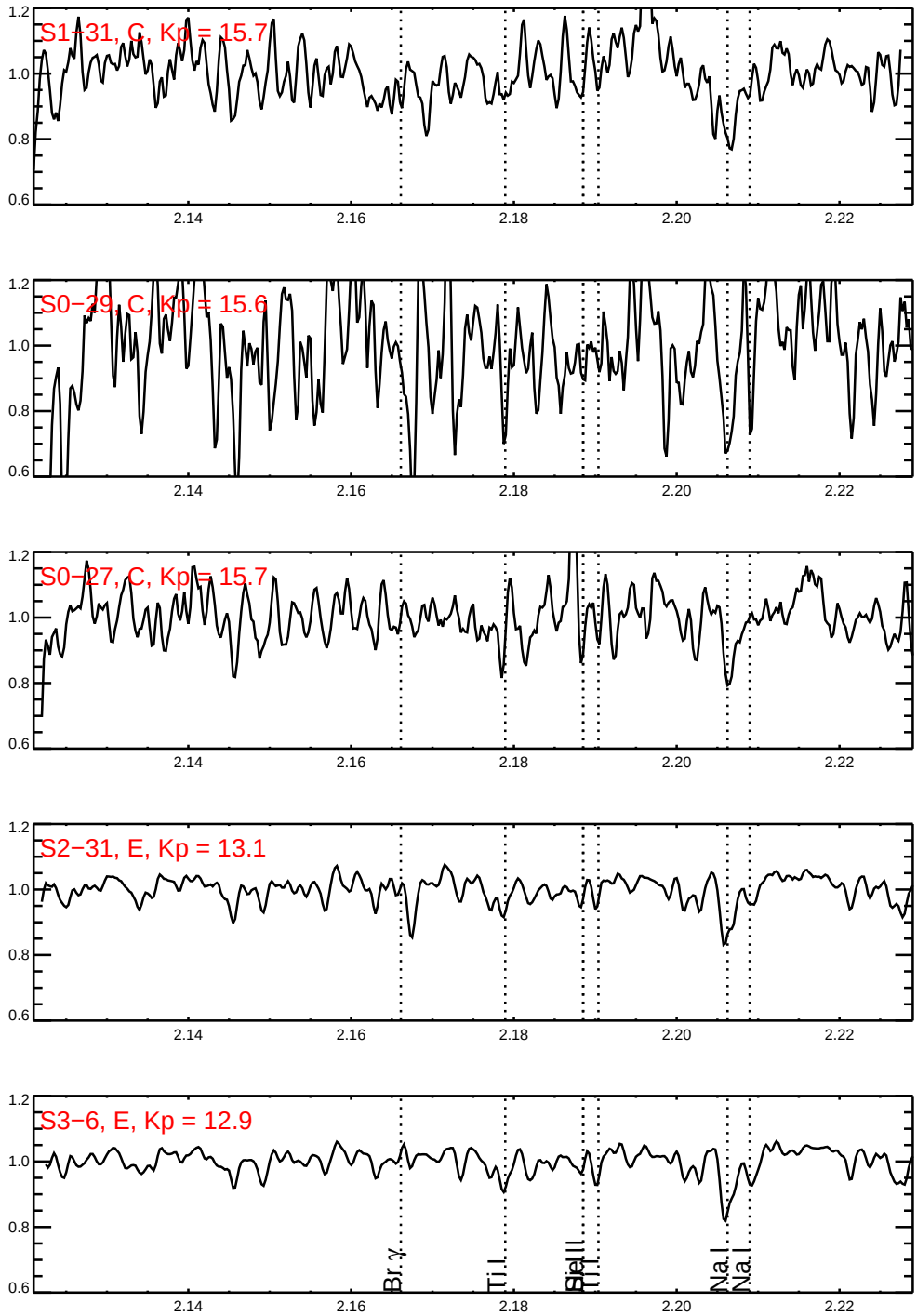

Figure B.17 Continuation of Figure B.15.

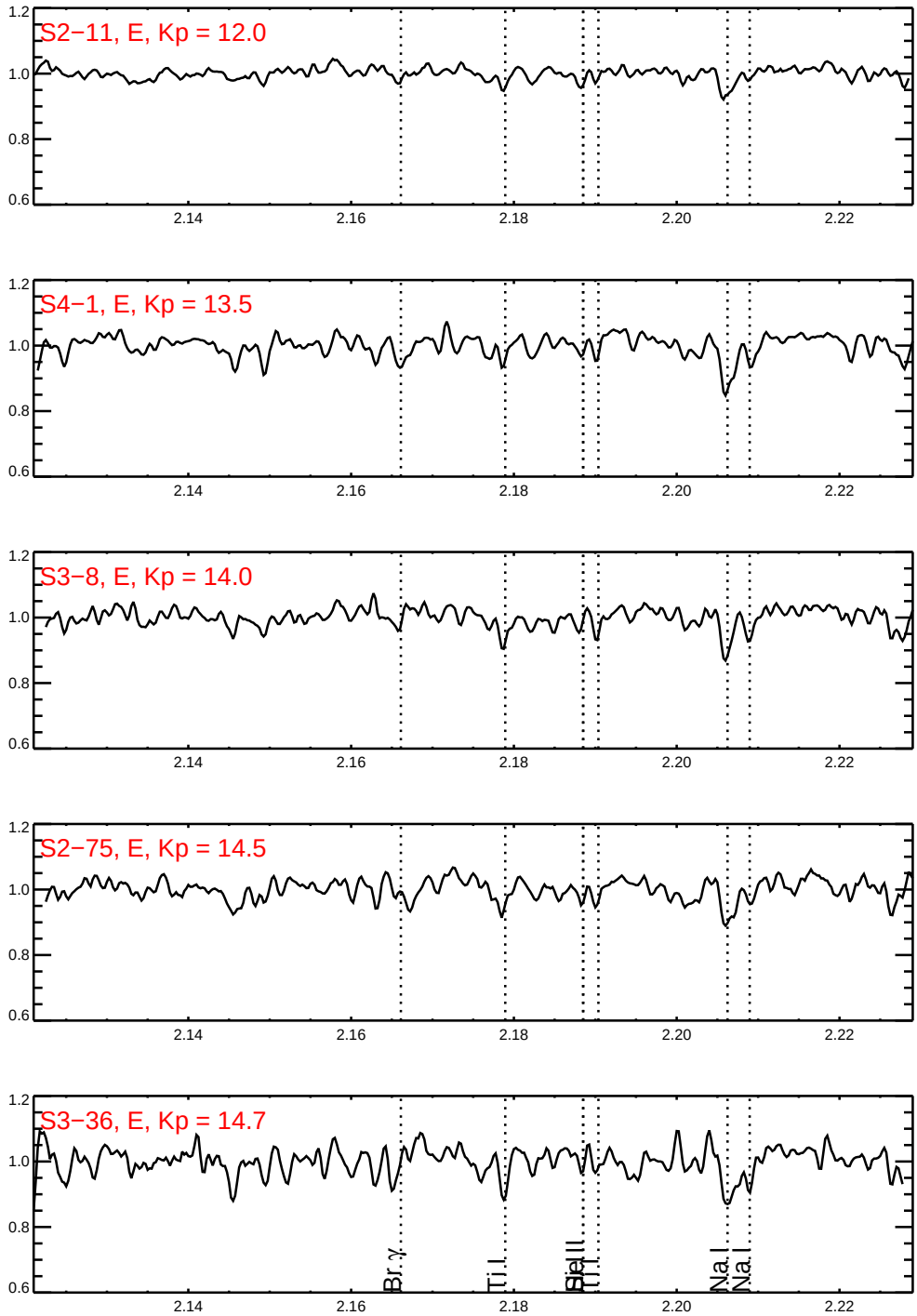

Figure B.18 Continuation of Figure B.15.

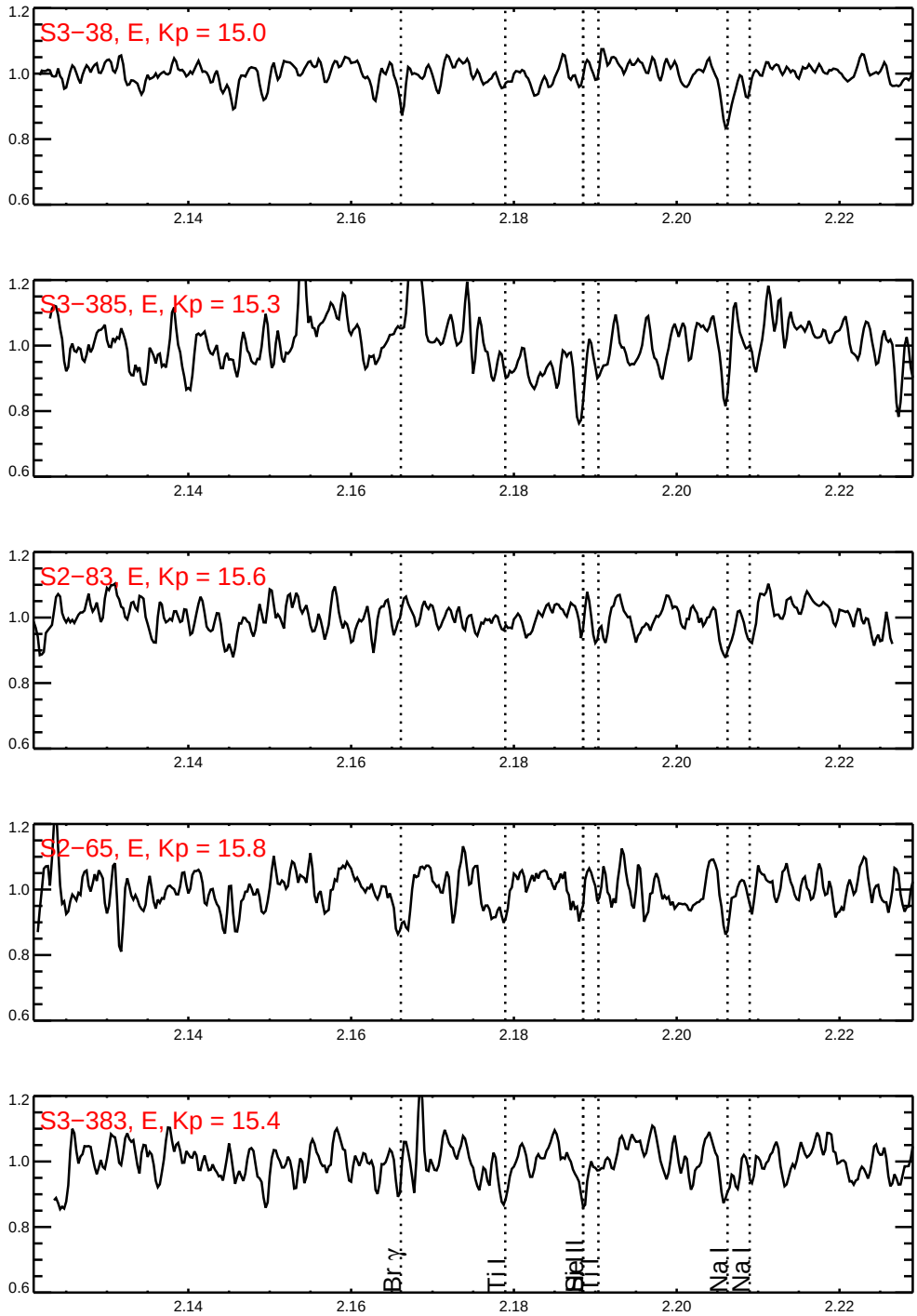

Figure B.19 Continuation of Figure B.15.

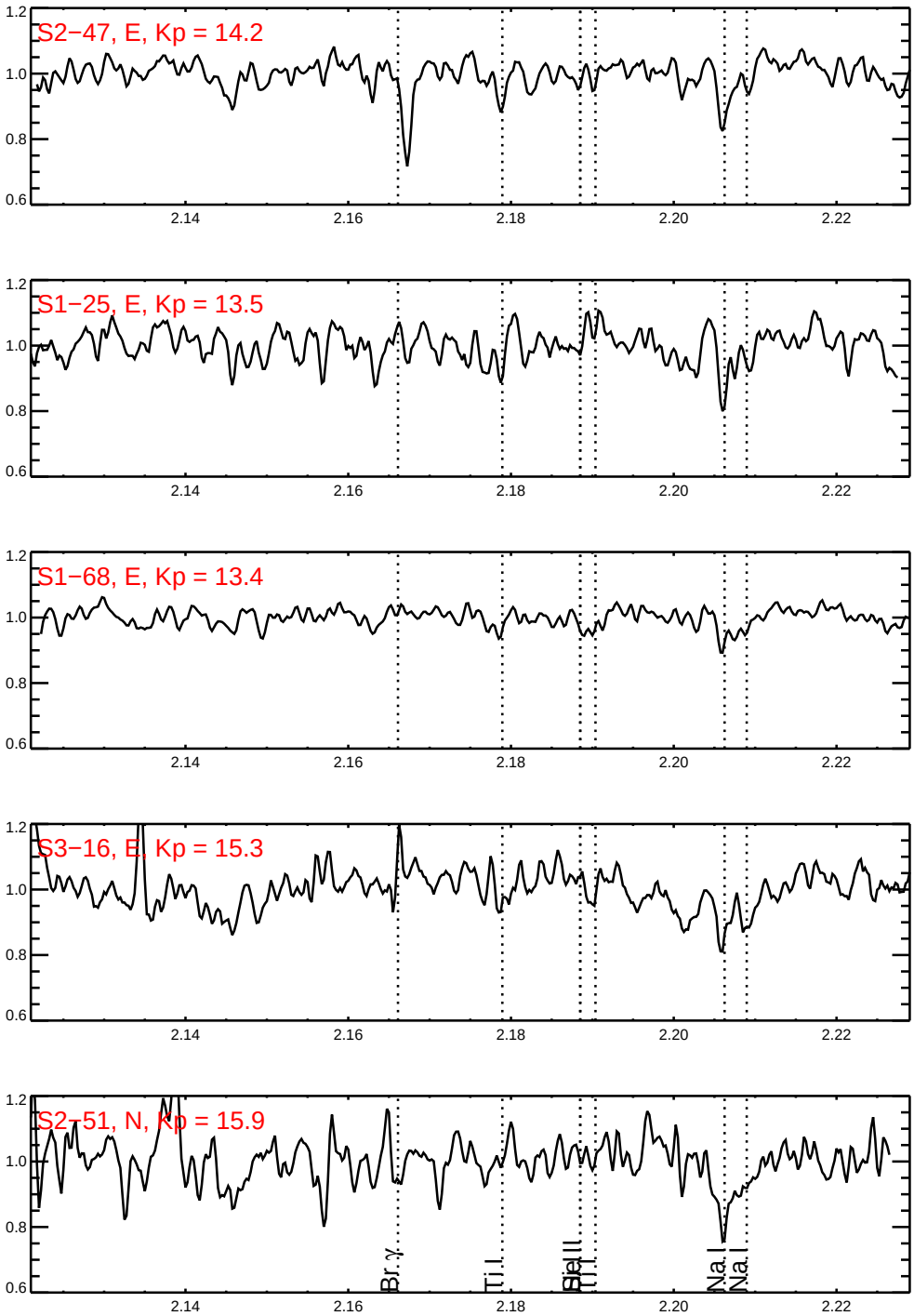

Figure B.20 Continuation of Figure B.15.

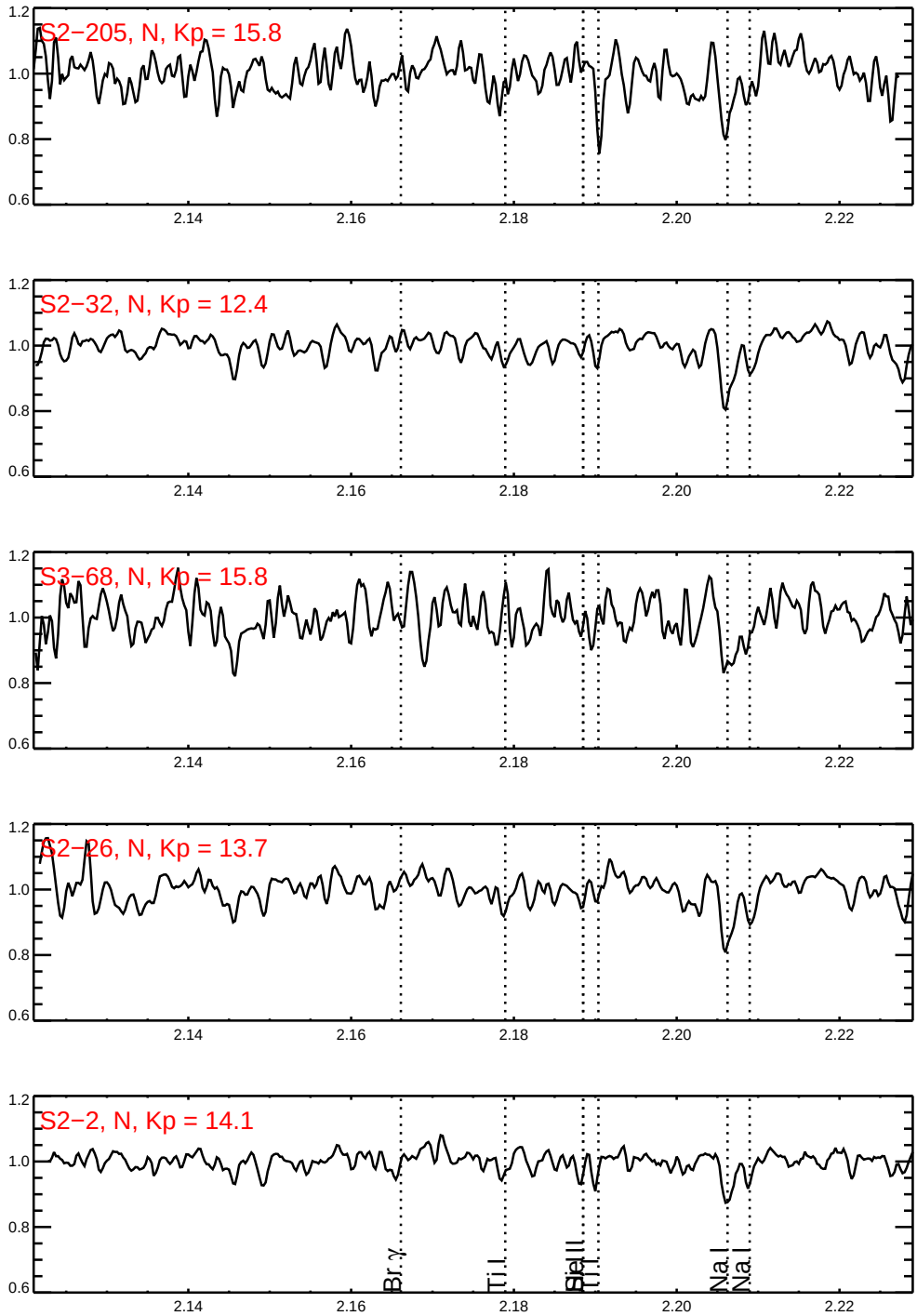

Figure B.21 Continuation of Figure B.15.

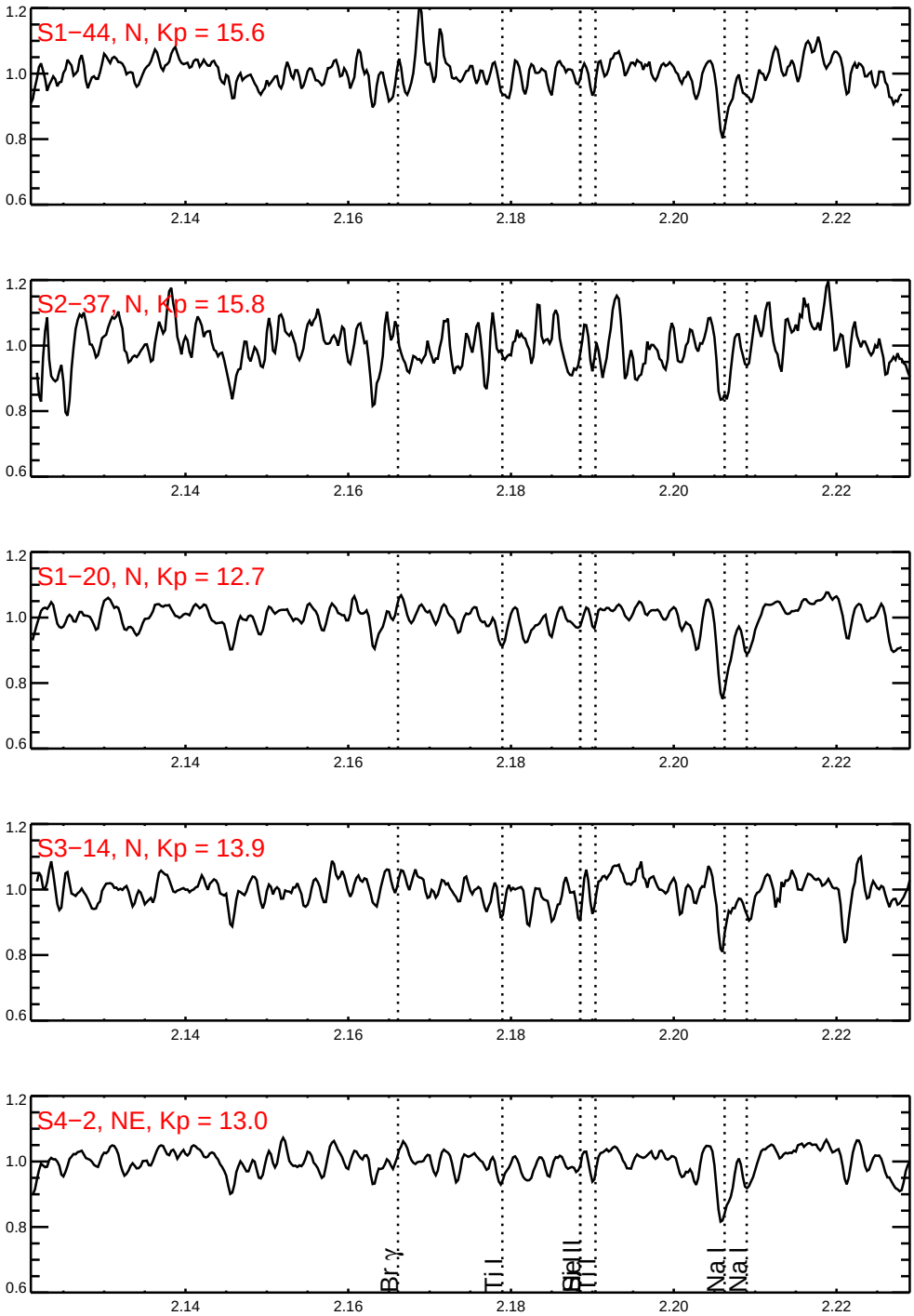

Figure B.22 Continuation of Figure B.15.

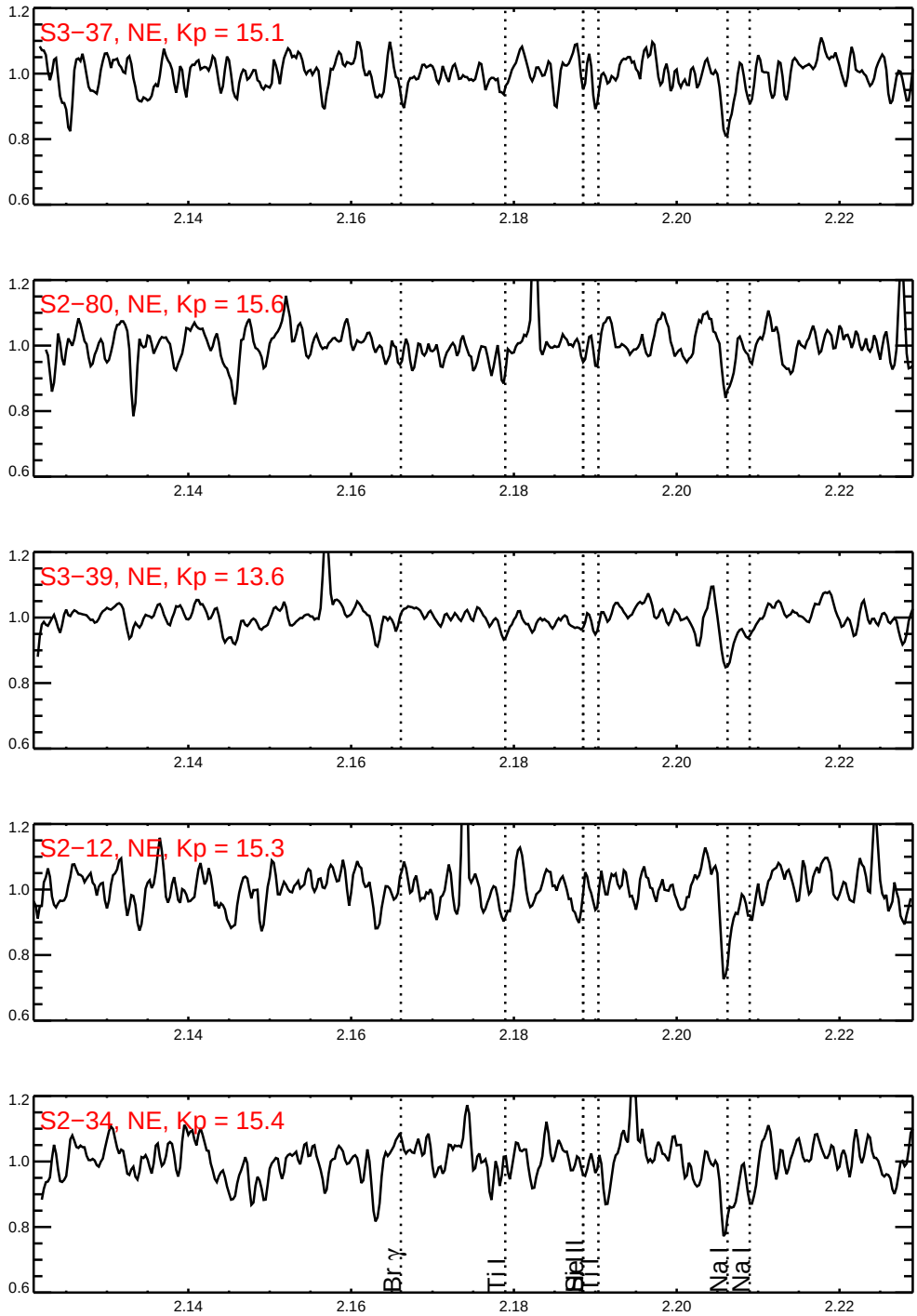

Figure B.23 Continuation of Figure B.15.

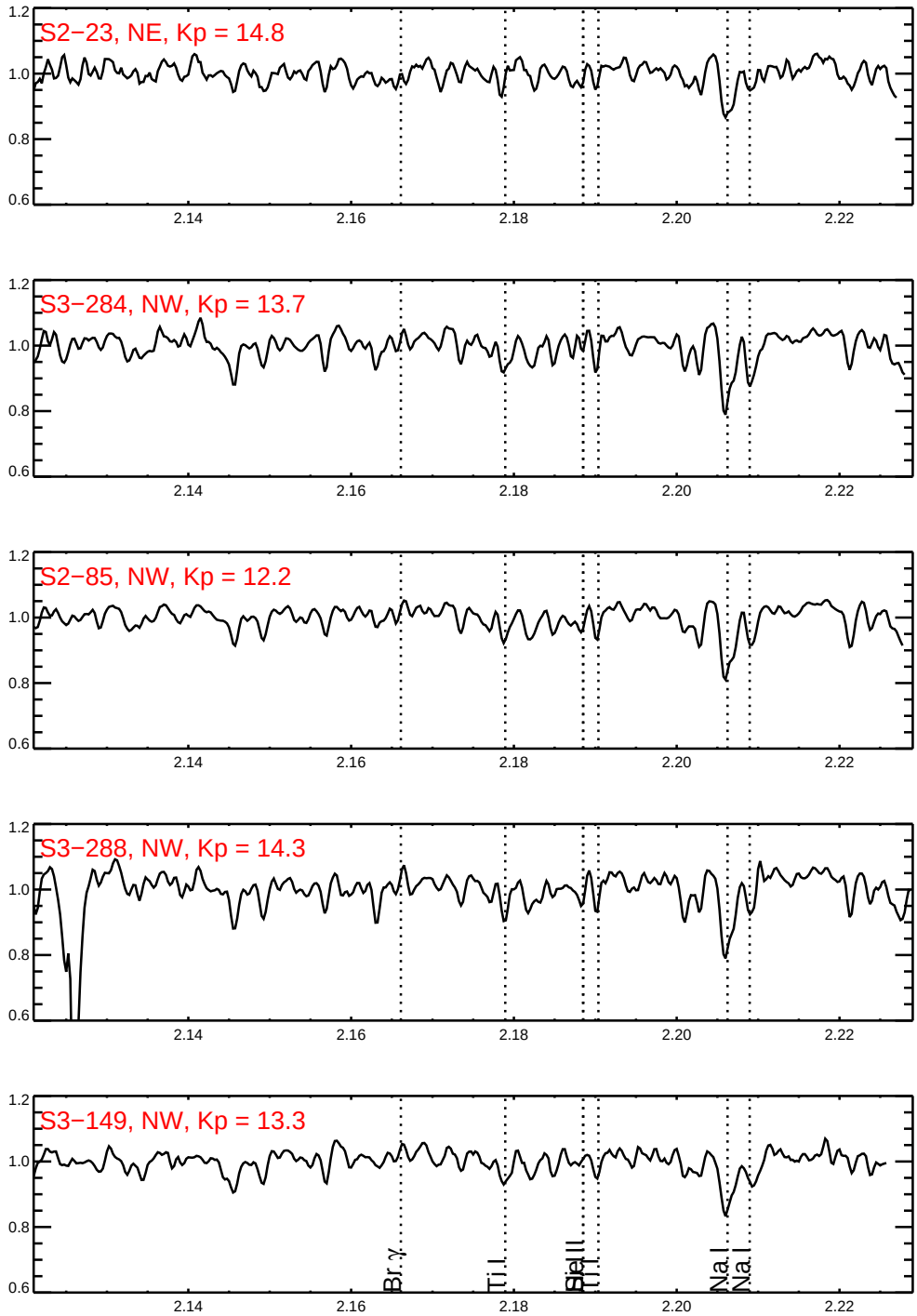

Figure B.24 Continuation of Figure B.15.

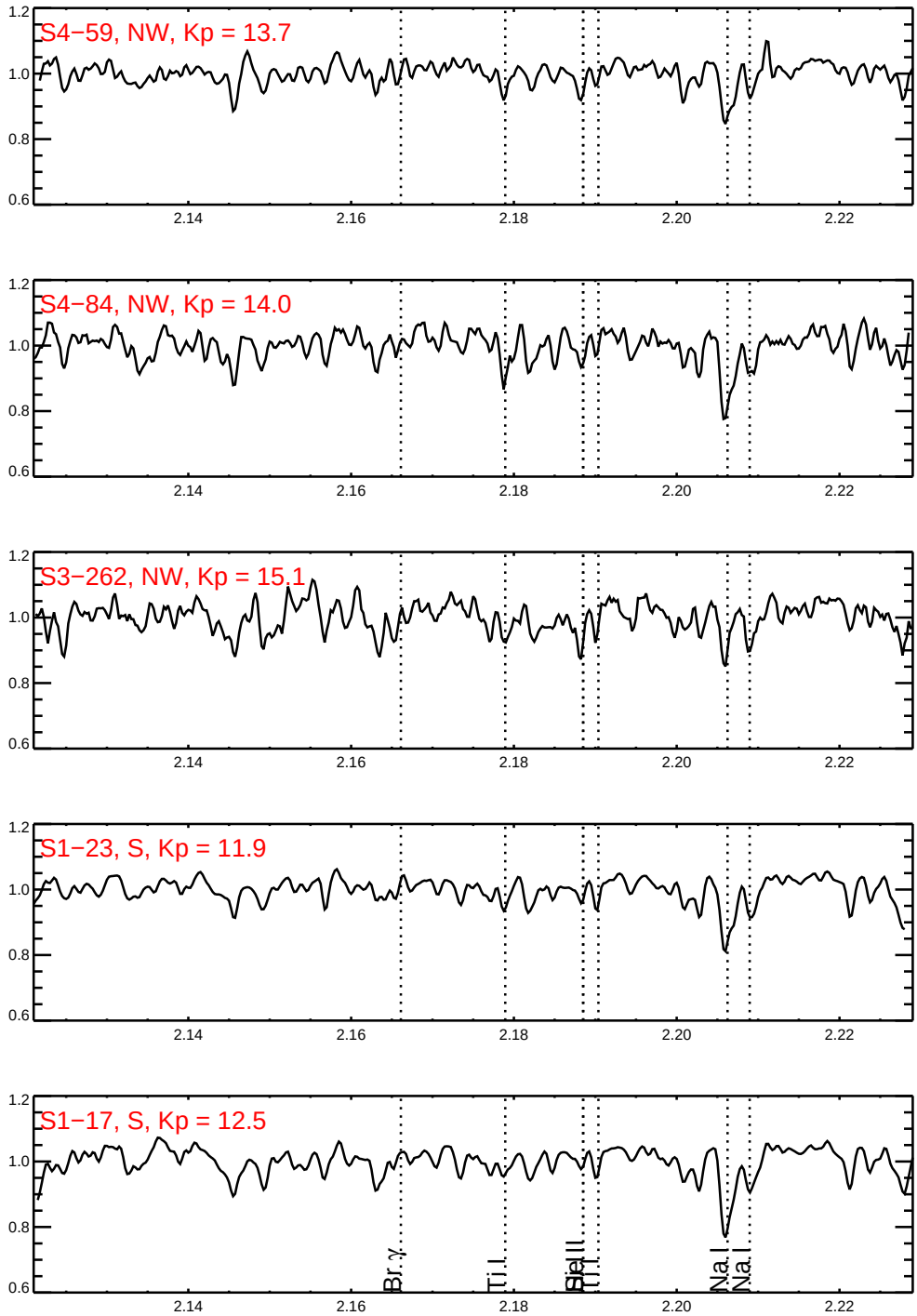

Figure B.25 Continuation of Figure B.15.

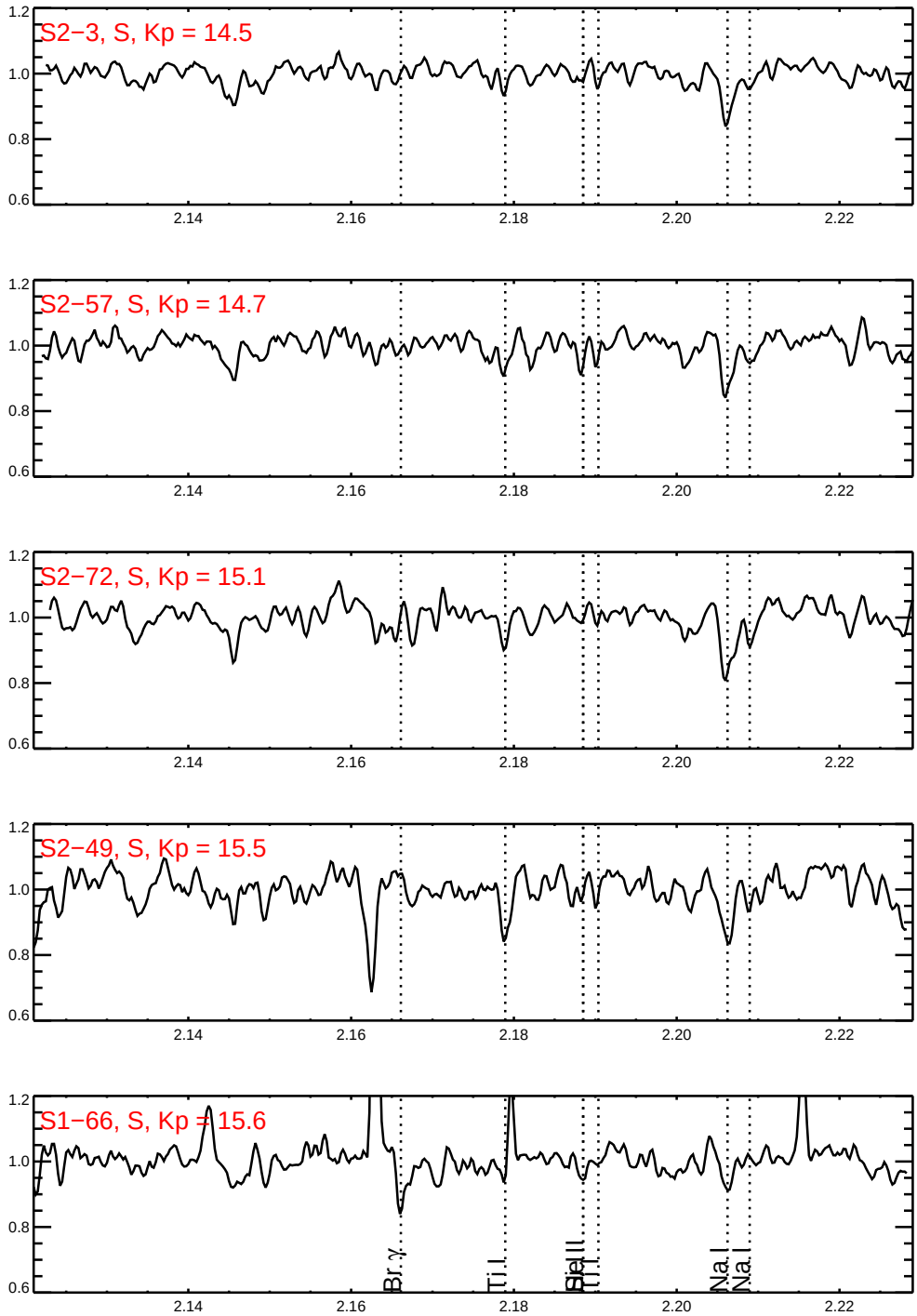

Figure B.26 Continuation of Figure B.15.

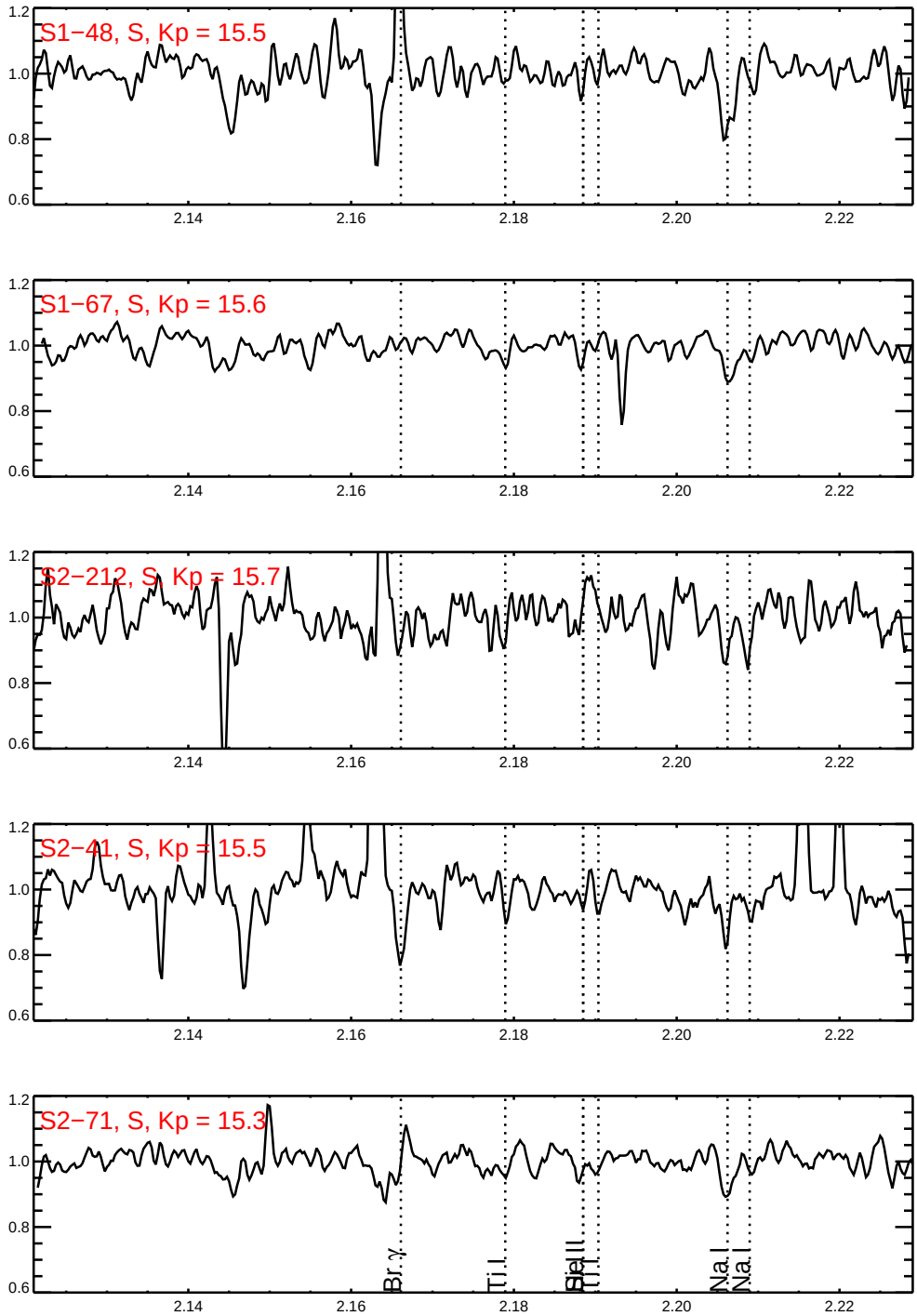

Figure B.27 Continuation of Figure B.15.

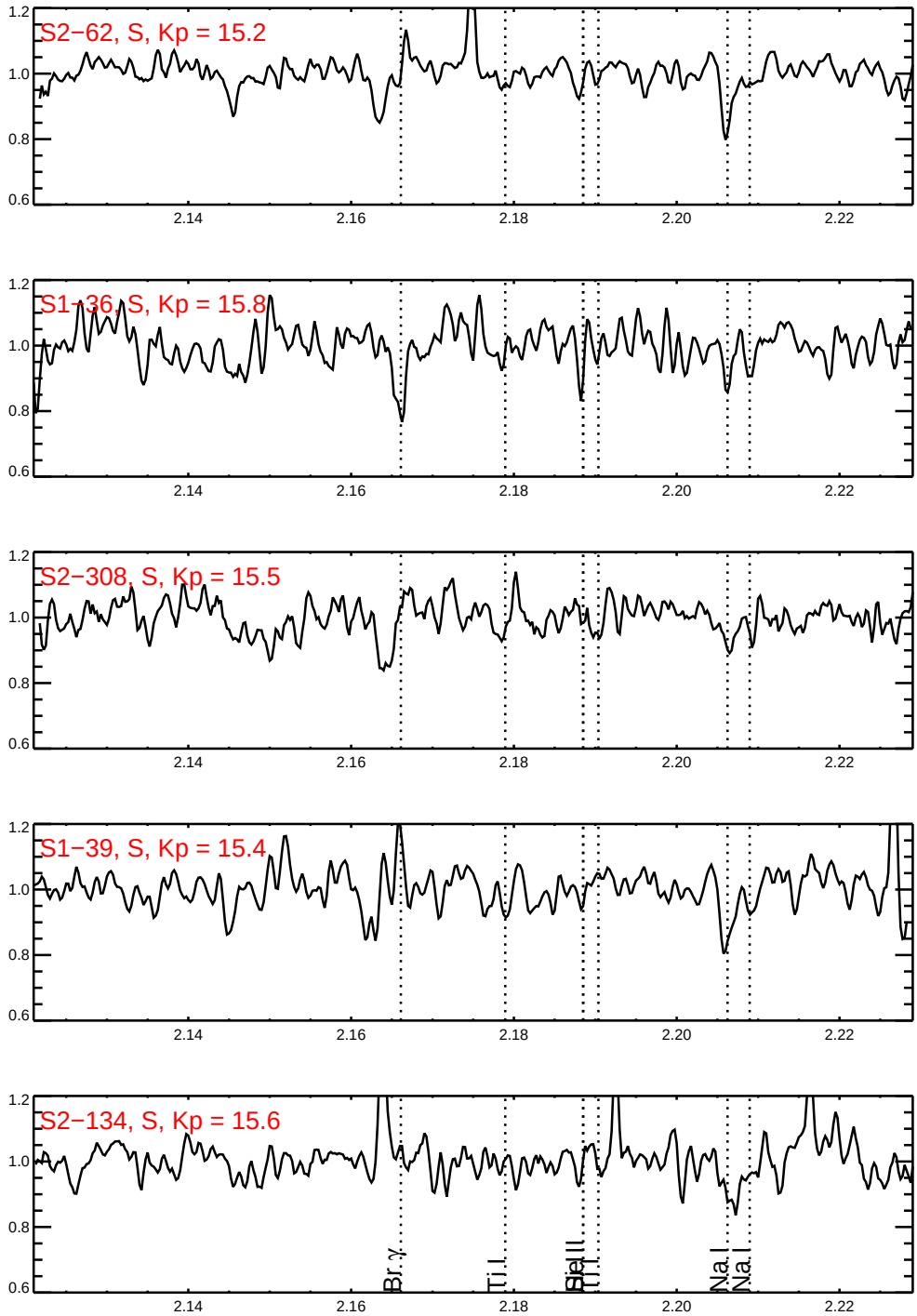

Figure B.28 Continuation of Figure B.15.

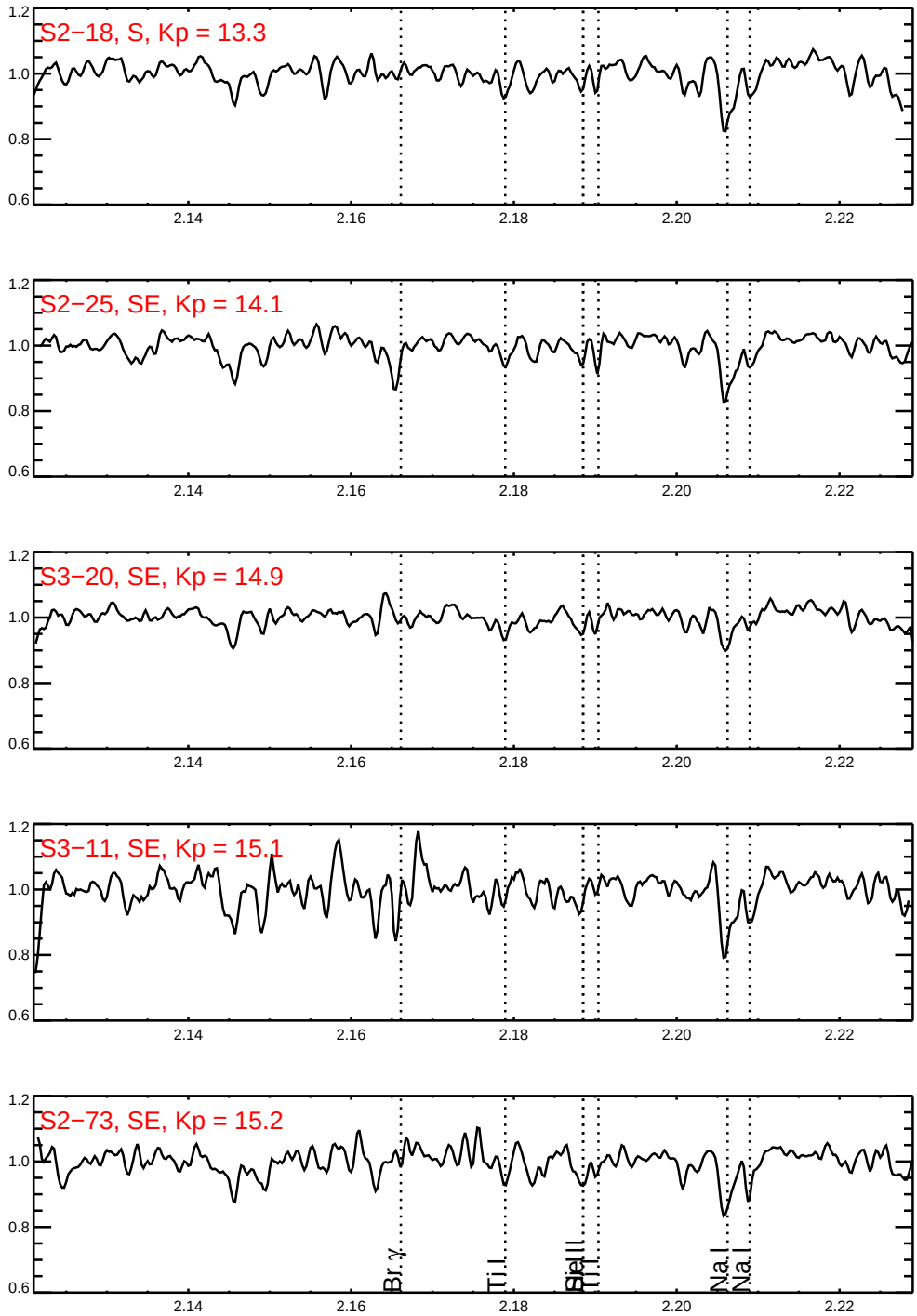

Figure B.29 Continuation of Figure B.15.

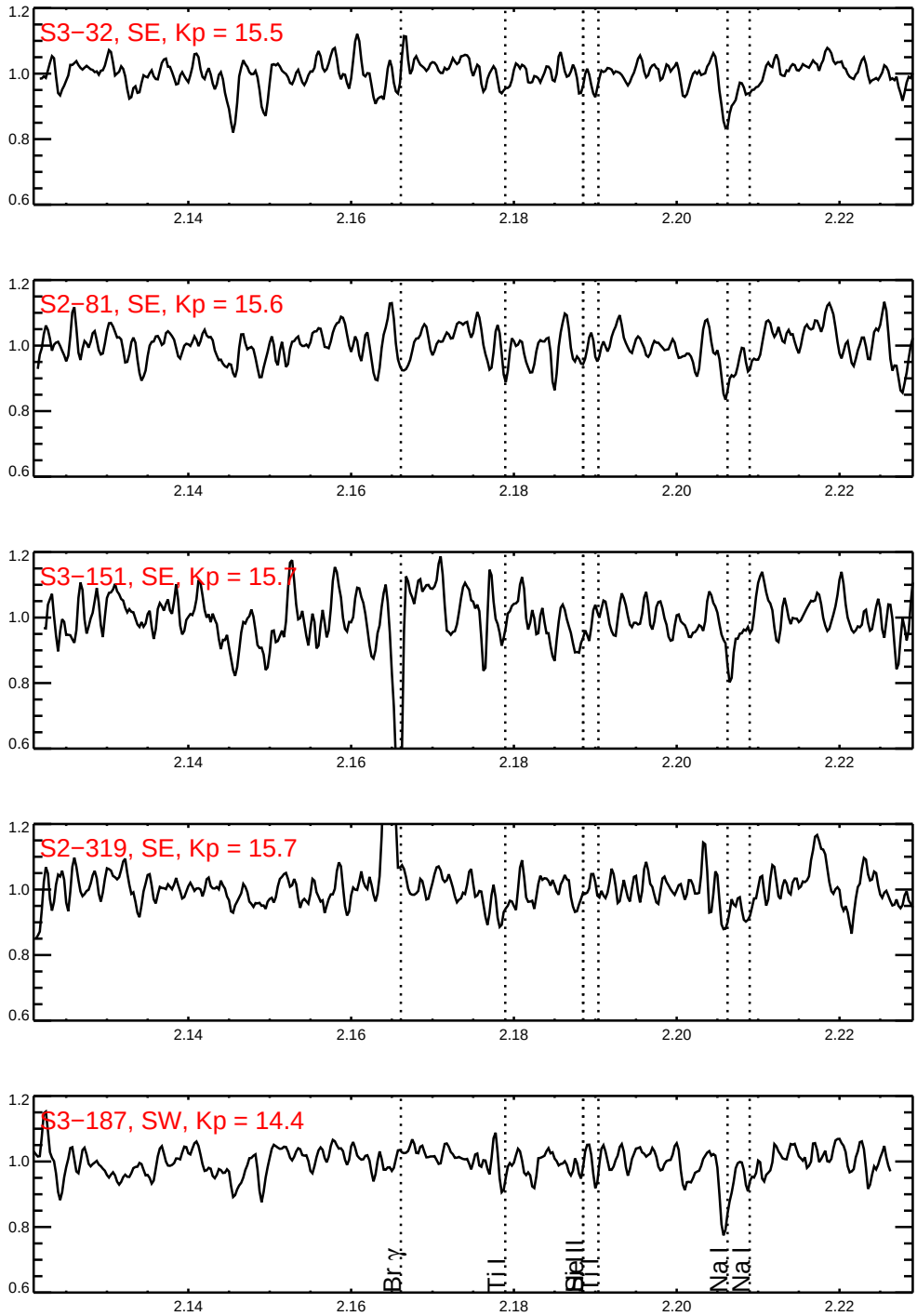

Figure B.30 Continuation of Figure B.15.

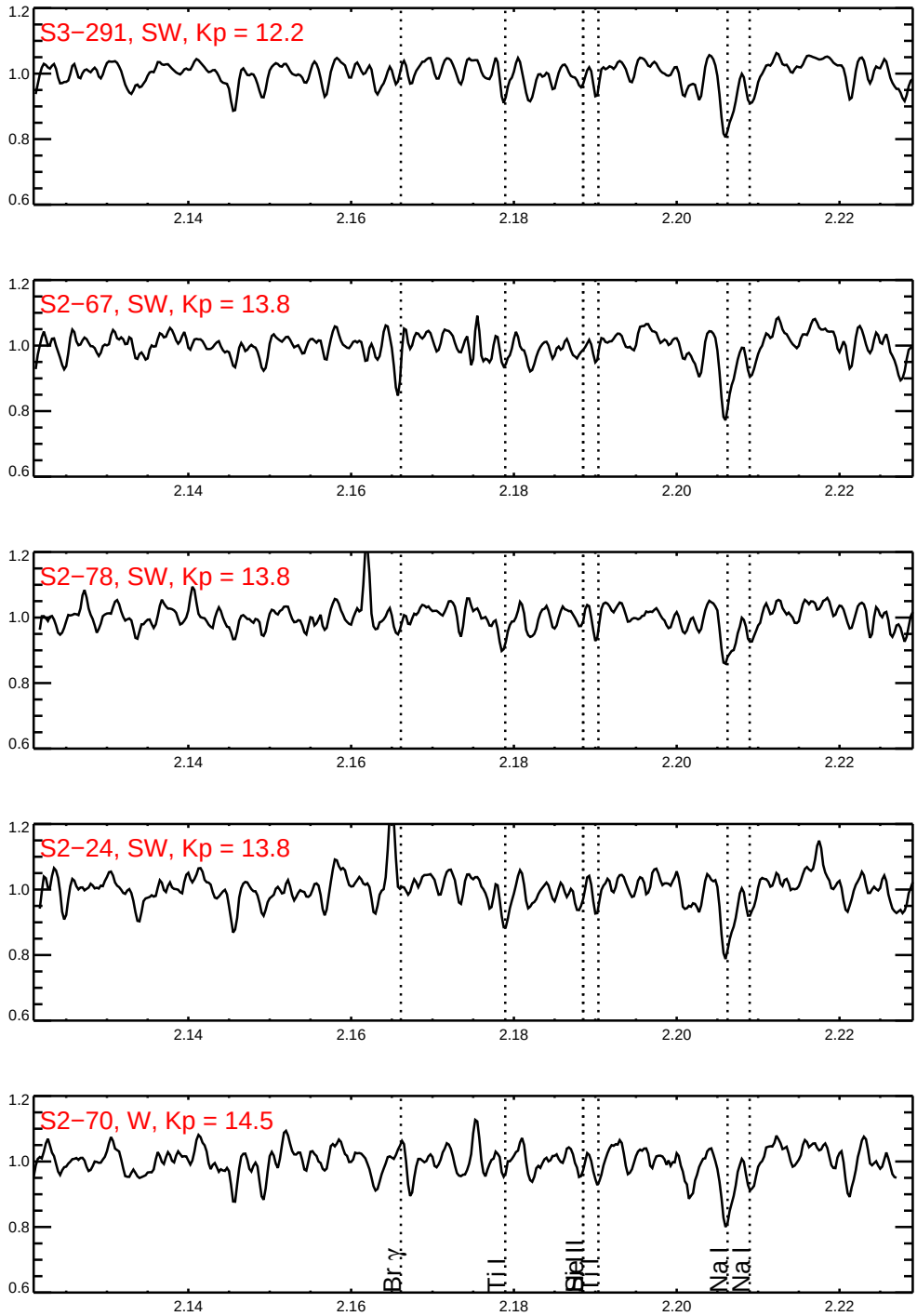

Figure B.31 Continuation of Figure B.15.

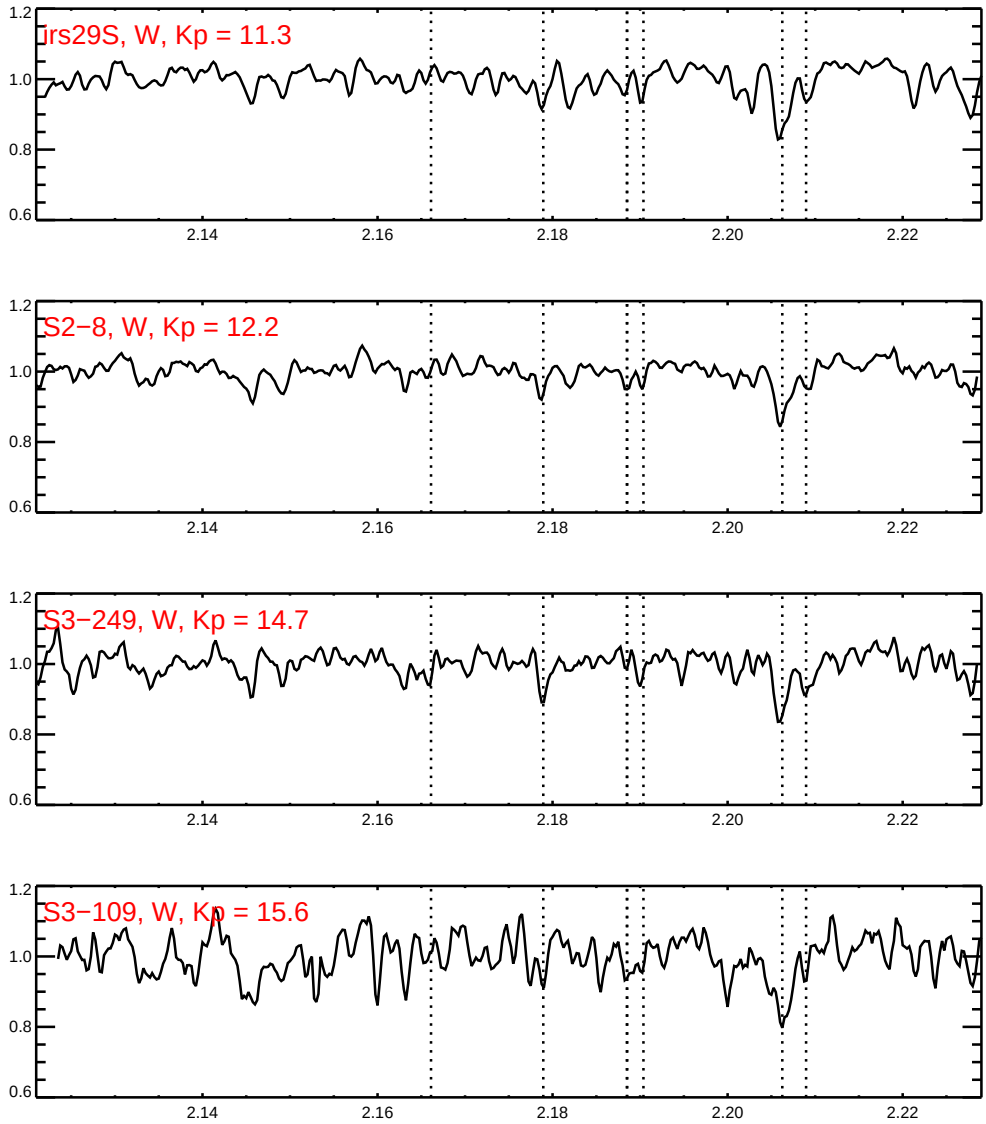

Figure B.32 Continuation of Figure B.15.

Bibliography

Alexander, T., & Hopman, C. 2008, ArXiv e-prints

Allen, D. A., Hyland, A. R., & Hillier, D. J. 1990, MNRAS, 244, 706

An, J. H., & Evans, N. W. 2006, ApJ, 642, 752

Armitage, P. J., & Reynolds, C. S. 2003, MNRAS, 341, 1041

Aschenbach, B., Grosso, N., Porquet, D., & Predehl, P. 2004, AAP, 417, 71

Baganoff, F. K., Maeda, Y., Morris, M., Bautz, M. W., Brandt, W. N., Cui, W., Doty, J. P., Feigelson, E. D., Garmire, G. P., Pravdo, S. H., Ricker, G. R., & Townsley, L. K. 2003, ApJ, 591, 891

Bahcall, J. N., & Wolf, R. A. 1976, ApJ, 209, 214

—. 1977, ApJ, 216, 883

Bailey, V. C., & Davies, M. B. 1999, MNRAS, 308, 257

Bartko, H., Martins, F., Fritz, T. K., Genzel, R., Levin, Y., Perets, H. B., Paumard, T., Nayakshin, S., Gerhard, O., Alexander, T., Dodds-Eden, K., Eisenhauer, F., Gillessen, S., Mascetti, L., Ott, T., Perrin, G., Pfuhl, O., Reid, M. J., Rouan, D., Sternberg, A., & Trippe, S. 2009, ApJ, 697, 1741

Baumgardt, H., Gualandris, A., & Portegies Zwart, S. 2006, MNRAS, 372, 174

Becklin, E. E., & Neugebauer, G. 1968, ApJ, 151, 145

Bélanger, G., Goldwurm, A., Melia, F., Ferrando, P., Grosso, N., Porquet, D., Warwick, R., & Yusef-Zadeh, F. 2005, ApJ, 635, 1095

Bélanger, G., Terrier, R., de Jager, O. C., & Melia, F. 2008 in prep, ApJ

Benlloch, S., Wilms, J., Edelson, R., Yaqoob, T., & Staubert, R. 2001, ApJL, 562, L121

Binney, J., & Tremaine, S. 2008, Galactic Dynamics: Second Edition (Princeton University Press)

Blum, R. D., Ramírez, S. V., Sellgren, K., & Olsen, K. 2003, ApJ, 597, 323

Blum, R. D., Sellgren, K., & Depoy, D. L. 1996, ApJ, 470, 864

Buchholz, R. M., Schödel, R., & Eckart, A. 2009, AAP, 499, 483

Cohn, H., & Kulsrud, R. M. 1978, ApJ, 226, 1087

Dale, J. E., Davies, M. B., Church, R. P., & Freitag, M. 2009, MNRAS, 393, 1016

Diolaiti, E., Bendinelli, O., Bonaccini, D., Close, L., Currie, D., & Parmeggiani, G. 2000, A&AS, 147, 335

Do, T., Ghez, A. M., Morris, M. R., Lu, J. R., Matthews, K., Yelda, S., & Larkin, J. 2009a, ApJ, 703, 1323

Do, T., Ghez, A. M., Morris, M. R., Yelda, S., Meyer, L., Lu, J. R., Hornstein, S. D., & Matthews, K. 2009b, ApJ, 691, 1021

Ducati, J. R., Bevilacqua, C. M., Rembold, S. B., & Ribeiro, D. 2001, ApJ, 558, 309

Eckart, A., Baganoff, F. K., Schödel, R., Morris, M., Genzel, R., Bower, G. C., Marrone, D., Moran, J. M., Viehmann, T., Bautz, M. W., Brandt, W. N., Garmire, G. P., Ott, T., Trippe, S., Ricker, G. R., Straubmeier, C., Roberts, D. A., Yusef-Zadeh, F., Zhao, J. H., & Rao, R. 2006a, AAP, 450, 535

Eckart, A., Baganoff, F. K., Zamaninasab, M., Morris, M. R., Schödel, R., Meyer, L., Muzic, K., Bautz, M. W., Brandt, W. N., Garmire, G. P., Ricker, G. R., Kunneriath, D., Straubmeier, C., Duschl, W., Dovciak, M., Karas, V., Markoff, S., Najarro, F., Mauerhan, J., Moultaka, J., & Zensus, A. 2008, AAP, 479, 625

Eckart, A., Schödel, R., Meyer, L., Trippe, S., Ott, T., & Genzel, R. 2006b, AAP, 455, 1

Eisenhauer, F., Genzel, R., Alexander, T., Abuter, R., Paumard, T., Ott, T., Gilbert, A., Gillessen, S., Horrobin, M., Trippe, S., Bonnet, H., Dumas, C., Hubin, N., Kaufer, A., Kissler-Patig, M., Monnet, G., Ströbele, S., Szeifert, T., Eckart, A., Schödel, R., & Zucker, S. 2005, ApJ, 628, 246

Falanga, M., Melia, F., Tagger, M., Goldwurm, A., & Bélanger, G. 2007, ApJL, 662, L15

Ferrarese, L., & Ford, H. 2005, Space Science Reviews, 116, 523

Figer, D. F., Becklin, E. E., McLean, I. S., Gilbert, A. M., Graham, J. R., Larkin, J. E., Levenson, N. A., Teplitz, H. I., Wilcox, M. K., & Morris, M. 2000, ApJL, 533, L49

Figer, D. F., Gilmore, D., Kim, S. S., Morris, M., Becklin, E. E., McLean, I. S., Gilbert, A. M., Graham, J. R., Larkin, J. E., Levenson, N. A., & Teplitz, H. I. 2003, ApJ, 599, 1139

Förster Schreiber, N. M. 2000, AJ, 120, 2089

Genzel, R., Pichon, C., Eckart, A., Gerhard, O. E., & Ott, T. 2000, MNRAS, 317, 348

Genzel, R., Schödel, R., Ott, T., Eckart, A., Alexander, T., Lacombe, F., Rouan, D., & Aschenbach, B. 2003a, Nature, 425, 934

Genzel, R., Schödel, R., Ott, T., Eisenhauer, F., Hofmann, R., Lehnert, M., Eckart, A., Alexander, T., Sternberg, A., Lenzen, R., Clénet, Y., Lacombe, F., Rouan, D., Renzini, A., & Tacconi-Garman, L. E. 2003b, ApJ, 594, 812

Ghez, A. M., Duchêne, G., Matthews, K., Hornstein, S. D., Tanner, A., Larkin, J., Morris, M., Becklin, E. E., Salim, S., Kremenek, T., Thompson, D., Soifer, B. T., Neugebauer, G., & McLean, I. 2003, ApJL, 586, L127

Ghez, A. M., Hornstein, S. D., Lu, J. R., Bouchez, A., Le Mignant, D., van Dam, M. A., Wizinowich, P., Matthews, K., Morris, M., Becklin, E. E., Campbell, R. D., Chin, J. C. Y., Hartman, S. K., Johansson, E. M., Lafon, R. E., Stomski, P. J., & Summers, D. M. 2005a, ApJ, 635, 1087

Ghez, A. M., Salim, S., Hornstein, S. D., Tanner, A., Lu, J. R., Morris, M., Becklin, E. E., & Duchêne, G. 2005b, ApJ, 620, 744

Ghez, A. M., Salim, S., Weinberg, N. N., Lu, J. R., Do, T., Dunn, J. K., Matthews, K., Morris, M. R., Yelda, S., Becklin, E. E., Kremenek, T., Milosavljevic, M., & Naiman, J. 2008, ApJ, 689, 1044

Gierliński, M., & Zdziarski, A. A. 2003, MNRAS, 343, L84

Gillessen, S., Eisenhauer, F., Trippe, S., Alexander, T., Genzel, R., Martins, F., & Ott, T. 2009, ApJ, 692, 1075

Gualandris, A., & Merritt, D. 2009, ArXiv e-prints

Haller, J. W., Rieke, M. J., Rieke, G. H., Tamblyn, P., Close, L., & Melia, F. 1996, ApJ, 456, 194

Hanson, M. M., Conti, P. S., & Rieke, M. J. 1996, ApJS, 107, 281

Hopman, C., & Alexander, T. 2006, ApJ, 645, 1152

Horne, J. H., & Baliunas, S. L. 1986, ApJ, 302, 757

Hornstein, S. D., Ghez, A. M., Tanner, A., Morris, M., Becklin, E. E., & Wizinowich, P. 2002, ApJL, 577, L9

Hornstein, S. D., Matthews, K., Ghez, A. M., Lu, J. R., Morris, M., Becklin, E. E., Rafelski, M., & Baganoff, F. K. 2007, ApJ, 667, 900

Hughes, P. A., Aller, H. D., & Aller, M. F. 1992, ApJ, 396, 469

Kataoka, J., Takahashi, T., Wagner, S. J., Iyomoto, N., Edwards, P. G., Hayashida, K., Inoue, S., Madejski, G. M., Takahara, F., Tanihata, C., & Kawai, N. 2001, ApJ, 560, 659

Krabbe, A., Genzel, R., Drapatz, S., & Rotaciuc, V. 1991, ApJL, 382, L19

Larkin, J., Barczys, M., Krabbe, A., Adkins, S., Aliado, T., Amico, P., Brims, G., Campbell, R., Canfield, J., Gasaway, T., Honey, A., Iserlohe, C., Johnson, C., Kress, E., Lafreniere, D., Magnone, K., Magnone, N., McElwain, M., Moon, J., Quirrenbach, A., Skulason, G., Song, I., Spencer, M., Weiss, J., & Wright, S. 2006, New Astronomy Review, 50, 362

Lawrence, A., & Papadakis, I. 1993, ApJL, 414, L85

Lu, J. R., Ghez, A. M., Hornstein, S. D., Morris, M. R., Becklin, E. E., & Matthews, K. 2009, ApJ, 690, 1463

Lyubarskii, Y. E. 1997, MNRAS, 292, 679

Madigan, A., Levin, Y., & Hopman, C. 2009, ApJL, 697, L44

Markowitz, A., Edelson, R., Vaughan, S., Uttley, P., George, I. M., Griffiths, R. E., Kaspi, S., Lawrence, A., McHardy, I., Nandra, K., Pounds, K., Reeves, J., Schurch, N., & Warwick, R. 2003, ApJ, 593, 96

Marrone, D. P., Baganoff, F. K., Morris, M., Moran, J. M., Ghez, A. M., Hornstein, S. D., Dowell, C. D., Munoz, D. J., Bautz, M. W., Ricker, G. R., Brandt, W. N., Garmire, G. P., Lu, J. R., Matthews, K., Zhao, J. ., Rao, R., & Bower, G. C. 2007, ArXiv e-prints, 712

Martins, F., & Plez, B. 2006, AAP, 457, 637

Mauerhan, J. C., Morris, M., Walter, F., & Baganoff, F. K. 2005, ApJL, 623, L25

McGinn, M. T., Sellgren, K., Becklin, E. E., & Hall, D. N. B. 1989, ApJ, 338, 824

McHardy, I. M., Koerding, E., Knigge, C., Uttley, P., & Fender, R. P. 2006, Nature, 444, 730

Melia, F., & Falcke, H. 2001, ARAA, 39, 309

Merritt, D. 2005, in Growing Black Holes: Accretion in a Cosmological Context, ed. A. Merloni, S. Nayakshin, & R. A. Sunyaev, 221–235

Merritt, D. 2010, ApJ, 718, 739

Merritt, D., Mikkola, S., & Szell, A. 2007, ApJ, 671, 53

Merritt, D., & Milosavljević, M. 2005, Living Reviews in Relativity, 8, 8

Meyer, L., Do, T., Ghez, A., Morris, M. R., Witzel, G., Eckart, A., Bélanger, G., & Schödel, R. 2008, ApJL, 688, L17

Meyer, L., Do, T., Ghez, A., Morris, M. R., Yelda, S., Schödel, R., & Eckart, A. 2009, ApJL, 694, L87

Meyer, L., Eckart, A., Schödel, R., Duschl, W. J., Mužić, K., Dovčiak, M., & Karas, V. 2006, AAP, 460, 15

Moneti, A., Stolovy, S., Blommaert, J. A. D. L., Figer, D. F., & Najarro, F. 2001, AAP, 366, 106

Morris, M. 1993, ApJ, 408, 496

Murphy, B. W., Cohn, H. N., & Durisen, R. H. 1991, ApJ, 370, 60

Paltani, S. 1999, in Astronomical Society of the Pacific Conference Series, Vol. 159, BL Lac Phenomenon, ed. L. O. Takalo & A. Sillanpää, 293–+

Papadakis, I. E., & Lawrence, A. 1993, MNRAS, 261, 612

Paumard, T., Genzel, R., Martins, F., Nayakshin, S., Beloborodov, A. M., Levin, Y., Trippe, S., Eisenhauer, F., Ott, T., Gillessen, S., Abuter, R., Cuadra, J., Alexander, T., & Sternberg, A. 2006, ApJ, 643, 1011

Paumard, T., Maillard, J.-P., & Morris, M. 2004, AAP, 426, 81

Press, W. H. 1978, Comments on Astrophysics, 7, 103

Press, W. H., & Rybicki, G. B. 1989, ApJ, 338, 277

Priestley, M. B. 1981, Spectral Analysis and Time Series, Vol. 1 & 2 (Elsevier Academic Press)

Rafelski, M., Ghez, A. M., Hornstein, S. D., Lu, J. R., & Morris, M. 2007, ApJ, 659, 1241

Rayner, J. T., Cushing, M. C., & Vacca, W. D. 2009, ApJS, 185, 289

Reid, M. J., & Brunthaler, A. 2004, ApJ, 616, 872

Rieke, G. H., & Lebofsky, M. J. 1985, ApJ, 288, 618

Schödel, R., Eckart, A., Alexander, T., Merritt, D., Genzel, R., Sternberg, A., Meyer, L., Kul, F., Moultaka, J., Ott, T., & Straubmeier, C. 2007, AAP, 469, 125

Schödel, R., Ott, T., Genzel, R., Eckart, A., Mouawad, N., & Alexander, T. 2003, ApJ, 596, 1015

Schödel, R., Ott, T., Genzel, R., Hofmann, R., Lehnert, M., Eckart, A., Mouawad, N., Alexander, T., Reid, M. J., Lenzen, R., Hartung, M., Lacombe, F., Rouan, D., Gendron, E., Rousset, G., Lagrange, A.-M., Brandner, W., Ageorges, N., Lidman, C., Moorwood, A. F. M., Spyromilio, J., Hubin, N., & Menten, K. M. 2002, Nature, 419, 694

Scoville, N. Z., Stolovy, S. R., Rieke, M., Christopher, M., & Yusef-Zadeh, F. 2003, ApJ, 594, 294

Simonetti, J. H., Cordes, J. M., & Heeschen, D. S. 1985, ApJ, 296, 46

Timmer, J., & Koenig, M. 1995, AAP, 300, 707

Trippe, S., Gillessen, S., Gerhard, O. E., Bartko, H., Fritz, T. K., Maness, H. L., Eisenhauer, F., Martins, F., Ott, T., Dodds-Eden, K., & Genzel, R. 2008, AAP, 492, 419

Trippe, S., Paumard, T., Ott, T., Gillessen, S., Eisenhauer, F., Martins, F., & Genzel, R. 2007, MNRAS, 375, 764

Uttley, P., McHardy, I. M., & Papadakis, I. E. 2002, MNRAS, 332, 231

van Belle, G. T., Lane, B. F., Thompson, R. R., Boden, A. F., Colavita, M. M., Dumont, P. J., Mobley, D. W., Palmer, D., Shao, M., Vasisht, G. X., Wallace, J. K., Creech-Eakman, M. J., Koresko, C. D., Kulkarni, S. R., Pan, X. P., & Gubler, J. 1999, AJ, 117, 521

van Dam, M. A., Bouchez, A. H., Le Mignant, D., Johansson, E. M., Wizinowich, P. L., Campbell, R. D., Chin, J. C. Y., Hartman, S. K., Lafon, R. E., Stomski, Jr., P. J., & Summers, D. M. 2006, PASP, 118, 310

Vaughan, S. 2005, AAP, 431, 391

Vaughan, S., Fabian, A. C., & Nandra, K. 2003, MNRAS, 339, 1237

Wizinowich, P. L., Le Mignant, D., Bouchez, A. H., Campbell, R. D., Chin, J. C. Y., Contos, A. R., van Dam, M. A., Hartman, S. K., Johansson, E. M., Lafon, R. E., Lewis, H., Stomski, P. J., Summers, D. M., Brown, C. G., Danforth, P. M., Max, C. E., & Pennington, D. M. 2006, PASP, 118, 297

Yelda, S., Ghez, A. M., Lu, J. R., Do, T., Clarkson, W., & Matthews, K. 2010, ArXiv e-prints

Young, P. 1980, ApJ, 242, 1232

Yusef-Zadeh, F., Bushouse, H., Dowell, C. D., Wardle, M., Roberts, D., Heinke, C., Bower, G. C., Vila-Vilaró, B., Shapiro, S., Goldwurm, A., & Bélanger, G. 2006, ApJ, 644, 198

Zamaninasab, M., Eckart, A., Witzel, G., Dovciak, M., Karas, V., Schödel, R., Gießübel, R., Bremer, M., García-Marín, M., Kunneriath, D., Mužić, K., Nishiyama, S., Sabha, N., Straubmeier, C., & Zensus, A. 2010, AAP, 510, A3+